Dissertation
submitted to the
Combined Faculties for the Natural Sciences and for Mathematics
of the Ruperto-Carola University of Heildeberg, Germany
for the degree of
Doctor of Natural Sciences

Put forward by

Diplom-Physicist: Sören Kopelke

Born in: Hamburg, Germany

Oral examination: 7th of December, 2011

Quenching of Molecular Photodissociation by Interatomic Coulombic Decay

Der Einfluss des Interatomic Coulombic Decay (ICD) auf die Kerndynamik in den ersten vier Vibrations-Zuständen des $CO^* B^1\Sigma^+$ Rydberg-Zustandes in CO·Mg wird quantitativ untersucht. Eine Methode zur Berechnung der dazu benötigten ICD-Breiten wird eingeführt. Die Methode wird anhand von Berechnungen der ICD-Breiten von Anregungen in der äußeren Valenz in NeAr, $HCNMg_n$, $n = 1, 2$, und in der inneren Valenz in NeMg getestet.

The impact of Interatomic Coulombic decay (ICD) on the photoinduced dynamics in the first four vibrational levels of the $CO^* B^1\Sigma^+$ Rydberg state in CO·Mg clusters is investigated. A method for calculating the required ICD widths is introduced. The method is tested by calculations of ICD widths of outer-valence excited states in NeAr, $HCNMg_n$, $n = 1, 2$, and inner-valence excited states in NeMg.

Contents

CHAPTER 1

Introduction

Electronically excited states in atoms and molecules can decay by photon emission, and, if the excitation energy is higher than the ionization energy of the system, radiationlessly by the emission of electrons. Well-known examples for the latter decay mode are autoionization (AI) [1] and the Auger decay [2] which are governed by *intra*atomic or *intra*molecular electron correlation. If an excited system is placed in an environment and the excitation energy is sufficient to ionize the environment, another process can take place which is driven by *inter*atomic or *inter*molecular electron correlation. This process is known as interatomic Coulombic decay (ICD) [3]. Due to its fundamental and interdisciplinary relevance it has been the topic of extensive experimental [4–12] and theoretical [13–25] research since its discovery.

In the present work ICD emanating from neutral electronic excitations is investigated. Our particular interest lies in the single excitations of inner- and outer-valence electrons which can be produced in single photon absorption. The interatomic decay of such excited states is known as resonant ICD (RICD) [18] or excitation transfer ionization (ETI) [19] in the case of inner- or outer-valence excitations, respectively. A schematic illustration of both processes can be found in Fig. 1.1. The two processes are distinguished because an inner-valence excitation, in contrast to outer-valence excitations, can decay by autoionization as well.

A part of the fundamental relevance of the ICD is due to its impact on processes taking place in excited states in poly-atomic physical, chemical, and biological systems embedded in environments. Nevertheless, up to this point in time this impact has neither been investigated nor understood sufficiently.

Dynamics taking place in excited states of isolated poly-atomic systems have been topic of a multitude of experimental and theoretical works and the reader is referred to textbooks to get an overview [26–28]. Since there are many situations in nature and experiments where systems cannot considered to be isolated, the impact of environments on the dynamics must be investigated as well. A special consequence of the presence of an environment is ICD; it stands out because it is a *purely environmental effect*, i.e., it happens only due to the presence of the environment. Since the ICD is generally a very efficient process, an essential question is, how processes which take place in isolated excited poly-atomic system like photodissociation, isomerization, etc [26–28] are affected by ICD and whether they can be quenched by means of it. In the present work, we investigate the impact of ICD on photodissociation. To this end, we study the photodissociation
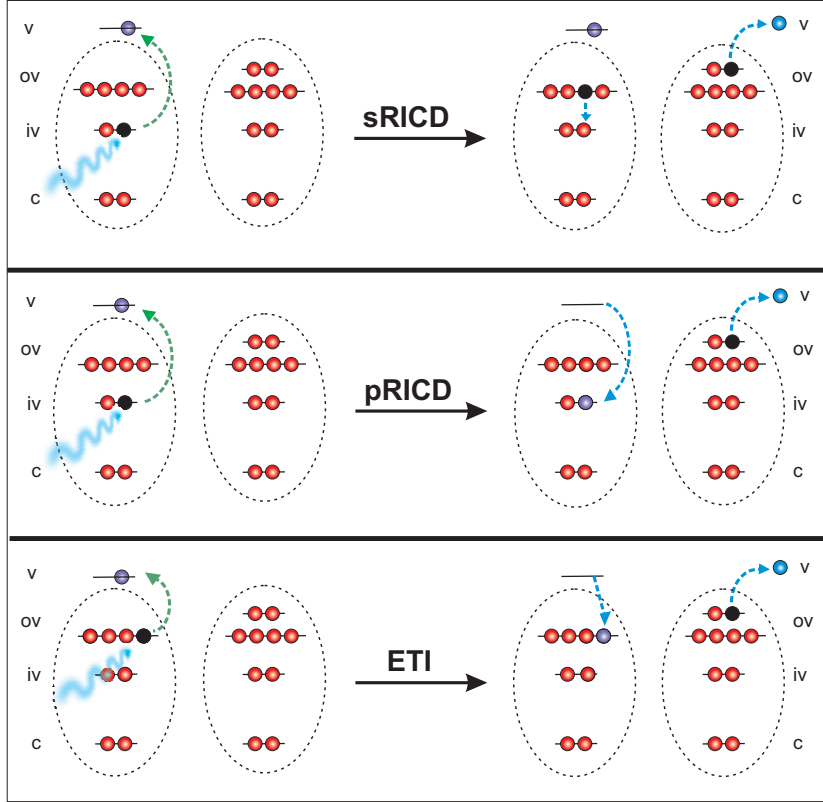
Figure 1.1: Schematic illustration of decay pathways following electronic excitations which are relevant in this work. The labeling indicates the type of orbital: core (c), inner-valence (iv), outer-valence (ov), and virtual (v), respectively. The uppermost frame shows spectator resonant interatomic Coulombic decay (sRICD), the middle box depicts participator resonant interatomic Coulombic decay (pRICD), and the lowermost frame illustrates the scheme of the excitation transfer ionization (ETI) process. See text for more details. Note that if we successively execute the electron to orbitals of higher and higher energies, decay by ETI will eventually cease to exist, but the decay by sRICD will still be highly efficient.

dynamics of CO [29] in the presence of an environment. In particular, we study the predissociation dynamics in the four lowest vibrational levels of the $B^1\Sigma^+$ Rydberg state of CO in CO·Mg. We study this system because, firstly, CO and Mg are weakly bonded which allows to exclude side effects, and, secondly, the corresponding dynamics of isolated CO have been investigated extensively and are well understood [29–32]. In order to carry out dynamics taking into account ICD the corresponding decay rates must be known.

Apart from the energetics, the widths are the most important attribute of ICD. Their knowledge allows one to estimate the efficiency of the decay into a particular channel and to calculate the distributions of the final states [22,33–36]. Decaying states are characterized by complex energies $E = E_R - i\tilde{\Gamma}/2$. The width $\tilde{\Gamma}$ is the sum over partial decay widths of all open decay channels, i.e. radiative,

autoionization, interatomic Coulombic, etc. The radiative widths are usually much smaller than the ICD rates and can be neglected. In the following we will understand by the width Γ the sum of the partial widths due to electron emission only.

There is a need of efficient and accurate methods for calculating Γ. The complexity of the ICD process precludes the derivation of a general analytical formula for the decay width. Only if the distance between the excited system and the environment becomes large it is possible to obtain analytical expressions in the framework of the virtual photon transfer model [16, 21]. The analytical expressions are reasonably accurate at large internuclear distances, but can underestimate the true widths at equilibrium geometries by orders of magnitude [16, 21]. However, since they can be expressed by the properties of the isolated excited system and environment, whose values are often available in the literature, these asymptotic expressions provide an easy way for estimating the interatomic decay widths and can be used to verify *ab initio* results at asymptotic distances.

The property of resonances to have complex energies suggests a natural computational approach to the width Γ: analytic continuation of the many-electron Hamiltonian into the complex energy plane. This can be achieved by adding a complex absorbing potential (CAP) to the Hamiltonian [37–39]. In the case of electronic decay this Hamiltonian is represented using some many-electron ansatz, e.g. algebraic diagrammatic construction (ADC) [40, 41], coupled cluster (CC) [42], or configuration interaction (CI) [43, 44]. The complex resonance energy is obtained by repeated diagonalization of the non-Hermitian complex symmetric Hamiltonian matrix for different CAP parameters. Since addition of a CAP discretizes the electronic continuum, CAP based methods have the advantage of being able to use $\mathcal{L}^2$ basis sets common in standard methods for electronic structure calculations, to represent the continuum part of wave functions of resonances. The major drawbacks of the method are its numerical cost, the fact that a narrow resonance does not manifest itself in the results until the underlying one-particle basis set becomes of considerable size [37].

Another approach to calculate such widths is based on the picture introduced by Fano [45] and Feshbach [46] of a resonance as a bound state embedded and interacting with the continuum. In its framework the decay width is obtained from a golden-rule-like expression [45, 47, 48]. The initial and final states of the decay can be constructed by a variety of techniques. To lowest order in perturbation theory they can be taken as spin-adapted Slater determinants of one-electron functions [49]. The resulting calculations are very efficient numerically, but the neglect of electron correlation usually leads to rather inaccurate results [18, 50]. The ansatz was improved in calculations of the interatomic decay in systems having inversion symmetry by utilizing CI including single excitations to describe the initial states [23]. Further improvement has been achieved employing the so-called Fano ansatz [51] to represent the initial and the final states as well as

the coupling between them accounting for electron correlation consistently. The extension of these methods to the estimation of partial decay widths is possible [52], allowing us to calculate the autoionization and ICD widths separately.

The main disadvantage of the original Fano ansatz is the use of continuum electron wave functions whose asymptotic behavior and correct normalization cannot be reproduced by $\mathcal{L}^2$ basis sets. This difficulty has been overcome in Ref. [51] by combining the Fano ansatz with the Stieltjes imaging technique [53–59]. Employing this technique helps to evaluate decay widths by the Fano method using $\mathcal{L}^2$ one-particle basis sets. The Stieltjes imaging technique allows to extract correctly normalized continuum quantities, e.g. decay widths or photoionization cross sections, from a discrete spectrum by calculating the spectral moments of the quantity in question and using them to construct consecutive approximations to the quantity itself. Stieltjes imaging was previously applied to the calculations of the widths of states decaying by electron emission [16, 51, 60]. The standard implementation of the Stieltjes imaging requires the knowledge of a large part of the eigenspectrum of the corresponding Hamiltonian matrix and is, therefore, restricted to atomic or small molecular systems. This drawback of the Stieltjes imaging technique was realized very early on [61] and a number of suggestions how it can be overcome exist in the literature [61–64]. A general approach of overcoming the bottleneck was proposed [65] for the calculation of photoionization cross sections. The approach is based on applying the Stieltjes imaging procedure to the block-Lanczos pseudospectra instead of the full spectra of the Hamiltonian. In the block Lanczos procedure one converges iteratively to a subspace of eigenvectors having non-zero overlap with a starting block of vectors [66]. A judicious choice of the latter adapted to the problem at hand allows one to obtain continuum quantities to a desired precision within reasonable computational time. The conjunction of Fano ansatz, Stieltjes imaging, and Lanczos method is called Fano-Stieltjes-Lanczos (FSL) method [65].

In the course of the present work, we implement the FSL method for the calculation of widths of neutral excited states decaying by electron emission. In our implementation the ADC method [67, 68] is used to calculate the properties of involved excited states. Phenomenologically and numerically it is more demanding to determine properties of neutral excited states than properties of ionized or doubly ionized states since the configuration space required for an accurate description is much larger and the interpretation of the results is more sophisticated. However, the large dimension of the required configuration spaces make the use of the Lanczos method is especially gainful. In the course of the present work, we test the approach by applying it to calculations of ETI widths in NeAr, HCN·Mg$_n$, $n = 1, 2$, and to the determination of RICD widths in NeAr. Later on it is used to compute the ETI widths in CO·Mg.

This work is structured as follows: chapter 2 introduces the theory forming the FSL approach. In chapter 3 asymptotic formulae for ETI are derived. We apply

the FSL approach to calculations of ETI and RICD widths of systems of interest in chapter 4 and 6, respectively. The dynamics of CO in CO·Mg after CO$^*B^1\Sigma^+$ excitations are investigated in chapter 5. The results of this work are summarized in chapter 7.

Chapter **1**

Throughout this work scalars will be denoted by italic letters, vectors $\mathbf{v}$ are given as bold letters. Letters which are bold and underlined represent matrices $\underline{\mathbf{M}}$, operators are indicated by a hat, and $\| \cdots \|$ denotes the Euclidian norm of the embraced quantity. If not stated otherwise in the respective chapter or section, the indices j, k, l represent occupied and the indices a, b, c unoccupied molecular orbitals. The indices r, s are general. Atomic units are used throughout the present work.

Theory

In this chapter we introduce the theory of our numerical approach for the calculation of ICD widths. The whole approach, which is summarized at the end of this chapter, is called Fano-Stieltjes-Lanczos method (FSL).

2.1 Calculating Properties of Resonances

In quantum mechanics a resonant state or resonance can be regarded as a bound state which is embedded in and coupled to one or more continua. As it is shown below, resonances are characterized by complex energies $E = E_\phi + \Delta - i\Gamma/2$; for reasons which will become clear later E_ϕ is denoted as the formation energy, Δ as the energy shift, and the imaginary part Γ as the width of the resonance. The determination of resonance energies in atomic and molecular systems is a central part of the present work. The formation energy E_ϕ can be calculated comparatively easily using efficient quantum chemical $\mathcal{L}^2$ methods. However, the determination of the shift Δ and the width Γ is difficult as they depend on continuum states whose asymptotic behavior and correct normalization cannot be reproduced by $\mathcal{L}^2$ basis sets.

However, there are methods which can determine those quantities using $\mathcal{L}^2$ basis sets exclusively. In order to understand the underlying idea, solutions of the Schrödinger equation in a restricted function space can be considered. If the space consists of $\mathcal{L}^2$ functions only, the solutions are subject to the artificially imposed boundary condition

$$B: \quad \phi_0(r \to \infty) = 0. \tag{2.1}$$

On the other hand, the physical boundary condition of a resonance reads [69–73]

$$B_0: \quad \phi(r \to \infty) \sim e^{ikr \exp(-i\alpha)}, \quad k, \alpha > 0, \tag{2.2}$$

where $\alpha = \frac{1}{2}\mathrm{Arg}(E)$ is related to the width of the resonance. In order to obtain solutions which fulfil the correct boundary condition in a $\mathcal{L}^2$ function space, the coordinates must be transformed $r \to r'$ so that the Schrödinger equation in the transformed coordinates with the physical boundary condition $B_0(r')$ is the same as the Schrödinger equation in the original coordinates with the artificial boundary condition $B(r)$, i.e.,

$$B_0(r') = B(r). \tag{2.3}$$

It can be shown, that this can be achieved by the transformation [69–73]

$$r \to re^{i\theta}. \tag{2.4}$$

It results in a change of the initially diverging boundary condition, $B_0(r)$, to

$$B_0(re^{i\theta}) : \int_0^\infty e^{ikr\exp(i(\theta-\alpha))} = \text{finite} \quad \text{if } \sin(\theta-\alpha) > 0. \tag{2.5}$$

Introducing the new coordinates into the Schrödinger equation leads to a new equation [74, 75]

$$\hat{H}(\theta) = e^{-2i\theta}\hat{T} + e^{-2i\theta}\hat{V}. \tag{2.6}$$

The expectation value of (2.6) with respect to $\mathcal{L}^2$ functions is complex [69, 74, 75]. This rotation of the Hamiltonian into the complex plane is known as complex scaling [71, 72]. Resonances are revealed upon the transformation since the energy of the continuum states rotates as $E \to E\exp(-2i\theta)$ [70–73]. Due to their special boundary conditions (2.2), resonances are rotated only about α [70–73] and, consequently, are revealed upon the rotation if the pure continuum states are rotated further. Since the resonances wave function is asymptotically convergent (2.5) in the new coordinates, the resonant parameters can be obtained using $\mathcal{L}^2$ functions only.

Another way to continue the Hamiltonian into the complex plane is to employ CAPs [37, 39, 76, 77]

$$\hat{H}(\eta) = \hat{T} + e^{-2i\eta}\hat{V}. \tag{2.7}$$

A CAP is an absorbing boundary condition in the exterior region of the scattering target. All scattering functions and the continuum part of the wave functions of resonances are literally absorbed by the imaginary potential and as a result they become square integrable. In order to reveal resonances the CAP strength η is varied. As in the case of complex scaling, the energies of resonances are affected up to a certain degree by the CAP, continuum states are spatially extended and, therefore, interact strongly with the CAP. Hence, resonances exhibit a minimum with respect to the CAP strength [39]. Since CAPs are just additional potentials which, similarly to the Hamiltonian, can be expanded in basis sets, they are much more convenient to use in conjunction with many-body methods compared to complex scaling.

The major drawback of the use of complex scaling and CAPs are their numerical costs: in order to reveal resonances large very basis sets are required [37, 39]. Moreover, these methods are inappropriate to determine partial widths (for complex scaling see [78]; to our knowledge there is no study for CAPs). However, partial widths are often desirable because they help to understand the decay process in detail and to estimate channel couplings.

In this work we use an approach which is based on the splitting of the domain of the Hamiltonian into a part that represents bound states and another part describing continuum states. Splitting of the domain is known as projection formalism [46]. Within this formalism, the effects of the continuum on the bound states, a shift and a broadening, are naturally given by the coupling through the Hamiltonian. Assuming the coupling as a perturbation which is switched on adiabatically, one can use time-dependent perturbation theory to derive an expression for the shift and the width. This approach is known as Wigner-Weisskopf method [79]; derivations and discussions can, e.g., be found in Ref. [49, 80]. The Wigner-Weisskopf method has the disadvantage that it produces results correct only up to the first non-vanishing order of perturbation theory and it is cumbersome to go beyond this level of approximation. Thus, the method is practically limited to estimate the order of magnitude of the coupling and to elucidate the underlying mechanism. As a consequence, we chose to work with a more general approach.

The approach is based on the observation that the wave functions of resonances can be expressed by a linear combination of a wave function describing a bound state and a wave function representing the background continuum. It was originally independently proposed by Fano to determine the shape of resonances in electron-atom scattering [45] and Feshbach to describe resonant scattering in nuclear physics [46, 81]. Later on, it was used by Malley [82], Bardsley [83], and Mies [84] to describe resonant electron-molecule scattering and further developed by Howat *et al* in order to describe states undergoing Auger decay [47, 48]. In the literature, the approach is often denoted as Fano method and we will stick to this name throughout this work. In order to derive an expression for the shift and the width within the Fano method we consider the Hamiltonian matrix

$$
\begin{aligned}
\langle \phi | H | \phi \rangle &= E_\phi, \\
\langle \psi_{E'} | H | \phi \rangle &= V_{E'}, \\
\langle \psi_{E''} | H | \psi_{E'} \rangle &= E' \delta(E'' - E'),
\end{aligned}
\tag{2.8}
$$

where $|\phi\rangle$ denotes a bound state, $|\psi_{E'}\rangle$ a continuum state and the off-diagonal element $V_{E'}$ describes the coupling between them. In general the eigenvectors of the matrix with elements (2.8) read

$$
|\Psi_E\rangle = a(E)|\phi\rangle + \int dE' b_{E'}(E) |\psi_{E'}\rangle.
\tag{2.9}
$$

To obtain solutions for the coefficients a and $b_{E'}$, the ansatz wave function $|\Psi_E\rangle$ is inserted into the time-independent Schrödinger equation

$$
\hat{H}|\Psi_E\rangle = E|\Psi_E\rangle,
\tag{2.10}
$$

which is then multiplied, respectively, with $|\phi\rangle$ and $|\psi_{E'}\rangle$ from the left, and is integrated over the electronic coordinates. Thus, the following system of equations is obtained

$$aE_\phi + \int dE' V_{E'}^* b_{E'} = Ea, \qquad (2.11a)$$

$$V_E a + E' b_{E'} = E b_{E'} \qquad (2.11b)$$

A solution of the system can be found by expressing $b_{E'}$ in terms of a. However, this solution exhibits a singularity at $E - E'$. To handle it one can use the formal solution introduced by Dirac [85]

$$b_{E'} = \left[P \frac{1}{E - E'} + z(E)\delta(E - E') \right] V_E a, \qquad (2.12)$$

where P indicates that the principal part of the integral should be taken. Inserting (2.12) into (2.11a) and cancelling a (at energies close to the real part of the energy of the resonance $a \neq 0$) we obtain a formal solution for the energy of the resonance:

$$E = E_\phi + \Delta(E) - z(E)|V_E|^2. \qquad (2.13)$$

Consequently, the energy of the resonance is given by the energy of the bound state E_ϕ plus the so-called shift $\Delta(E)$ which is defined as follows

$$\Delta(E) = P \int dE' \frac{V_{E'}^* V_E}{E - E'}, \qquad (2.14)$$

and a part which contains $z(E)$. From (2.13) a formal solution for $z(E)$ is obtained

$$z(E) = \frac{E - E_\phi - \Delta(E)}{|V_E|^2}. \qquad (2.15)$$

It is also possible to obtain a solution for $z(E)$ by imposing boundary conditions [46,83]. The decay of a resonance can be considered as a half-scattering process. Taking an excited state as the point of origin, there can be only outgoing electron waves. From scattering theory it is well known that such a decay process can be specified by choosing the boundary conditions [46,86]

$$z(E) = -i\pi. \qquad (2.16)$$

This choice directly yields the expression of the energy of the resonance given in the first paragraph of this section:

$$E = E_\phi + \Delta - i\Gamma/2, \qquad (2.17)$$

where

$$\Gamma = 2\pi|V_E|^2. \tag{2.18}$$

The last step in the solution of the system of equations (2.11) is the determination of the coefficient a which can be obtained by normalization:

$$\langle \Psi_{\tilde{E}}|\Psi_E\rangle = a^*(\tilde{E})a(E) + \int dE' b^*_{E'}(\tilde{E})b_{E'}(E) = \delta(\tilde{E} - E). \tag{2.19}$$

By inserting the formal solution of $b_{E'}$ (2.12) and the derived expression for $z(E)$ (2.15) into (2.19) the following solution is obtained [45]

$$|a(E)|^2 = \frac{|V_E|^2}{[E - E_\phi - \Delta(E)]^2 + \pi^2|V_E|^4}. \tag{2.20}$$

Obviously, due to the coupling to the continuum the discrete state is diluted and the amplitude or shape of the resonance in the energy spectrum is given by a Lorentz profile with a half width $\Gamma = 2\pi|V_E|^2$ which is connected to the mean lifetime of the resonance by $\tau = 1/\Gamma$. Since we will make further use of the result for the width it is written more generally:

$$\Gamma(E) = 2\pi \sum_\beta |\langle \phi_d|\hat{H} - E|\psi^+_{\beta,E}\rangle|^2, \tag{2.21}$$

where $|\phi_d\rangle$ stands for the decaying N-electron state and $|\psi^+_{\beta,E}\rangle$ for the outgoing energy-normalized N-electron continuum state of energy E, with β enumerating all open channels of the decay. The sum runs over all available final states of energy E, and the relevant width is found by evaluating $\Gamma(E)$ at $E = E_r$ where E_r is the energy of the decaying state corrected for the interaction with continuum. In the calculations presented in this paper we take $E_r \approx E_d$, the formation energy of the decaying state.

Having the solutions

$$a = \sin(\Theta(E))/\pi V_E \tag{2.22}$$

$$b_{E'} = \frac{|V_{E'}|^2 \sin(\Theta(E))}{\pi V_E^*(E - E')} - \cos(\Theta(E))\delta(E - E'), \tag{2.23}$$

where

$$\Theta(E) = -\arctan\frac{\pi|V_E|^2}{E - E_\phi - \Delta}, \tag{2.24}$$

one can consider how the probability to excite the resonances $|\Psi_E\rangle$ is related to experimental observations. To this end, the transition matrix element of a general transition operator $\hat{T}$ is considered

$$
\begin{aligned}
\langle\Psi_E|\hat{T}|i\rangle &= \frac{1}{\pi V_E^*}\langle\phi|\hat{T}|i\rangle\sin\Theta + \frac{1}{\pi V_E^*}\mathrm{P}\int dE'\frac{V_{E'}^*\langle\psi_{E'}|\hat{T}|i\rangle}{E-E'}\sin\Theta \\
&\quad - \langle\psi_E|\hat{T}|i\rangle\cos\Theta \\
&= \frac{1}{\pi V_E^*}\langle\Phi|\hat{T}|i\rangle\sin\Theta - \langle\psi_E|\hat{T}|i\rangle\cos\Theta,
\end{aligned}
\tag{2.25}
$$

where

$$
|\Phi\rangle = |\phi\rangle + \mathrm{P}\int dE'\frac{V_{E'}^*|\psi_{E'}\rangle}{E-E'}.
\tag{2.26}
$$

and $|i\rangle$ denotes an initial state. The strong variation of Θ as E passes through the resonance $E=E_\phi+\Delta$ causes a strong variation of $\langle\Psi_E|\hat{T}|i\rangle$. Since it peaks at $E=E_\phi+\Delta$, experimentally the center of the resonance is observed at this energy. Additionally, $\langle\Phi|\hat{T}|i\rangle$ and $\langle\psi_E|\hat{T}|i\rangle$ contribute to $\langle\Psi_E|\hat{T}|i\rangle$ with opposite phase So, the transition probability $|\langle\Psi_E|\hat{T}|i\rangle|^2$ vanishes at one side of the resonance. The quotient of the transition probability between the initial state and the resonant state $|\langle\Psi_E|\hat{T}|i\rangle|^2$ and the probability of the transition from the initial state to the non-resonant background continuum $|\langle\psi_E|\hat{T}|i\rangle|^2$ determines the measured intensity of the resonance in the spectrum. A discussion for different ratios can be found in [45].

The expression describing the bound-continuum coupling (2.21) obviously contains continuum functions. However, in order to evaluate this kind of matrix elements it is not necessary to know the involved continuum functions explicitly. The properties of wave function constituting these kind of matrix elements allow for an strict $\mathcal{L}^2$ treatment as will be shown in Sec. 2.3. It is important to note that the Fano method is applicable as long as the required separation of the Hamiltonian in a bound and a continuum part is possible.

2.2 Calculating Excited States of Atoms and Molecules

In order to obtain the eigenfunctions and eigenenergies for the electronic motion in molecules one has to solve the many-particle Schrödinger equation

$$\hat{H}\Phi(\mathbf{r}_1, s_1; \ldots; \mathbf{r}_N, s_N) = E\Phi(\mathbf{r}_1, s_1; \ldots; \mathbf{r}_N, s_N) \tag{2.27}$$

where (in atomic units):

$$\hat{H} = \left(-\sum_{i=1}^{N} \frac{1}{2}\nabla_i^2 - \sum_{A=1}^{M}\sum_{i=1}^{N} \frac{Z_A}{|\mathbf{R}_A - \mathbf{r}_i|} + \sum_{j=1}^{N}\sum_{i<j}^{N} \frac{1}{|\mathbf{r}_j - \mathbf{r}_i|} \right) \tag{2.28}$$

Here $\mathbf{r}_i$ and s_i, respectively, denote the spatial and the spin coordinates of the ith electron, and $\mathbf{R}_A$ are the coordinates of the nucleus A. The wave function $\Phi(\mathbf{r}_1, s_1; \ldots; \mathbf{r}_N, s_N)$ is is anti-symmetric with respect to the interchange of the coordinates of two electrons. It can be expanded in a basis of anti-symmetrized products of one-particle functions

$$\Phi_{P_1,\ldots,P_N} = |\psi_{P_1}(\mathbf{r}_1, s_1) \ldots \psi_{P_N}(\mathbf{r}_N, s_N)|$$
$$= \frac{1}{\sqrt{N!}} \begin{vmatrix} \psi_{P_1}(\mathbf{r}_1, s_1) & \ldots & \psi_{P_N}(\mathbf{r}_1, s_1) \\ \vdots & \ddots & \vdots \\ \psi_{P_1}(\mathbf{r}_N, s_N) & \ldots & \psi_{P_N}(\mathbf{r}_N, s_N) \end{vmatrix} \tag{2.29}$$

which are known as Slater determinants [87]. An optimal set of one-particle functions for this expansion can be obtained by a Hatree-Fock (HF) computation ofr the ground state. The HF equations are obtained from the variation principle which minimizes the energy

$$E_0 = \frac{\langle\Phi_0|\hat{H}|\Phi_0\rangle}{\langle\Phi_0|\Phi_0\rangle} \tag{2.30}$$

with respect to the one-particle wave functions $\psi_r(\mathbf{r}, s)$ [87] under the constraint that the latter remain orthonormal $\langle\psi_i|\psi_j\rangle = \delta_{ij}$. The resulting equations which determine the optimal one-particle functions

$$\hat{f}\psi(\mathbf{r}, s) = \left[\hat{h} + \sum_r \hat{J}_r - \sum_r \hat{K}_r\right]\psi(\mathbf{r}, s) = \epsilon_a\psi(\mathbf{r}, s) \tag{2.31}$$

are known as Hartree-Fock (HF) equations. The exchange operator

$$\hat{K}_b\psi(\mathbf{r}, s) = \left[\int d\mathbf{r}'\psi_r^*(\mathbf{r}', s')\frac{1}{|\mathbf{r} - \mathbf{r}'|}\psi(\mathbf{r}', s')\right]|\psi_r(\mathbf{r}, s)\rangle, \tag{2.32}$$

and the Coulomb operator

$$\hat{J}_r\psi_i(\mathbf{r}, s) = \left[\int d\mathbf{r}'\psi_r^*(\mathbf{r}', s')\frac{1}{|\mathbf{r} - \mathbf{r}'|}\psi_r(\mathbf{r}', s')\right]\psi(\mathbf{r}, s). \tag{2.33}$$

represent electron-electron interactions in (2.31); without these terms it would be a one-particle Schrödinger equation

$$\hat{h}\psi_i(\mathbf{r}, s) = \left[-\frac{1}{2}\nabla^2 - \sum_{A=1}^{M}\frac{Z_A}{|\mathbf{R}_A - \mathbf{r}|}\right]\psi_i(\mathbf{r}, s) = \epsilon_i\psi_i(\mathbf{r}, s). \tag{2.34}$$

The Slater determinant of the N energetically lowest optimized one-particle functions is the best possible one-particle approximation to the ground state of the system [87].

Throughout this work we only consider closed-shell systems where all spin orbitals are doubly occupied in the ground state,

$$|\Phi_0\rangle = |\phi_1(\mathbf{r}_1)\chi_\alpha(s_1)\phi_1(\mathbf{r}_2)\chi_\beta(s_2)\ldots$$
$$\ldots\phi_{N/2}(\mathbf{r}_{N-1})\chi_\alpha(s_{N-1})\phi_{N/2}(\mathbf{r}_N)\chi_\beta(s_N)|, \tag{2.35}$$

where the spin orbitals $\psi_i(\mathbf{r}, s) = \phi_i(\mathbf{r})\chi_\gamma(s)$ are represented by products of a spatial function $\phi_i(\mathbf{r})$ and a spin function $\chi_\gamma(s)$. Carrying out the energy minimization (2.31) for closed shell determinants and integrating out the spin yields the closed-shell HF equations for the spatial one-particle functions,

$$\hat{f}\phi(\mathbf{r}) = \left[\hat{h} + \sum_r^{N/2}\left[2\hat{J}_r - \hat{K}_r\right]\right]\phi(\mathbf{r}) = \epsilon\phi(\mathbf{r}). \tag{2.36}$$

The missing factor 2 in front of the exchange term $\hat{K}_r$ reflects the fact that there is only exchange among electrons of parallel spin. By representing the spatial orbitals $|\phi\rangle$ in a basis set, the integro-differential equations (2.36) are transformed into a set of algebraic equations - the so-called Roothaan equations [87]. The system of equations is then solved iteratively until self-consistency is achieved. In order to represent $\hat{J}_r$ and $\hat{K}_r$ during the first iteration, a set of starting orbitals is generated from less elaborate approximations. As a result of the averaging of electron-electron interactions, the HF approximation does not account for the entire electronic energy. The residual part of the interactions is called electron correlation.

Naturally, the questions arises how one can represent excited states within the HF approximation. According to Koopman's Theorem [87] one can interpret the one-particle energies of the occupied and unoccupied HF orbitals as approximations to ionization energies and electron affinities, respectively. Thus, all kind of excited

states can be represented by Slater determinants which differ from the HF ground state $|\Phi_0\rangle$ by their orbital configuration. In the framework of second quantization, excited states can be obtained by applying creation (annihilation) operators $\hat{c}_a^\dagger$ ($\hat{c}_k$) associated with the one-particle functions on the HF gound state. A neutral excited one-hole one-particle (1h1p) state is given by

$$|\Phi_k^a\rangle = \hat{c}_a^\dagger \hat{c}_k |\Psi_0\rangle. \tag{2.37}$$

Analogously, one can define higher excited states like, e.g., two-hole two-particle (2h2p) excited states and so on. The description of such excited state by a single excited HF determinant is usually very crude and not sufficient to predict or verify experimental results. In the calculation of excited states, the enormous importance of the HF approximations lies in the fact that it serves as starting point for more accurate approximations which include electron correlation. To achieve better approximations one has to generate linear combinations of several excited HF determinants and solve the resulting equations for the coefficients. To this end, one often expands the Hamilton operator in a basis of excited HF determinants. This standard wavefunction method is the known as configuration interaction (CI) [87]. The desired properties of the excited state follow from diagonalizing the CI matrix. Since those matrices are usually very large, the diagonalization is usually a very demanding task. The CI method is methodically straightforward but it is not size-consistent unless the complete configuration space is taken into account [88].

Size-consistent wavefunction methods do exist, e.g., coupled-cluster methods [89–94] and complete active space approaches [95, 96]. Alternatively, there are non-wavefunction (Green's function) methods which are based on the polarization propagator [97]. The Random Phase Approximation (RPA) [97], the second order polarization propagator approach (SOPPA) [98, 99], and the algebraic diagrammatic construction (ADC) [67] have been used to compute electronic excitation spectra for a long time. Wavefunction methods and propagator methods can be linked by the so-called intermediate state representation (ISR) [100]. In this work the intermediate state representation approach to the ADC is used to determine the characteristics of excited states. The corresponding theory is presented in the following subsection.

Algebraic Diagrammatic Construction

The ADC method was originally derived employing diagrammatic perturbation theory for the polarization propagator [67, 68]. Later, the ADC scheme was also applied to the one-particle Green's function [101] to obtain properties of ionized states and the pp-propagator [102] to determine properties of doubly ionized states.

In order to derive the ADC we consider the polarization propagator [97] whose spectral representation reads

$$\Pi_{rs,r's'}(\omega) = \sum_{m \neq 0} \frac{\langle \Psi_0 | \hat{c}_r^\dagger \hat{c}_s | \Psi_m \rangle \langle \Psi_m | \hat{c}_{r'}^\dagger \hat{c}_{s'} | \Psi_0 \rangle}{\omega + E_0 - E_m + i\eta}$$

$$+ \sum_{m \neq 0} \frac{\langle \Psi_0 | \hat{c}_{r'}^\dagger \hat{c}_{s'} | \Psi_m \rangle \langle \Psi_m | \hat{c}_r^\dagger \hat{c}_s | \Psi_0 \rangle}{-\omega + E_0 - E_m + i\eta}. \tag{2.38}$$

Here E_0 and E_m denote the energies of the N-electron ground $|\Psi_0\rangle$ and the excited states $|\Psi_m\rangle$, respectively. The first and the second term of (2.38) contain identical physical information. We will consider the first term here, in the following denoted as $\Pi^+(\omega)$, which provides the excitation energies

$$\Omega_m = E_m - E_0 \tag{2.39}$$

and the spectroscopic amplitudes

$$x_{m,rs} \equiv \langle \Psi_m | \hat{c}_r^\dagger \hat{c}_s | \Psi_0 \rangle. \tag{2.40}$$

The ADC form of the propagator is given by

$$\Pi^+(\omega) = \mathbf{f}^\dagger (\omega \underline{\mathbf{1}} - \underline{\mathbf{M}})^{-1} \mathbf{f}. \tag{2.41}$$

$\mathbf{f}$ is the array of effective transition amplitudes $f_{I,rs}$ and $\underline{\mathbf{M}}$ is a hermitian matrix M_{IJ} where the captial latin indices denote electron configurations. For $\underline{\mathbf{M}}$ and $\mathbf{f}$ there are perturbation expansions

$$\underline{\mathbf{M}} = \underline{\mathbf{M}}^{(0)} + \underline{\mathbf{M}}^{(1)} + \dots \tag{2.42a}$$

$$\mathbf{f} = \mathbf{f}^{(0)} + \mathbf{f}^{(1)} + \dots \tag{2.42b}$$

The matrix inverse can be expanded by means of a geometric series

$$(\omega \underline{\mathbf{1}} - \underline{\mathbf{M}})^{-1} = (\omega \underline{\mathbf{1}} - \underline{\mathbf{M}}^{(0)})^{-1} \sum_n \left(\frac{\underline{\mathbf{M}} - \underline{\mathbf{M}}^{(0)}}{\omega \underline{\mathbf{1}} - \underline{\mathbf{M}}^{(0)}} \right)^n. \tag{2.43}$$

Comparing this expansion to the original diagrammatic perturbation expansion of the polarization propagator [97] through order n of perturbation theory yields successively higher-order contributions for the expansion (2.42). The physical information is obtained by solving the eigenvalue problem

$$\underline{\mathbf{M}}\,\underline{\mathbf{X}} = \underline{\mathbf{X}}\,\underline{\mathbf{\Omega}}, \quad \underline{\mathbf{X}}^\dagger \underline{\mathbf{X}} = \underline{\mathbf{1}} \tag{2.44}$$

where $\underline{\mathbf{\Omega}}$ is the diagonal matrix of excitations energies Ω_m. The spectroscopic amplitudes are then given by

$$x_{rs}^{(m)} = \sum_I X_{Im}^* f_{I,rs}. \tag{2.45}$$

As an example, we derive the expressions for $\mathbf{f}$ and $\underline{\mathbf{M}}$ up to first order. The zeroth and the first order of the diagrammatic expansion series of the polarization propagator are depicted in Fig. 2.1. The zeroth order diagram is the leftmost. The corresponding analytical expression reads

$$(\Pi^+_{ak,a'k'})^{(0)}(\omega) = \sum_{a,k} \frac{\delta_{aa'}\delta_{kk'}}{\omega + \epsilon_k - \epsilon_a} \tag{2.46}$$

where a and k denote particle and hole states, respectively. The right hand side of (2.46) can be written in the ADC form
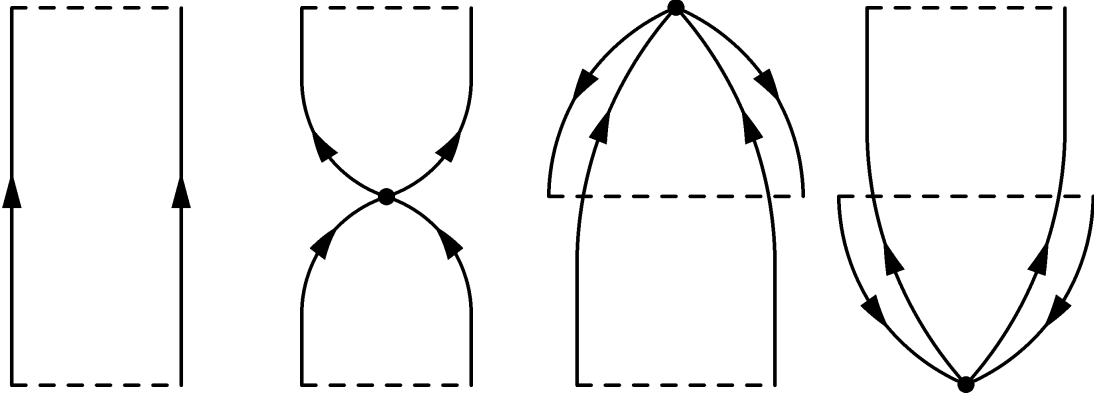
$$(\mathbf{f}^{(0)})^\dagger[\omega\underline{\mathbf{1}} - \underline{\mathbf{M}}^{(0)}]^{-1}\mathbf{f}^{(0)} \tag{2.47}$$

where

$$M^{(0)}_{ak,a'k'} = \delta_{aa'}\delta_{kk'}(\epsilon_a - \epsilon_k) \tag{2.48}$$

$$f^{(0)}_{ak,rs} = \delta_{ar}\delta_{ks} \tag{2.49}$$

The algebraic expressions for the first order can be read from the three first order

Figure 2.1: Goldstone diagrams of the zeroth and first order of the diagrammatic expansion series of the polarization propagator. Both the zeroth order diagram and the three first order diagrams are given in Abrikosov form.

Goldstone diagrams (see Fig. 2.1):

$$X_1 = \frac{1}{\omega + \epsilon_k - \epsilon_a}(-V_{ak'[a'k]})\frac{1}{\omega + \epsilon_{k'} - \epsilon_{a'}}, \tag{2.50}$$

$$X_2 = X_3^* = \frac{V^*_{as[rk]}\bar{n}_s n_r}{\epsilon_a + \epsilon_s - \epsilon_k - \epsilon_r}\frac{1}{\omega + \epsilon_k - \epsilon_a}.$$

To obtain the first order ADC expression, we consider

$$(\Pi^+)^{(1)}(\omega) = (\mathbf{f}^{(1)})^\dagger[\omega\underline{\mathbf{1}} - \underline{\mathbf{M}}^{(0)} - \underline{\mathbf{M}}^{(1)}]^{-1}\mathbf{f}^{(1)}. \tag{2.51}$$

Expanding (2.51) up to first first order yields

$$(\Pi^+)^{(1)}(\omega) = (\mathbf{f}^{(0)})^\dagger (\omega \underline{\mathbf{1}} - \underline{\mathbf{M}}^{(0)})^{-1} \mathbf{f}^{(0)} + (\mathbf{f}^{(1)})^\dagger (\omega \underline{\mathbf{1}} - \underline{\mathbf{M}}^{(0)})^{-1} \mathbf{f}^{(0)}$$
$$+ (\mathbf{f}^{(0)})^\dagger (\omega \underline{\mathbf{1}} - \underline{\mathbf{M}}^{(0)})^{-1} \underline{\mathbf{M}}^{(1)} (\omega \underline{\mathbf{1}} - \underline{\mathbf{M}}^{(0)})^{-1} \mathbf{f}^{(0)}$$
$$+ (\mathbf{f}^{(0)})^\dagger (\omega \underline{\mathbf{1}} - \underline{\mathbf{M}}^{(0)})^{-1} \mathbf{f}^{(1)}. \tag{2.52}$$

Comparing (2.50) to (2.52) yields the corresponding ADC expressions

$$M^{(1)}_{ak,a'k'} = -V_{ak[a'k']}, \tag{2.53}$$

$$f^{(1)}_{ak,rs} = \sum_{r,s} \frac{-V_{as[rk]}\bar{n}_s n_r}{\epsilon_a + \epsilon_s - \epsilon_k - \epsilon_r}. \tag{2.54}$$

The higher order expressions are derived analogously [67].

The derivation of the ADC matrix from the diagrammatic expansion of the polarization propagator does not elucidate in which basis the Hamiltonian has to be represented in order to obtain this matrix. Thus, it is impossible to express other quantities in terms of the ADC approximation and it is inconvenient to use the ADC for modified problems, e.g., if one wants to use CAPs to calculate properties of resonances. The missing connection between the wave function and the propagator picture was established roughly ten years after the formulation of the ADC by the so-called intermediate state representation (ISR) [100]. Additionally, the ISR allows for an interpretation of the physical excitations described by the ADC matrix. It is shown that the ADC basis stems from physical excitation operators acting on the correlated ground state [100]. The spectral representation of the polarization propagator is obtained by inserting a complete set of exact N-particle excited states [97]. Similarly, the ADC form of the polarization propagator the can be determined by inserting a complete set of intermediate states $|\tilde{\Psi}^N_J\rangle$. Then the effective interaction $\underline{\mathbf{C}}$ may be expressed as the representation of $(E^N_0 - \hat{H})$ in the intermediate basis

$$(M)_{J,J'} = \langle \tilde{\Psi}^N_J | \hat{H} - E^N_0 | \tilde{\Psi}^N_{J'} \rangle \tag{2.55}$$

and the effective amplitudes read

$$f_{J,rs} = \langle \tilde{\Psi}^N_J | c^\dagger_r c_s | \Psi_0 \rangle. \tag{2.56}$$

This representation of the Hamiltonian is referred to as the intermediate state representation (ISR) [100]. The exact and the intermediate states are connected by an unitary transformation

$$|\tilde{\Psi}^N_m\rangle = \sum_J Q_{mJ} |\tilde{\Psi}^N_J\rangle \tag{2.57}$$

where $\underline{\mathbf{Q}}$ can be identified as the Hermitian conjugate of the ADC eigenvector matrix $\underline{\mathbf{X}}$ from (2.44). Now, one has to determine how to choose $\underline{\mathbf{Q}}$ and thus $|\tilde{\Psi}_J^N\rangle$ that the basic ADC properties are obtained.

In Ref. [100] it is shown that the desired ISR can be obtained from a specific orthonormalization of

$$|\Psi_J^0\rangle = \hat{C}_J|\Psi_0\rangle \tag{2.58}$$

where $\hat{C}_J$ denotes the physical excitation operator

$$\hat{C}_J = \{\hat{c}_a^\dagger \hat{c}_k; \hat{c}_a^\dagger \hat{c}_b^\dagger \hat{c}_k \hat{c}_l, a < b, k < l; \dots\} \tag{2.59}$$

and $|\Psi_0\rangle$ is the correlated ground states with the perturbation series

$$|\Psi_0\rangle = |\Phi_0^{HF}\rangle + |\Psi_0^{(1)}\rangle + |\Psi_0^{(2)}\rangle + \dots \tag{2.60}$$

The orthonormalization is carried out in two steps. First, states of different excitation classes $[J]$ are Gram-Schmidt orthogonalized to get the ISR precursor states $|\Psi_J^\sharp\rangle$. The first excitation class in the case of excited state ADC is orthogonalized to the exact ground state according to

$$|\Psi_{ak}^\sharp\rangle = \hat{c}_a^\dagger \hat{c}_k|\Psi_0\rangle - |\Psi_0\rangle\langle\Psi_0|\hat{c}_a^\dagger \hat{c}_k|\Psi_0\rangle \tag{2.61}$$

Next, symmetric orthonormalization [87] is performed within each excitation class. Taking again 1h1p states as an example, one obtains

$$|\tilde{\Psi}_{ak}\rangle = \sum_{bl} |\Psi_{bl}^\sharp\rangle (S^{-1/2})_{bl,ak}, \tag{2.62}$$

where $\underline{\mathbf{S}}$ is the overlap matrix of the precursor states.

One can find the correlated ground state $|\Psi_0\rangle$ correct up to n-th order of perturbation theory by truncating its perturbation expansion

$$|\Psi_0\rangle = |\Phi_0^{HF}\rangle + |\Psi_0^{(1)}\rangle + |\Psi_0^{(2)}\rangle + \dots \tag{2.63}$$

$|\Phi_0^{HF}\rangle$ being the Hartree-Fock ground state. Correspondingly, one can construct a hierarchy of approximations, ADC(n), $n = 1, 2, \dots$ in which the expansion of the Hamiltonian in the intermediate states of successive excitation classes $[J]$ is truncated in accordance with the correlated ground state (Eq. (2.63)). Performing the orthonormalization procedure of Eq. (2.61) and (2.62) approximately and consistently with the order of the many-body perturbation theory used for the construction of the correlated ground state (see Eq. (2.63)), the Hamiltonian matrix elements of the type $\langle\tilde{\Psi}_J|H|\tilde{\Psi}_{J'}\rangle$ can be expressed analytically using one-particle energies and the two-electron integrals [103, 104].

The required one-particle orbitals are obtained by a restricted Hartree-Fock calculation. In the post Hartree-Fock calculations we employ the strict ADC(2) [or ADC(2)s] and the extended ADC(2) [or ADC(2)x] schemes. These schemes use second order perturbation theory for the correlated ground state and expand the excited states in the 1h1p and 2h2p excitation classes. Both ADC(2) schemes treat the 1h1p-1h1p and 1h1p-2h2p couplings in second and first order, respectively. The ADC(2)s scheme neglects the coupling between different 2h2p intermediate states, while the extended ADC(2)x scheme takes into account the 2h2p-2h2p interactions to first order. One obtains singly excited states correct to second order in both schemes, while doubly excited states are correct to zeroth or first order in the ADC(2)s and ADC(2)x schemes, respectively.

The ADC possesses two important properties: compactness and separability (also known as size-consistency). Separability means that results obtained for a system AB consisting of the non-interacting components A and B are identical to the sum of the results obtained by separate calculations for system A and system B. Compactness means that the configuration space used to represent the ADC matrix does not increase in every order with the order of approximation of the main states of the corresponding propagator. E.g., in the case of ADC for the polarization propagator the main states are the 1h1p excitations. The configuration space of ADC(2) and ADC(3) comprises 1h1p and 2h2p configurations. ADC(4) and ADC(5) matrices must be spanned by 1h1p, 2h2p and 3h3p configurations.

2.3 The Stieltjes Imaging Technique

The idea how a $\mathcal{L}^2$ pseudo-spectrum can be used to get a correctly normalized approximation to the width $\Gamma(E)$ can be sketched as follows [56]: consider the cumulative function $\Pi(E)$ defined according to the equations:

$$\Pi(E) = \int dE' \Gamma(E'), \tag{2.64a}$$

$$\Gamma(E) = \frac{d\Pi}{dE}. \tag{2.64b}$$

Using the $\mathcal{L}^2$ pseudo-spectrum $\{\chi_{\beta,\tilde{E}_n}, \tilde{E}_n\}$, $n = 1, \ldots, N$ in the expression (2.21) to represent the continuum, a set of couplings

$$\tilde{\gamma}_n = 2\pi |\langle \phi_d | \hat{H} - E | \chi_{\beta,\tilde{E}_n} \rangle|^2 \tag{2.65}$$

is obtained at the corresponding energies $\tilde{E}_n$. By adding up all couplings $\tilde{\gamma}_n$ a histogram approximation to the auxiliary cumulative function $\tilde{\Pi}(E)$ is defined

$$\tilde{\Pi}(E) \approx \sum_{n=1}^{N} \tilde{\gamma}_n, \tag{2.66}$$

where the order is determined by the corresponding energies $\tilde{E}_n < E < \tilde{E}_{n+1}$. The derivative of $\tilde{\Pi}(E)$

$$\tilde{\Pi}'(E) = \sum_{n=1}^{N} \tilde{\gamma}_n \delta(E - \tilde{E}_n) \tag{2.67}$$

returns the discrete pseudospectrum. By connecting the neighboring midpoints

$$\left(\frac{\tilde{E}_{n-1} + \tilde{E}_n}{2}, \frac{\tilde{\gamma}_{n-1} + \tilde{\gamma}_n}{2} \right) \tag{2.68a}$$

and

$$\left(\frac{\tilde{E}_n + \tilde{E}_{n+1}}{2}, \frac{\tilde{\gamma}_n + \tilde{\gamma}_{n+1}}{2} \right) \tag{2.68b}$$

with straight lines, the cumulative function $\Pi(E)$ is obtained from $\tilde{\Pi}(E)$. In contrast to $\tilde{\Pi}'(E)$, the derivative $\Pi'(E)$ is free of any delta-function-like singularities. The numerical (Stieltjes) derivative at the midpoints $\bar{E}_n = \frac{1}{2}(\tilde{E}_n + \tilde{E}_{n+1})$ is given explicitly by

$$\Pi'(\bar{E}_n) = \frac{\tilde{\gamma}_n + \tilde{\gamma}_{n+1}}{2(\tilde{E}_{n+1} - \tilde{E}_n)}. \tag{2.69}$$

In an $\mathcal{L}^2$ basis set, the function $\Pi'(E)$ converges to $\Gamma(E)$, as the number of pairs of values of the pseudo-spectrum N increases [53]. Moreover, the expression (2.69) has the correct physical dimensionality ([Energy]), and it shows that the normalization constants of $|\chi_{\beta,\tilde{E}_n}\rangle$, necessary to introduce the correct dimensionality in (2.21), are determined by the density of eigenvalues in the pseudo-spectrum

$$\propto (\tilde{E}_{n+1} - \tilde{E}_n)^{-1}. \tag{2.70}$$

In practice, one does not work directly with the pseudo-spectrum $\{\tilde{E}_n, \tilde{\gamma}_n\}$ since, firstly, the distribution and the density of the pseudo-spectrum depends strongly on the basis set employed. Secondly, there is no criterion whereby one can judge how well the approximated width $\Pi'(E)$ has converged to the true width $\Gamma(E)$.

Both difficulties can be overcome by employing moment theory [105]. The moment theory is commonly known as a tool for reproducing distributions from random variables, which is, for example, important in analyzes of quantum physical experiments [106]. In this work, the goal of the application of moment theory is to determine the pseudo-spectra $\{\gamma_n, E_n\}$ which are evenly distributed, robust with respect to the basis, and give rise to the same moments as the raw pseudo-spectra $\{\tilde{\gamma}_n, \tilde{E}_n\}$. In order to obtain the smoothed pseudo-spectra $\{\gamma_n, E_n\}$ one has to solve the reduced moment problem [105, 107] for the width $\Gamma(E)$:

Given a finite set of moments $S(k)$, $k = 0, \ldots, 2N - 1$, determine a function $\Gamma(E)$ so that it reproduces all available moments in the interval $[a, b]$

$$S(k) = \int_a^b E^k \Gamma(E) dE, \quad k = 0, \ldots, 2N - 1.$$

The application of moment theory to decay width calculations relies on the fact that the negative moments $S(-k)$ of the width $\Gamma(E)$

$$S(-k) = \int_{E_T}^{\infty} E^{-k} \Gamma(E) dE, \tag{2.71}$$

where E_T is the energy of the threshold of interest, can be well approximated by the corresponding sum over the discrete pseudo-spectrum $\{\tilde{E}_n, \tilde{\gamma}_n\}$ obtained from *ab initio* $\mathcal{L}^2$ calculations:

$$S(-k) \approx \sum_{n=1}^{N} \tilde{E}_n^{-k} \tilde{\gamma}_n, \quad k = 0, \ldots, (2N - 1). \tag{2.72}$$

As the raw pseudo-spectrum consists of N pairs of energies and coupling strengths $\{\tilde{E}_n, \tilde{\gamma}_n\}$ only $2N$ moments can be calculated [53]. A finite set of moments does not determine the distribution function $\Gamma(E)$ from (2.71) completely - or, otherwise stated, there are infinitely many weight functions which reproduce the

first few moments. A unique solution $\Gamma(E)$ can be chosen from the infinite number of solutions using the Chebychev algorithm [105]. The Chebychev inequalities [53, 105, 107]

$$\Pi^{(m)}(E_i - 0) \leq \Pi^{(m+1)}(E_i - 0) \leq \Pi(E_i) \leq \Pi^{(m+1)}(E_i + 0) \leq \Pi^{(m)}(E_i + 0) \tag{2.73}$$

where E_i are certain abscissae, which will be discussed below, and $E_i \pm 0$ denote, respectively, upper and lower limits, allow to verify the convergence of the approximations to the cumulative function $\Pi(E)$. $\Pi^{(m)}(E)$ are the cumulative functions calculated by means of the pseudo-spectra $\{\gamma_n, E_n\}^{(m)}$ where the first $2m$ moments were used to determine them. The Chebychev inequalities allow for two important implications [105]:

- At the points E_i the approximated cumulative function $\Pi^{(m)}(E)$ converges to the (true) infinite order function $\Pi(E)$.

- The lower and the upper limit of the approximated cumulative function $\Pi^{(m)}(E)$ bracket the 'infinite order' function $\Pi(E)$ at the E_i.

Consequently, the Chebychev algorithm allows to find the best converging approximation $\Pi^{(m)}$ to the cumulative function $\Pi(E)$ with respect to a given basis set.

In order to solve the reduced moment problem the continued fraction [108]

$$S(z) = \cfrac{\beta_0}{(1/z) - \alpha_1 - \cfrac{\beta_1}{(1/z) - \alpha_2 - \cfrac{\beta_2}{(1/z) - \alpha_3 - \cfrac{\beta_3}{\ddots}}}}, \quad z \in \mathbb{C} \backslash \mathbb{R}_- \tag{2.74}$$

is considered. It converges to the Stieltjes integral [105]

$$S(z) = \int_{E_1}^{\infty} \frac{E\Gamma(E)dE}{E - z}. \tag{2.75}$$

If $\Gamma(E)$ was known one could apply Gaussian quadrature in order to evaluate the Stieltjes integral. The resulting quadrature abscissae and weights (the poles and the residues of the Stieltjes integral) would correspond to the desired spectrum $\{E_n, \gamma_n\}$. Since $\Gamma(E)$ is generally unknown, the spectrum must be obtained via the accessible moments: making use of the definition of the moments (2.71) and the closed-form expression of a geometric series [106] one can expand the Stieltjes

integral in a series of moments

$$
\begin{aligned}
\int_{E_1}^{\infty} \frac{E\Gamma(E)dE}{E-z} &= \int_{E_1}^{\infty} \frac{\Gamma(E)dE}{1-z/E} \\
&= \sum_k \int_{E_1}^{\infty} E^{-k}\Gamma(E)dE z^k \\
&= \sum_k S(-k)z^k = S(0) + S(-1)z + S(-2)z^2 + \dots
\end{aligned}
\tag{2.76}
$$

Now, the continued fraction (2.74) can be truncated and approximated using Padé approximations [109] to it, which retains the analytical structure of $S(z)$. From the first $2N$ moments the following Padé approximations can be obtained

$$
[n, n-1](z) = \frac{P_{n-1}(z)}{Q_n(z)},
\tag{2.77}
$$

where

$$
P_{n-1}(z) = \sum_{i=0}^{n-1} a_i^n z^i,
\tag{2.78a}
$$

$$
Q_n(z) = 1 + \sum_{i=1}^{n-1} b_i^n z^i,
\tag{2.78b}
$$

up to the maximal order $[N, N-1](z)$. Consequently, via the continued fraction and the Stieltjes integral the polynomials $P_{n-1}(z)$ and $Q_n(z)$ of the nth order Padé approximation are connected to the series of moments

$$
[n, n-1](z) = S(0) + S(-1)z + S(-2)z^2 + \dots
\tag{2.79}
$$

The coefficients of the continued fraction α_n and β_n and the coefficients of the polynomials a_i^n and b_i^n associated with the polynomials $P_{n-1}(z)$ and $Q_n(z)$, can be determined from the moments $S(-k)$ using the three-term recurrence relations

$$
\begin{aligned}
Q_n(z) &= (1 - \alpha_n z)Q_{n-1}(z) - z^2 \beta_{n-1} Q_{n-2}(z), \\
Q_0(z) &= 1, \quad Q_{-1}(z) = 0, \\
P_{n-1}(z) &= (1 - \alpha_n z)P_{n-2}(z) - z^2 \beta_{n-1} P_{n-3}(z), \\
P_0(z) &= \beta_0, \quad P_{-1}(z) = 0,
\end{aligned}
$$

$$
\tag{2.80a}
$$
$$
\tag{2.80b}
$$

which produce polynomials orthogonal to the weight function $\Gamma(E)$

$$
\int_{E_1}^{\infty} Q_n(E)Q_m(E)\Gamma(E)dE = \delta_{n,m}.
\tag{2.81}
$$

Equations which express the coefficients in terms of moments can directly be derived from (2.79)

$$\alpha_n = \frac{Y_{n-1,n}}{Y_{n-1,n-1}} - \frac{Y_{n-2,n-1}}{Y_{n-2,n-2}}, \quad \alpha_0 = 0, \quad \alpha_1 = \frac{S(-1)}{S(0)}, \tag{2.82a}$$

$$\beta_n = \frac{Y_{n,n}}{Y_{n-1,n-1}}, \quad \beta_{-1} = 0, \quad \beta_0 = S(0), \tag{2.82b}$$

where the matrix elements are given by

$$Y_{n,l} = \int_{E_1}^{\infty} E^{-l-n} Q_n(E)\Gamma(E)dE, \tag{2.83}$$

and, according to (2.80), satisfy the recurrence relations [54]

$$Y_{n,l} = Y_{n-1,l+1} - \alpha_n Y_{n-1,l} - \beta_{n-1} Y_{n-2,l}, \tag{2.84a}$$

$$Y_{n,l} = 0, \quad n < l, \tag{2.84b}$$

$$Y_{n,l} = S(-l), \tag{2.84c}$$

$$Y_{n,-1} = Y_{-1,l} = 0. \tag{2.84d}$$

By approximating the moments $S(-k)$ in (2.84) by the discrete pseudo-spectrum, the coefficients from (2.82) can be obtained directly from them [107]

$$\tilde{\alpha}_n = \frac{1}{\tilde{\beta}_0\tilde{\beta}_1\ldots\tilde{\beta}_{n-1}} \sum_{i=1}^{N} \left(\frac{1}{\tilde{E}_i}\right)^{2n-1} [Q_{n-1}(\tilde{E}_i)]^2 \tilde{\gamma}_i, \tag{2.85}$$

$$\tilde{\beta}_n = \frac{1}{\tilde{\beta}_0\tilde{\beta}_1\ldots\tilde{\beta}_{n-1}} \sum_{i=1}^{N} \left(\frac{1}{\tilde{E}_i}\right)^{2n} [Q_n(\tilde{E}_i)]^2 \tilde{\gamma}_i. \tag{2.86}$$

The values $Q_{n-1}(\tilde{E}_i)$ and $Q_n(\tilde{E}_i)$ are obtained from (2.80a). The particular abscissae E_i and weights γ_i of the new spectrum of order m required in (2.73) are given by the roots and the residues of $[N, N-1](z)$ [54, 107]

$$Q_n(E_i^{(m)}) = 0, \qquad\qquad i = 1,\ldots,m, \tag{2.87a}$$

$$\gamma_i^{(m)} = \frac{P_{n-1}(E_i^{(m)})}{E_i^{(m)} Q'(E_i^{(m)})}. \tag{2.87b}$$

Now, each of these N spectra $\{\gamma_n, E_n\}$ is used to generate an approximation to the corresponding cumulative function $\Pi^{(m)}$. Note, that the first five sets are usually too rough and are, thus, not appropriate to verify the convergence. Thus one needs a least a decent amount of energy-coupling pairs in order to get a meaningful approximation [107]. The sets of order $m > 20$ are often oscillating and should be used cautiously.

Three important properties of the presented method are remarked. First, the positive spectral moments of the photoionization matrix element of the hydrogen atom diverge (see [55] and references therein). Therefore, negative moments are used in the Stieltjes imaging calculations. Second, the Stieltjes method is a smoothing method. In its framework, only a finite number of moments can be calculated. Consequently, sharp features of the quantity which is approximated cannot be resolved. Third, as has already been mentioned in Sec. 1, the knowledge of $|\chi_{\beta,\tilde{E}_n}\rangle$ is necessary for the spectral moment calculation, which means that final state Hamiltonian matrix must be diagonalized. Already for systems composed of a few atoms this is a computational bottleneck, and makes the calculations in the case of large systems impossible. A number of schemes were proposed which are helpful to circumvent this difficulty: Nesbet proposed a solution completely bypassing the diagonalization of the Hamiltonian matrix [61] and applied the approach to the boron atom. Ågren, Carravetta and co-workers used the iterative solution of the response-type equations to calculate effective spectral moments from a reduced space [63,64]. This method has been applied to several diatomic systems. In Ref. [65] another way to circumvent the full diagonalization has been proposed where Stieltjes imaging were applied to Lanczos pseudo-spectra in order to the determine molecular photoionization cross sections. It has been shown in that work that the knowledge of a relatively low-order Lanczos pseudospectrum is sufficient to obtain the converged spectral moments. In the course of this work, we show that the Stieltjes procedure in conjunction with the Lanczos method can be used to calculate the decay widths in atomic and molecular systems within the Fano formalism [51].

2.4 The Lanczos Method

A subspace $\bar{\delta}_m = \mathrm{span}(\mathbf{z}_1, \ldots, \mathbf{z}_m)$, $m < n$ spanned by the eigenvectors $\mathbf{z}_i$ of the symmetric matrix $\underline{\mathbf{A}} \in \mathbb{R}^{n \times n}$, is invariant under the transformation $\underline{\mathbf{A}}$ [66, 110]. If

$$\underline{\mathbf{B}}_m \equiv [\mathbf{q}_1, \ldots, \mathbf{q}_m] \tag{2.88}$$

is an orthonormal basis of the arbitrary subspace δ_m, the residual matrix

$$\underline{\mathbf{R}}(\underline{\mathbf{B}}_m) = \underline{\mathbf{A}}\,\underline{\mathbf{B}}_m - \underline{\mathbf{B}}_m \underline{\mathbf{H}}_m \quad \text{with} \quad \underline{\mathbf{H}}_m \equiv \underline{\mathbf{B}}_m^\dagger \underline{\mathbf{A}}\,\underline{\mathbf{B}}_m. \tag{2.89}$$

shows how much of the basis is invariant under the transformation $\underline{\mathbf{A}}$. The diagonalization of the Rayleigh-Quotient matrix $\underline{\mathbf{H}}_m$ leads to the eigenpairs $\{\theta_i, \mathbf{g}_i\}$ of eigenvalues θ_i and eigenvectors $\mathbf{g}_i$. Multiplying the eigenvectors $\mathbf{g}_i$ by $\underline{\mathbf{B}}_m$ the so-called Ritz eigenpairs $\{\theta_i, \mathbf{y}_i = \underline{\mathbf{B}}_m \mathbf{g}_i\}$ are obtained. They are the best approximation to eigenpairs of $\underline{\mathbf{A}}$, which can be derived from δ_m. This procedure of finding approximations to the eigenpairs of $\underline{\mathbf{A}}$ is known as the Rayleigh-Ritz method (RRM) [66]. For an arbitrary subspace δ_m this method is very expensive because it requires the orthogonalization of δ_m and the diagonalization of $\underline{\mathbf{H}}_m$. However, the computational effort can be reduced enormously by applying the RRM on sequences of Krylov subspaces

$$\mathcal{K}_m(\mathbf{f}, \underline{\mathbf{A}}) \equiv \mathrm{span}\{\mathbf{f}, \underline{\mathbf{A}}\mathbf{f}, \ldots, \underline{\mathbf{A}}^{m-1}\mathbf{f}\}. \tag{2.90}$$

where $\mathbf{f}$ is a starting vector. This approach is known as the Lanczos method [111].

The Lanczos method is very efficient because if the Krylov matrix

$$\underline{\mathbf{K}}_m(\mathbf{f}, \underline{\mathbf{A}}) \equiv [\mathbf{f}, \underline{\mathbf{A}}\mathbf{f}, \ldots, \underline{\mathbf{A}}^{m-1}\mathbf{f}] \tag{2.91}$$

has a full rank it can be QR factorized [66, 110, 112]

$$\underline{\mathbf{K}}_m(\mathbf{f}, \underline{\mathbf{A}}) = \underline{\mathbf{B}}_m \underline{\mathbf{C}}_m^{-1}, \tag{2.92}$$

where $\underline{\mathbf{B}}_m$ is defined according to (2.88) and $\underline{\mathbf{C}}_m^{-1}$ is an upper triangular matrix. Now, each Krylov subspace $\mathcal{K}_m(\mathbf{f}, \underline{\mathbf{A}})$ exhibits the characteristic property that for each $j < m$ $\underline{\mathbf{A}}\mathcal{K}_j \subset \mathcal{K}_{j+1}$. In particular, $\mathbf{q}_i \perp \mathcal{K}_{i-1}$ and $\underline{\mathbf{A}}\mathbf{q}_j \in \mathcal{K}_{j+1}$. Consequently,

$$\mathbf{q}_i^\dagger \underline{\mathbf{A}}\mathbf{q}_j = 0 \ \ \forall \ \ i > j + 1. \tag{2.93}$$

Id est, the new $\mathbf{q}_j$ have to be orthonormalized only to two preceding basis vectors or, alternatively, $\underline{\mathbf{B}}_m^\dagger \underline{\mathbf{A}}\,\underline{\mathbf{B}}_m$ is tridiagonal and there is a three-term recurrence

relation for generating $\underline{\mathbf{B}}_m$ from $\underline{\mathbf{A}}$. By defining $\alpha_j = \mathbf{q}_j^\dagger \underline{\mathbf{A}} \mathbf{q}_j$ and $\beta_j = \mathbf{q}_{j+1}^\dagger \underline{\mathbf{A}} \mathbf{q}_j$, the tridiagonal matrix $\underline{\mathbf{T}}_m = \underline{\mathbf{B}}_m^\dagger \underline{\mathbf{A}} \underline{\mathbf{B}}_m$ reads

$$
\underline{\mathbf{T}}_m = \begin{bmatrix} \alpha_1 & \beta_1 & & \cdots & 0 \\ \beta_1 & \alpha_2 & \ddots & & \vdots \\ & \ddots & \ddots & \ddots & \\ \vdots & & \ddots & \ddots & \beta_{m-1} \\ 0 & \cdots & & \beta_{m-1} & \alpha_m \end{bmatrix}. \tag{2.94}
$$

The columns of $\underline{\mathbf{A}}\,\underline{\mathbf{B}}_m = \underline{\mathbf{B}}_m \underline{\mathbf{T}}_m$ are given by

$$
\underline{\mathbf{A}} \mathbf{q}_j = \beta_{j-1}\mathbf{q}_{j-1} + \alpha_j \mathbf{q}_j + \beta_j \mathbf{q}_{j+1}, \tag{2.95}
$$

where $j = 1, \ldots, m-1$ and $\beta_0 \alpha_0 \equiv 0$. Since $\mathbf{q}_{j+1}$ are the quantities of interest, (2.95) is modified using the definition $\mathbf{r}_j = (\underline{\mathbf{A}} - \alpha_j \underline{\mathbf{1}})\mathbf{q}_j - \beta_{j-1}\mathbf{q}_{j-1}$

$$
\mathbf{q}_{j+1} = \frac{\mathbf{r}_j}{\beta_j} = \frac{\mathbf{r}_j}{\pm \| \mathbf{r}_j \|}, \tag{2.96}
$$

because $\mathbf{q}_j$ are supposed to be orthonormal, one can choose $\| \mathbf{r}_j \|$ to be positive without losing generality. If $\mathbf{r}_j = \mathbf{0}$ the iteration breaks down. Thus, the Lanczos procedure can be sketched formally by

$$
\mathbf{r}_0 = \mathbf{q}_1; \;\; \beta_0 = 1; \;\; \mathbf{q}_0 = \mathbf{0}; \;\; j = 0, \tag{2.97}
$$
$$
\textbf{while}(\beta_j \neq 0)
$$
$$
\mathbf{q}_{j+1} = \mathbf{r}_j / \beta_j; \;\; j = j+1; \;\; \alpha_j = \mathbf{q}_j^\dagger \underline{\mathbf{A}} \mathbf{q}_j
$$
$$
\mathbf{r}_j = (\underline{\mathbf{A}} - \alpha_j \underline{\mathbf{1}})\mathbf{q}_j - \beta_{j-1}\mathbf{q}_{j-1}; \;\; \beta_j = \| \mathbf{r}_j \|_2
$$
$$
\textbf{end}.
$$

The quantities $\mathbf{q}_j$ are called Lanczos vectors. If the iteration (2.97) stops (since $\beta_j \approx 0$) before the tridiagonalization is complete then the starting vector $\mathbf{q}_1$ is contained in a proper invariant subspace of $\underline{\mathbf{A}}$. In such a case, the Lanczos procedure runs until $j = m$ where $m = \text{rank}(\underline{\mathbf{K}}_n(\mathbf{q}_1, \underline{\mathbf{A}}))$.

In practical applications the event $\beta_j \to 0$ is very unlikely. Nevertheless, it is possible to verify the convergence of the eigenvalues by looking at the Ritz eigenpairs. Therefore, let us assume that $\underline{\mathbf{T}}_j$ after j Lanczos iterations is known and that it has been diagonalized

$$
\underline{\mathbf{G}}_j^\dagger \underline{\mathbf{T}}_j \underline{\mathbf{G}}_j = \text{diag}(\theta_1, \ldots, \theta_j). \tag{2.98}
$$

The matrix of Ritz vectors $\underline{\mathbf{Y}}_j$ is obtained by

$$
\underline{\mathbf{Y}}_j = [\mathbf{y}_1, \ldots, \mathbf{y}_j] \equiv \underline{\mathbf{B}}_j \underline{\mathbf{G}}_j \in \mathbb{R}^{j \times j}, \tag{2.99}
$$

and the Ritz vectors obey the relation [66]

$$\| \, \underline{\mathbf{A}}\mathbf{y}_i - \theta_i\mathbf{y}_i \, \| = |\beta_j||g_{ji}|, \quad i = 1, \ldots, j, \tag{2.100}$$

with $g_{ji} \equiv \| \, \mathbf{e}_j^\dagger \underline{\mathbf{G}}\mathbf{e}_i \, \|$, where $\mathbf{e}_i$ is the ith coordinate vector. Then the expression for the computable error bound to the eigenvalues of $\underline{\mathbf{T}}_j$ reads

$$\min_{\mu \in \lambda(\underline{\mathbf{A}})} |\theta_i - \mu| \leq |\beta_j||g_{ji}| \equiv \beta_{ij}. \tag{2.101}$$

If β_{ij} becomes small a good convergence is achieved.

Beside its efficiency the Lanczos method has two important properties. Firstly, it converges to the extremal eigenvalues of $\underline{\mathbf{A}}$ most efficiently and, secondly, it correctly reproduces the global structure of the spectrum. In order to understand the first property, one can use another way to derive the three-term recurrence (2.96) [112]: the maximum and minimum values of the Rayleigh quotients

$$r(\mathbf{x}) = \frac{\mathbf{x}^\dagger \underline{\mathbf{A}}\mathbf{x}}{\mathbf{x}^\dagger \mathbf{x}} \tag{2.102}$$

of the matrix $\underline{\mathbf{A}} \in \mathbb{R}^{n \times n}$ are equal to the largest $\lambda_1(\underline{\mathbf{A}})$ and the smallest $\lambda_n(\underline{\mathbf{A}})$ eigenvalue of this matrix [112]. If there is a sequence $\{\mathbf{q}_i\}$ of orthonormal vectors $\mathbf{q}_i \subseteq \mathbb{R}^j$ with $j < n$ one can define the scalars M_j and m_j by

$$M_j = \lambda_1(\underline{\mathbf{B}}_j^\dagger \underline{\mathbf{A}}\, \underline{\mathbf{B}}_j) = \max_{\mathbf{z} \neq 0} \frac{\mathbf{z}^\dagger(\underline{\mathbf{B}}_j^\dagger \underline{\mathbf{A}}\, \underline{\mathbf{B}}_j)\mathbf{z}}{\mathbf{z}^\dagger \mathbf{z}} = \max_{\|\mathbf{z}\|=1} r(\underline{\mathbf{B}}_j\mathbf{z}) \leq \lambda_1(\underline{\mathbf{A}}), \tag{2.103a}$$

$$m_j = \lambda_n(\underline{\mathbf{B}}_j^\dagger \underline{\mathbf{A}}\, \underline{\mathbf{B}}_j) = \min_{\mathbf{z} \neq 0} \frac{\mathbf{z}^\dagger(\underline{\mathbf{B}}_j^\dagger \underline{\mathbf{A}}\, \underline{\mathbf{B}}_j)\mathbf{z}}{\mathbf{z}^\dagger \mathbf{z}} = \min_{\|\mathbf{z}\|=1} r(\underline{\mathbf{B}}_j\mathbf{z}) \geq \lambda_n(\underline{\mathbf{A}}), \tag{2.103b}$$

where $\mathbf{z}$ is an appropriate vector and $\underline{\mathbf{B}}_j \equiv [\mathbf{q}_1, \ldots, \mathbf{q}_j]$. The connection to the problem of determining orthonormal bases for Krylov spaces can be established by considering how to generate $\mathbf{q}_j$ so that M_j and m_j are progressively better approximations to the eigenvalues $\lambda_1(\underline{\mathbf{A}})$ and $\lambda_n(\underline{\mathbf{A}})$. Suppose there is a $\mathbf{u}_j \in$ span$\{\mathbf{q}_1, \ldots, \mathbf{q}_j\}$ such that $M_j = r(\mathbf{u}_j)$. Since $r(\mathbf{x})$ increases most rapidly in the direction of its gradient we can ensure that $M_{j+1} > M_j$ if $\mathbf{q}_{j+1}$ is calculated so that

$$\nabla r(\mathbf{u}_j) \in \text{span}\{\mathbf{q}_1, \ldots, \mathbf{q}_{j+1}\}. \tag{2.104}$$

Analogously, if there is a $\mathbf{v}_j \in$ span$\{\mathbf{q}_1, \ldots, \mathbf{q}_j\}$ for which $r(\mathbf{v}_j) = m_j$ then one can claim

$$\nabla r(\mathbf{v}_j) \in \text{span}\{\mathbf{q}_1, \ldots, \mathbf{q}_{j+1}\}. \tag{2.105}$$

because $r(\mathbf{x})$ falls off most rapidly in the direction $-\nabla r(\mathbf{x})$. Consider a Krylov space

$$\mathrm{span}\{\mathbf{q}_1,\ldots,\mathbf{q}_j\} = \mathrm{span}\{\mathbf{q}_1,\underline{\mathbf{A}}\mathbf{q}_1,\ldots,\underline{\mathbf{A}}^{j-1}\mathbf{q}_1\}. \tag{2.106}$$

Since $\nabla r(\mathbf{x}) \in \mathrm{span}\{\mathbf{x},\underline{\mathbf{A}}\mathbf{x}\}$ [112], $\mathbf{q}_{j+1}$ can be chosen so that

$$\mathrm{span}\{\mathbf{q}_1,\ldots,\mathbf{q}_{j+1}\} = \mathrm{span}\{\mathbf{q}_1,\underline{\mathbf{A}}\mathbf{q}_1,\ldots,\underline{\mathbf{A}}^{j}\mathbf{q}_1\}. \tag{2.107}$$

Thus, we returned to the problem of generating orthonormal bases for Krylov spaces.

The Kaniel-Paige theory [66, 112] provides *a priori* relations to describe the convergence quantitatively. The relations provide error bounds to the eigenvalues [66] and, moreover, show the role of the starting vector in the convergence process. Assume $\theta_1 \geq \cdots \geq \theta_j$ are the eigenvalues of $\underline{\mathbf{T}}_j$ and $\mathbf{q}_1,\ldots,\mathbf{q}_j$ the corresponding Lanczos vectors after j Lanczos iterations. The bounds for θ_j are then given by

$$\lambda_n \leq \theta_j \leq \lambda_n + \frac{(\lambda_1 - \lambda_n)\tan^2(\phi_m)}{C_{j-1}(1+2\rho_n)^2}, \tag{2.108}$$

where $\cos\phi_n \equiv |\mathbf{q}_n^\dagger \mathbf{z}_n|$, $\rho_n \equiv (\lambda_{n-1}-\lambda_n)/(\lambda_1-\lambda_{n-1})$, and $C_j(x)$ is the Chebychev polynomial of degree j [112]. Furthermore, $\lambda_1 \geq \cdots \geq \lambda_n$ are the true eigenvalues of $\underline{\mathbf{A}}^{n\times n}$ and $\mathbf{z}_1,\ldots,\mathbf{z}_n$ the corresponding eigenvectors. C_j are bounded on $[-1,1]$, but grow with x^j outside. So, the convergence increases with the number of iterations. From (2.108) we can read that the convergence is better for isolated eigenvalues and that eigenvectors which are orthogonal to the Lanczos vectors cannot be recovered. Thus, the starting vector should be chosen such that the resulting Krylov space has a large overlap with the eigenvectors of interest. In practice, the Lanczos method is not as efficient as it is theoretically. Due to round off errors the orthogonality among the $\mathbf{q}_i$ gets lost and, as a consequence, the algorithm generates redundant copies of Ritz pairs (the so-called ghost eigenvalues, see [66], Chap. 13.3 for details). This issue can be overcome by reorthogonalization of $\mathbf{q}_i$ during the process of convergence which increases the costs of the method [66, 112].

The second important property of the Lanczos method, that it recovers the global structure of the spectrum correctly even if individual eigenpairs are far from having converged, can be understood as follows. After j Lanczos iterations one can approximate a matrix $\underline{\mathbf{H}}$ by [113]

$$\underline{\mathbf{H}}^{(j)} = \underline{\mathbf{B}}_j \underline{\mathbf{T}}_j \underline{\mathbf{B}}_j^\dagger. \tag{2.109}$$

The exact and the approximated matrix are connected by

$$\mathbf{q}_1^\dagger \underline{\mathbf{H}}^k \mathbf{q}_1 = \mathbf{q}_1^\dagger \left(\underline{\mathbf{H}}^{(j)}\right)^k \mathbf{q}_1, \quad 0 \leq k \leq 2j-1, \ j = \mathrm{odd},$$
$$0 \leq k \leq 2j-2, \ j = \mathrm{even}. \tag{2.110}$$

Id est, the first $2j - 2$ or $2j - 1$ moments of $\underline{\mathbf{H}}^{(j)}$ are exact with respect to the starting vector $\mathbf{q}_1$. In the sense

$$\left(\underline{\mathbf{H}}^{(j)}\right)^k \mathbf{q}_1 = \underline{\mathbf{H}}^k \mathbf{q}_1, \quad 0 \le k \le j - 1, \tag{2.111}$$

the matrix $\underline{\mathbf{H}}^{(j)}$ is the best approximation to $\underline{\mathbf{H}}$. This property is very helpful when moments of resolvents or other functions of the Hamiltonian are to be calculated [113]. Moreover, it means that the Lanczos method can be used for calculations of spectral moments [53–55,114]. The nth moment M_n of the width (2.21) can be approximated by

$$\begin{aligned} M_n &= \langle \Psi_d | (\hat{H} - E)^\dagger \hat{H}^n (\hat{H} - E) | \Psi_d \rangle \\ &\approx \langle \Psi_d | (\hat{H} - E)^\dagger (\hat{H}^{(N)})^n (\hat{H} - E) | \Psi_d \rangle \\ &= \sum_{i=0}^{N} (E_i^{(N)})^n |\langle \Psi_d | (\hat{H} - E) | \chi_i^{(N)} \rangle|^2, \end{aligned} \tag{2.112}$$

where $E_i^{(N)}$ and $\chi_i^{(N)}$ are the Nth order Lanczos eigenenergies and eigenvectors, respectively, which stem from the Nth order approximation to $\hat{H}$

$$\hat{H}^{(N)} = \sum_{i,j=0}^{N} |\psi_i\rangle\langle\psi_i|\hat{H}|\psi_j\rangle\langle\psi_j| \,. \tag{2.113}$$

$\langle\psi_i|\hat{H}|\psi_j\rangle$ is tridiagonal. As N increases, the Lanczos pseudospectrum becomes a successively better approximation to the true spectrum of $\hat{H}$.

For our purposes the block Lanczos method [66,112,114], which is a straightforward generalization of the Lanczos method, is more appropriate. In the block Lanczos method the initial state is replaced by a set of initial states $|\phi_0^m\rangle$ which form a starting block. The block version is theoretically analog; it is, however, numerically more stable than the simple Lanczos method [112] and, as we will see in Sec. (4) and Sec. (6), it provides the possibility to start from blocks consisting of many states what is more suitable for our purposes.

2.5 Fano-Stieltjes-Lanczos method

In the course of this work the Fano-Stieltjes-Lanczos method for the calculation of widths of excited states has been realized. The program relies purely on *ab initio* methods. Its course can be summarized by the following scheme:

- Perform a HF calculation. It provides the MOs, their energies, and the corresponding two-electron integrals in MO basis.

- Select an ADC scheme (ADC(1), ADC(2)s, and ADC(2)x are available).

- Define the configuration subspace of the decaying states (Q) and of the final states of the decay (P)

- Calculate the decaying state of interest ϕ_d and its energy E_d by carrying out an ADC calculation using the configuration subspace Q.

- Compute the final states ψ_n and their energies E_n by performing an ADC calculation using subspace P; the spectrum is obtained by means of the Lanczos method.

- For each final state ψ_n calculate the coupling $\gamma_n = 2\pi|\langle\phi_d|\hat{H}_e|\psi_n\rangle|^2$.

- Apply the Stieltjes imaging procedure to the couplings γ_n at the corresponding energies E_n to obtain the width.

The HF calculations does not solely provide the MOs, their energies, and two-electron integrals. The MOs and their energies together with the knowledge of the leading configurations of the decaying states and the final states of the decay are necessary to define appropriate configuration subspaces Q and P. As mentioned in Sec. 2.1, in principle any post HF method could be chosen. However, our FSL program provides ADC(1), ADC(2)s, and ADC(2)x only. While the ADC(1) procedure solely works in the space of 1h1p configurations, the ADC(2)s and ADC(2)x methods include 2h2p configurations. As a consequence, the method must be chosen before the configuration spaces are defined. For both the Q and the P subspace, the FSL program provides the opportunity to select up to 50 occupied MOs, for 1h1p and 2h2p configurations separately, which are by default combined with all available unoccupied MOs.

Asymptotic Formulae of Interatomic Decay Rates

3.1 General Theory

The complexity of the interatomic decay process involving electron correlation precludes a description of the decay width by an analytical formula. If the internuclear distance between the system and the neighbor is large, it is, however, possible to obtain analytical formulae using the virtual photon transfer model [16]. These formulae provide accurate decay widths at large interatomic distances, but they underestimate the true widths at the equilibrium distance by orders of magnitude [16]. Nevertheless, the formulae are useful because they solely rely on properties of the isolated excited system and the isolated neighbor which are often available in the literature or, if unknown, are easier to measure or calculate, respectively. The formulae are helpful in the seek of interesting systems and can be used to verify *ab initio* results at asymptotic distances. In this section, we derive asymptotic formulae for the interatomic energy transfer after a neutral excitation on atom A of a cluster $A \cdots B$. The results for dipole-dipole transitions were published in Ref. [21].

At large internuclear distances bound orbitals in clusters are localized on either A or B. In order to derive the formulae, matrix elements between continuum and bound orbitals localized on one cluster subunit are considered. Bound and continuum orbitals $|\gamma, l, m, \mu, \rangle$ differ by their normalization conditions

$$\langle \gamma', l', m', \mu', |\gamma, l, m, \mu \rangle = \delta_{\gamma\gamma'}\delta_{ll'}\delta_{mm'}\delta_{\mu\mu'}, \tag{3.1a}$$

$$\langle \gamma', l', m', \mu', |\gamma, l, m, \mu \rangle = \delta(\epsilon_\gamma - \epsilon_{\gamma'})\delta_{ll'}\delta_{mm'}\delta_{\mu\mu'}, \tag{3.1b}$$

where ϵ_γ is the energy of the corresponding continuum state, γ denotes the state, l is the angular momentum, m its projection, and μ denotes the spin projection. We suppose that the single determinant ground state of $A \cdots B$ $|\Phi_0\rangle$ is closed-shell. Additionally, we assume that the ground states of the subunits A, $|\Phi_0^A\rangle$, and B, $|\Phi_0^B\rangle$, are closed-shell. At large internuclear distances the ground state of the system is given by the product $|\Phi_0^A\rangle|\Phi_0^B\rangle$.

In the present case, the process originates from a 1h1p many-electron state on subunit A. 1h1p states can be expressed by Slater determinants of the type

$$|ik_u, iv_u\rangle = \hat{c}_{ik_u}^\dagger \hat{c}_{iv_u}|\Phi_0\rangle, \tag{3.2}$$

where $\hat{c}$ are the physical excitation operators of second quantization [97], the subscript u denotes the subunit where the orbitals are localized on, and the

indices $ik_u = (\gamma', l', m', \mu')$ and $iv_u = (\gamma, l, m, \mu)$ contain all relevant quantum numbers. The determinant (3.2) is not an eigenstate of the total spin operator. In general, spin eigenstates are obtained by linear combinations of determinants

$$|ik_u, iv_u; S_u, M_u^s\rangle = \sum_{\mu_{ik}, \mu_{iv}} C_{\mu_{ik}, \mu_{iv}}^{S, M^s} |ik_u, iv_u\rangle, \qquad (3.3)$$

where $C_{\mu_{ik}, \mu_{iv}}^{S, M^s}$ are the Clebsch-Gordan coefficients (CGCs) of the spin angular momentum [115, 116]. Here, the initial state is a spin singlet

$$|ik_u, iv_u; S_u = 0, M_u^s = 0\rangle = \frac{1}{\sqrt{2}}(c_{ik_u, 1/2}^\dagger c_{iv_u, 1/2} + c_{ik_u, -1/2}^\dagger c_{iv_u, -1/2})|\Phi_0\rangle,$$
$$(3.4)$$

$\pm 1/2$ denotes the spin projection and the indices $ik_u = \gamma', l', m' \quad iv_u = \gamma, l, m$ no longer contain the spin projection. However, the spin adapted state (3.4) is not an eigenfunction of the total angular momentum operator. In order to obtain symmetry adapted states, the spin adapted states are linearly combined

$$|ik_u, iv_u; l, l'; L_u, M_u\rangle = \sum_{m, m'} |ik_u, iv_u; 0, 0\rangle (l, l'; m, m'|l, l'; L_u, M_u). \qquad (3.5)$$

$(l, l'; m, m'|l, l'; L_u, M_u)$ denote the CGCs of the orbital angular momentum [115, 116] which depend on the total orbital angular momentum of the 1h1p state L_u and its projection on the cluster axis M_u. Since we assume that the system and its constituents are closed shell and that the excitation is generated by a dipole (quadrupole) transition, the initial excitation on subunit A is of ^1P (^1D) symmetry. The eigenstates exhibiting these symmetries are obtained by evaluating (3.5) under the constraints

$$l = 1(2), \ m = 0, \pm 1, (\pm 2); \ l' = 0, \ m' = 0 \quad \vee \ (l \leftrightarrow l'), (m \leftrightarrow m'), \quad (3.6a)$$
$$|ik_u, iv_u; l, l'; 1(2), M_u\rangle = \sum_{m, m'} |ik_u, iv_u; 0, 0\rangle (l, l'; m, m'|l, l'; 1(2), M_u),$$
$$(3.6b)$$

where $(x \leftrightarrow x')$ means that the assignation from the left should be taken with interchanged indices x and x'. The CGCs can be evaluated conveniently using their connection to the $3j$-symbols [116]

$$(l, l'; m, m'|l, l'; L, M) = (-1)^{-l+l'-m}\sqrt{2L+1} \begin{pmatrix} l & l' & L \\ m & m' & -M \end{pmatrix}. \qquad (3.7)$$

The final states of the processes considered here are 1h1p states too and, thus, can be described analogously.

ICD and its related processes are governed by electron correlation [18]. Consequently, the corresponding couplings between the initial and the final states of the process are given by the electron-electron interaction operator

$$\hat{V} = \frac{1}{2}\sum_{i \neq j}\frac{1}{|\mathbf{r}_i - \mathbf{r}_j|}, \tag{3.8}$$

where $\mathbf{r}_i$ denotes the coordinates of the ith electron. From Sec. 2.1 we know that the decay width is given by

$$\Gamma = 2\pi|W_{L_B,L_A}^{M_B,M_A}|^2\delta(E_B - E_A). \tag{3.9}$$

In (3.9) E_B and E_A, respectively, denote the energy of the corresponding state on subunit B and A, the delta function $\delta(\dots)$ ensures energy conservation, and

$$\begin{aligned} W_{L_B,L_A}^{M_B,M_A} &\equiv \langle k_B, ov_B; l_k, l_{ov}; L_B, M_B|\hat{V}|ik_A, iv_A; l_{ik}, l_{iv}; L_A, M_A\rangle \\ &= \sum_{\substack{m_k, m_{ov} \\ m_{ik}, m_{iv}}}(l_k, l_{ov}; m_k, m_{ov}|l_k, l_{ov}; L_B, M_B)^*(l_{ik}, l_{iv}; m_{ik}, m'_{iv}|l_{ik}, l'_{iv}; L_A, M_A) \\ &\quad \times \langle k_B, ov_B; S_B, M_B^s|\hat{V}|ik_A, iv_A; S_A, M_A^s\rangle. \end{aligned} \tag{3.10}$$

The matrix element in (3.10) can be evaluated using Condon-Slater rules or the rules of second quantization [87]. In order to obtain spin reduced matrix elements, the spin variables are integrated out. In the case of singlet 1h1p states $(S_A = S_B = M_A^s = M_B^s = 0)$, the spin reduced expression of the matrix element reads
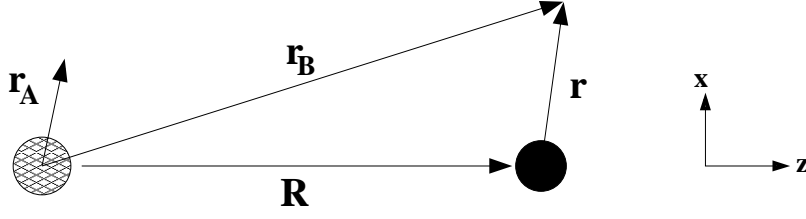
$$2\langle k_B, iv_A|ov_B, ik_A\rangle - \langle k_B, iv_A|ik_A, ov_B\rangle, \tag{3.11}$$

where $\langle i, j|k, l\rangle$ are two-electron intergals in physical notation

$$\langle i, j|k, l\rangle = \int d\mathbf{r}_1 d\mathbf{r}_2 \phi_i^*(1)\phi_j^*(2)\frac{1}{|\mathbf{r}_1 - \mathbf{r}_2|}\phi_k(1)\phi_l(2). \tag{3.12}$$

The second term in (3.11) - the exchange term - becomes exponentially small as the internuclear distance grows. That is obvious, as particle exchange happens only if the wave functions of the involved particles overlap. On the other hand, the first term in (3.11) does not cease exponentially with the internuclear distance. If subunit A and subunit B are very distant from each other, states of the total system can be represented as products of states of the isolated subunits. Choosing the coordinates according to Fig. 3.1, $|\mathbf{r}_A| \ll |\mathbf{r}_B|$, which allows us to expand the operator $1/|\mathbf{r}_i - \mathbf{r}_j|$ as [117]

$$\frac{1}{|\mathbf{r}_A - \mathbf{r}_B|} = 4\pi\sum_{l=0}^{\infty}\sum_{m=-l}^{l}\frac{1}{2l+1}\frac{r_A^l}{r_B^{l+1}}Y_{l,m}^*(\Omega_B)Y_{l,m}(\Omega_A). \tag{3.13}$$

Figure 3.1: The coordinates used to derive the asymptotic formulae.

Inserting (3.13) into the first term of (3.11) yields

$$2\langle k_B, iv_A|ov_B, ik_A\rangle = 8\pi \sum_{l=0}^{\infty} \sum_{m=-l}^{l} \frac{1}{2l+1}\langle iv_A|Y_{l,m}(\Omega_A)r_A^l|ik_A\rangle$$
$$\times \langle k_B|Y_{l,m}^*(\Omega_B)/r_B^{l+1}|ov_B\rangle. \tag{3.14}$$

In order to obtain expressions involving observables, many-particle spin and symmetry adapted states must be used. The corresponding many-particle representation of involved operators is given by [87, 97]

$$\hat{O} = \sum_{i,j} \langle i|\hat{O}|j\rangle \hat{c}_i^\dagger \hat{c}_j. \tag{3.15}$$

Assuming that a is particle and k a hole, the transition from one-particle states to 1h1p many-particle states can be achieved using the relation

$$\langle \Phi_0|\hat{O}|a, k\rangle = \sum_{ij} \langle i|\hat{O}|j\rangle \langle \Phi_0|\hat{c}_i^\dagger \hat{c}_j \hat{c}_a^\dagger \hat{c}_k|\Phi_0\rangle$$
$$= \sum_{ij} \langle i|\hat{O}|j\rangle \delta_{i,k}\delta_{j,a} = \langle k|\hat{O}|a\rangle. \tag{3.16}$$

The obtain the spin-adapted functions (3.4), an additional factor is required

$$\langle k|\hat{O}|a\rangle = \frac{1}{\sqrt{2}}\langle \Phi_0|\hat{O}|a, k, S = 0, M^s = 0\rangle. \tag{3.17}$$

Inserting (3.17) in (3.14) yields

$$2\langle k_B, iv_A|ov_B, ik_A\rangle = \sum_{l=0}^{\infty} \sum_{m=-l}^{l} \langle \Phi_0^A|\hat{D}_{l,m}^A|ik_A, iv_A; S_A = 0, M_A^s = 0\rangle$$
$$\times \langle \Phi_0^B|\hat{D}_{l,m}^B|k_B, ov_B; S_B = 0, M_B^s = 0\rangle^*, \tag{3.18}$$

where the operators $\hat{D}_{l,m}^u$ are defined by

$$\hat{D}_{l,m}^A = \sqrt{\frac{4\pi}{2l+1}}Y_{l,m}(\Omega_A)r_A^l, \tag{3.19a}$$

$$\hat{D}_{l,m}^B = \sqrt{\frac{4\pi}{2l+1}}Y_{l,m}(\Omega_B)/r_B^{l+1}. \tag{3.19b}$$

By inserterting (3.18) into (3.10) we obtain for $|\mathbf{r}_A| \ll |\mathbf{r}_B|$

$$
\begin{aligned}
W^{M_B,M_A}_{L_B,L_A} = &\sum_{\substack{m_k,m'_{ov} \\ m_{ik},m'_{iv}}} \sum_{l=1}^{\infty} \sum_{m=-l}^{l} \langle \Phi_0^A | \hat{D}_{l,m}^A | ik_A, iv_A; S_A = 0, M_A^s = 0 \rangle \\
&\times \langle \Phi_0^B | \hat{D}_{l,m}^B | k_B, ov_B; S_B = 0, M_B^s = 0 \rangle^* (l_k, l_{ov}; m_k, m_{ov} | l_k, l_{ov}; L_B, M_B)^* \\
&\times (l_{ik}, l'_{iv}; m_{ik}, m'_{iv} | l_{ik}, l'_{iv}; L_A, M_A).
\end{aligned}
\tag{3.20}
$$

(3.20) can be simplified by expanding the operators $\hat{D}$ in terms of R^{-n}. In the present work, we are only interested in the first two terms of the l series

$$
\begin{aligned}
W^{M_B,M_A}_{L_B,L_A} = \\
\sum_{m=-1}^{1} \langle \Phi_0^A | \hat{D}_{1,m}^A | ik_A, iv_A; l_{ik}, l_{iv}; L_a, M_a \rangle \langle \Phi_0^B | \hat{D}_{1,m}^B | k_B, ov_B; l_k, l_{ov}; L_b, M_b \rangle^* \\
+ \sum_{m=-2}^{2} \langle \Phi_0^A | \hat{D}_{2,m}^A | ik_A, iv_A; l_{ik}, l_{iv}; L_a, M_a \rangle \langle \Phi_0^B | \hat{D}_{2,m}^B | k_B, ov_B; l_k, l_{ov}; L_b, M_b \rangle^* \\
+ \dots,
\end{aligned}
\tag{3.21}
$$

where we have used definition of the symmetry adapted states (3.5). The $l = 1$ term corresponds to dipole transitions and $l = 2$ term to quadrupole transitions. First, we consider $l = 1$.

3.2 Dipole-Dipole Transitions

The explicit form of the operators of the first term of (3.21) is given by (3.19)

$$
\hat{D}_{1,m}^A = \sqrt{\frac{4\pi}{3}} Y_{1,m}(\Omega_A) r_A,
\tag{3.22a}
$$

$$
\hat{D}_{1,m}^B = \sqrt{\frac{4\pi}{3}} Y_{1,m}(\Omega_B) / r_B^2.
\tag{3.22b}
$$

The goal is to expand (3.22b) in terms of R^{-n}. To this end we multiply (3.22b) by 1 in the form of r_B/r_B and define the following quantities according to Fig. 3.1

$$
\mathbf{r}_B = \mathbf{r} + \mathbf{R},
\tag{3.23a}
$$

$$
\mathbf{R} = (0,0,R)^T,
\tag{3.23b}
$$

$$
\mathbf{r} = (x,y,z)^T,
\tag{3.23c}
$$

$$
\mathbf{r}_A = (x_A, y_A, z_A)^T.
\tag{3.23d}
$$

In the case $M = 0$ the operators then read

$$\hat{D}_{1,0}^A = \cos(\theta)r_A, \tag{3.24a}$$

$$\hat{D}_{1,0}^B = \cos(\theta)r_B/r_B^3, \tag{3.24b}$$

where we have used the common definition

$$Y_{1,0} = \sqrt{3/4\pi}\cos\theta. \tag{3.25}$$

Now, we can expand (3.24b) employing the Taylor expansion

$$\frac{1}{r_B^3} = \frac{1}{|\mathbf{r} + \mathbf{R}|^3} = \frac{1}{R^3}\frac{1}{(1 + 2\mathbf{R}\cdot\mathbf{r}/R^2 + r^2/R^2)^{3/2}} \tag{3.26}$$

$$= \frac{1}{R^3}(1 - \frac{3}{2}(2\mathbf{R}\cdot\mathbf{r}/R^2 + r^2/R^2) + \dots). \tag{3.27}$$

Using (3.23), (3.26), and neglecting monopol transitions and terms proportional to R^{-n}, $n > 3$ we obtain

$$\hat{D}_{1,0}^B \approx \frac{-2z}{R^3}. \tag{3.28}$$

Obviously, $\hat{D}_{1,0}^A = z_A$ and, thus, the final result for $M = 0$ reads

$$\hat{D}_{1,0}^A\hat{D}_{1,0}^B \approx \frac{z_A(-2z)}{R^3}. \tag{3.29}$$

The asymptotic operators for $M = \pm 1$

$$r_A^{\pm}(r^{\pm})^* = \frac{1}{2}\left(\frac{x_A x}{R^3} + \frac{y_A y}{R^3}\right) \tag{3.30}$$

where

$$r^{\pm} \equiv \mp\frac{1}{\sqrt{2}}(x \pm iy)$$

are obtained analogously using $Y_{1,\pm 1} = \mp\sqrt{3/8\pi}\sin\theta\exp\pm i\phi$. Adding (3.29) and (3.30) yields the asymptotic expression for the operators of the first term of (3.21)

$$\hat{V}_{l=1} \equiv \frac{1}{R^3}\sum_{m=-1}^{1} b_m\hat{\Theta}_m^A(\hat{\Theta}_m^B)^*$$

$$= \frac{x_A x + y_A y - 2z_A z}{R^3}, \tag{3.31}$$

where $b_m \equiv \{b_{-1} = 1, b_0 = -2, b_1 = 1\}$,

$$\hat{\Theta}_m^u \equiv x_u \quad \text{where} \quad x_u = \begin{cases} r_u^\pm & \text{if } m = \pm 1 \\ z_u & \text{if } m = 0 \end{cases}, \qquad (3.32)$$

and the subscript $l = 1$ indicates that (3.31) is the operator for the terms with $l = 1$.

Now, we can evaluate the $l = 1$ term of (3.21) by inserting the quantum numbers of the orbital angular momentum

$$\begin{aligned}
&L_B = L_A = 1 \\
&M_B = M_A = 0, \pm 1 \\
&l = 1, \ l' = 0 \qquad \vee \quad l = 0, \ l' = 1 \\
&m = 0, \pm 1, \ m' = 0 \quad \vee \quad m = 0, \ m' = 0, \pm 1 \\
&l = 1 \\
&m = 0, \pm 1
\end{aligned} \qquad (3.33)$$

that determine the CGCs and restrict the summation

$$\begin{aligned}
&\Rightarrow (l_x, l_y'; m_x, m_y'|l_x, l_y'; L, M) = 1, \\
&\Rightarrow \sum_{\substack{m_k, m_{ov}' \\ m_{ik}, m_{iv}'}} \rightarrow \sum_{M_A, M_B} .
\end{aligned}$$

We obtained for $l = 1$

$$\begin{aligned}
W_{L_B=1, L_A=1}^{M_B, M_A} = \sum_{M_A, M_B} \sum_{m=-1}^{1} \langle \Phi_0^A | \hat{D}_{1,m}^A | ik_A, iv_A; 1, M_A \rangle \\
\times \langle \Phi_0^B | \hat{D}_{1,m}^B | k_B, ov_B; 1, M_B \rangle^*
\end{aligned} \qquad (3.34)$$

and simplify the result further by introducing the asymptotic operators (3.31)

$$W_{L_B=1, L_A=1}^{M_B, M_A} \approx \sum_{M_A, M_B} \sum_{m=-1}^{1} b_m \langle \Phi_0 | \hat{\Theta}_m^A | ik, iv, 1, M_A \rangle \langle \Phi_0 | \hat{\Theta}_m^B | k, ov, 1, M_B \rangle^*. \qquad (3.35)$$

In (3.34) and (3.35) we have dropped the indices denoting the orbital angular momentum of the orbitals l_{iv}, l_{ik}. Henceforth, the symmetry-adapted many-particle states are denoted by $|x_u, y_u; 1, M_u\rangle$. Using (3.35) the following expression is obtained for (3.9)

$$\begin{aligned}
\Gamma_{l=1} &\equiv 2\pi |W_{1,1}^{M_B, M_A}|^2 \\
&= 2\pi \sum_{M_A, M_B} \sum_{m=-1}^{1} b_m^2 |\langle \Phi_0 | \hat{\Theta}_m^A | ik, iv, 1, M_A \rangle|^2 |\langle \Phi_0 | \hat{\Theta}_m^B | k, ov, 1, M_B \rangle|^2.
\end{aligned} \qquad (3.36)$$

To get rid of the M dependence of the dipole matrix elements the Wigner-Eckart theorem [116]

$$\langle \gamma, L, M | \hat{T}_{l,m} | \gamma', L', M' \rangle = (-1)^{L-M} \langle \gamma, L \| \hat{T}_l \| \gamma', L' \rangle \begin{pmatrix} L & l & L' \\ M & m & M' \end{pmatrix} \quad (3.37)$$

can be used. In the present case, $L = M = 0$ and $L' = l = 1$, all 3j-symbols vanish except [118]

$$m = 0, \ M' = 0 \quad \Leftrightarrow \quad \begin{pmatrix} 0 & 1 & 1 \\ 0 & 0 & 0 \end{pmatrix} = -\frac{1}{\sqrt{3}},$$

$$m = 1, \ M' = -1 \quad \Leftrightarrow \quad \begin{pmatrix} 0 & 1 & 1 \\ 0 & 1 & -1 \end{pmatrix} = \frac{1}{\sqrt{3}},$$

$$m = -1, \ M' = 1 \quad \Leftrightarrow \quad \begin{pmatrix} 0 & 1 & 1 \\ 0 & -1 & 1 \end{pmatrix} = \frac{1}{\sqrt{3}}.$$

Inserting the results of the Wigner-Eckart theorem and the definition of b_m in (3.36), the following expression is obtained

$$\Gamma_{l=1} = \frac{2\pi}{R^6} |\langle \Phi_0 | \hat{\Theta}_0^A | ik, iv, 1 \rangle|^2 |\langle \Phi_0 | \hat{\Theta}_0^B | k, ov, 1 \rangle|^2 \left(\frac{1}{9} + \frac{1}{9} + \frac{4}{9} \right)$$

$$= \frac{4\pi}{3R^6} |\langle \Phi_0 | z_A | ik, iv \rangle|^2 |\langle \Phi_0 | z | k, ov \rangle|^2, \quad (3.38)$$

where we have used (3.32) and exploited the fact that the dipole moments of different directions do not differ in atoms. Note, that this is not valid in general. If the dipole moments of different directions are not equivalent the summation over m in (3.36) would lead to differing contributions from y, x, and z in (3.38).

By replacing the squared matrix elements $\langle \Phi_0 | z_A | ik, iv \rangle$ by the definitions of the Einstein coefficient of spontaneous dipole transitions [116, 119]

$$A_{ik} = \frac{4\omega_{ik}^3}{3c^3} |\langle k | \mathbf{r} | i \rangle|^2, \quad (3.39)$$

where c is the speed of light, ω_{ik} the transition frequency, and $|k\rangle$ and $|i\rangle$ are the involved states, and the squared matrix elements $\langle \Phi_0 | z | k, ov \rangle$ by the photoionization cross sections [116, 119]

$$\sigma(E) = \frac{4\pi^2 \omega_{(ik)}}{3c} |\langle \Phi_0 | \mathbf{r} | \Psi_E \rangle|^2, \quad (3.40)$$

where $|\Phi_0\rangle$ is the ground state and $|\Psi_E\rangle$ the final continuum state, the final asymptotic expression for the decay width for dipole transitions is obtained (in a.u):

$$\Gamma_{l=1} = \frac{3}{4\pi} \left(\frac{c}{\omega} \right)^4 \frac{\sigma(\omega)}{R^6} \Gamma_\gamma \quad (3.41)$$

where $\Gamma_\gamma = A_{ik}$ denotes the radiative lifetime. The final formula (3.41) shows that the corresponding decay width falls off proportional to R^{-6}. This decrease is in agreement to the classical result for the potential energy of two interacting dipoles [117]. Moreover, in the asymptotic region the decay width is proportional to the radiative lifetime of the initial excitation of the isolated subunit A and the photoionization cross section of the isolated subunit B. Hence, we can estimate the width using properties of the isolated subunits. Asymptotic formulae can be generalized straightforward for processes with 2h2p final states or for systems consisting of molecules instead of atoms [21].

3.3 Quadrupole-Dipole Transitions

In this section the $l = 2$ term from (3.21) is considered. According to (3.19) the involved operators read

$$\hat{D}_{2,m}^A = \sqrt{\frac{4\pi}{5}} Y_{2,m}(\Omega_A) r_A^2, \tag{3.42a}$$

$$\hat{D}_{2,m}^B = \sqrt{\frac{4\pi}{5}} Y_{2,m}(\Omega_B)/r^3. \tag{3.42b}$$

As in the previous case, we derive explicit expression for these operators by employing the geometry of the system (see Fig. 3.1) and expanding in terms of R^{-n}. As above, we commence with $M = 0$: $\hat{D}_{2,0}^A$ can be expressed in terms of quadrupole moments:

$$\begin{aligned} \hat{D}_{2,0}^A &= \sqrt{\frac{4\pi}{5}} Y_{2,0}(\Omega_A) r_A^2 \\ &= \sqrt{\frac{4\pi}{5}} \sqrt{\frac{5}{16\pi}} (3\cos^2\theta - 1) r_A^2 \\ &= \frac{1}{2}(3z_A^2 - r_A^2) = \frac{3M_{zz}}{2}, \end{aligned} \tag{3.43}$$

where we have used the following definition for the quadrupole moments $Q_{\mu,\mu}$

$$\hat{Q}_{\mu,\mu} = eM_{\mu,\mu} = e(\mu^2 - 1/3r^2). \tag{3.44}$$

$\hat{D}_{2,0}^B$ is expressed in terms of dipole transitions and expanded in R^{-n}. To this end, we multiply it by 1 in form of r^2/r^2. The Taylor expansion of $1/r^5$ yields

$$
\begin{aligned}
\hat{D}_{2,0}^B &= \sqrt{\frac{4\pi}{5}} Y_{2,0}(\Omega_B)/r_B^3 = \sqrt{\frac{4\pi}{5}} \sqrt{\frac{5}{16\pi}} \frac{(3\cos^2\theta - 1)r_B^2}{r_B^5} \\
&= \frac{1}{2r^5}(3\cos^2\theta - 1)r_B^2 \\
&= \frac{1}{2r^5}(3(R+z)^2 - (R+z)^2 - x^2 - y^2) \\
&= \frac{1}{2r^5}(2(R+z)^2 - x^2 - y^2) \\
&\approx \frac{1}{2R^5}(2(R+z)^2 - x^2 - y^2)(1 - 5Rz/R^2) \\
&= \frac{1}{R^3} + \frac{-3z}{R^4} + O(R^{-5}). \tag{3.45}
\end{aligned}
$$

Terms with squared components of r are neglected. Since the R^{-3} term corresponds to forbidden monopol transitions, in the case $M = 0$ the expanded operator is given by

$$
\frac{3M_{zz}^A(-3z)}{2R^4}. \tag{3.46}
$$

Analogously, in the case $M = \pm 1$, $\hat{D}_{2,\pm 1}^A$ in terms if quadrupole moments read

$$
\begin{aligned}
\hat{D}_{2,\pm 1}^A &= \sqrt{\frac{4\pi}{5}} Y_{2,1}(\Omega_A)r_A^2 \\
&= \mp\sqrt{\frac{4\pi}{5}}\sqrt{\frac{15}{8\pi}}\cos\theta\sin\theta\exp(\pm i\phi)r_A^2 \\
&= \mp\sqrt{\frac{3}{2}}z(x\pm iy) = \mp\sqrt{\frac{3}{2}}(M_{xz}\pm iM_{yz}), \tag{3.47}
\end{aligned}
$$

and the asymptotic $\hat{D}_{2,\pm 1}^B$ in terms of dipole moments is given by

$$
\begin{aligned}
\hat{D}_{2,\pm 1}^B &= \sqrt{\frac{4\pi}{5}}Y_{2,1}(\Omega_B)/r_B^3 = \mp\sqrt{\frac{4\pi}{5}}\sqrt{\frac{15}{8\pi}}\frac{\cos\theta\sin\theta\exp(\pm i\phi)r_B^2}{r_B^5} \\
&= \mp\sqrt{\frac{3}{2}}\frac{(R+z)(x\pm iy)}{R^5}(1 - \frac{5}{2}(2\boldsymbol{R}\cdot\boldsymbol{r}/R^2 + r^2/R^2) + \ldots) \\
&= \mp\sqrt{\frac{3}{2}}\frac{x\pm iy}{R^4} + O(\frac{1}{R^5}). \tag{3.48}
\end{aligned}
$$

Thus, the asymptotic operator for $M = \pm 1$ reads

$$
\frac{6(M_{xz}^A x + M_{yz}^A y)}{2R^4} \tag{3.49}
$$

and the total one

$$\hat{V}_{l=2} \equiv \frac{6(\hat{Q}^A_{xz}x + \hat{Q}^A_{yz}y) - 9\hat{Q}^A_{zz}z}{2R^4}. \tag{3.50}$$

In (3.47), (3.49), and (3.50) we made use of the definition

$$\hat{Q}_{\mu,\nu} = eM_{\mu,\nu} = e\mu\nu. \tag{3.51}$$

For $M = \pm2$ the are no non-vanishing terms proportional to R^{-n}, $n \leq 4$ in the expansion series of $\hat{D}^B_{2,2}$.

According to (3.50), the asymptotic expression for the decay width is given by

$$\Gamma_{l=2} \approx 2\pi \sum_m \sum_{M_A M_B} |Q^{M_A}_{mz}|^2 |D^{M_B}_m|^2 \tag{3.52}$$

In (3.52) we used the definitions

$$Q^{M_A}_{mz} = \langle\Phi_0|\hat{\Xi}^A_m|ik_A, iv_A, 2, M_A\rangle, \tag{3.53a}$$
$$D^{M_B}_m = d_m\langle\Phi_0|\hat{m}^B|k_B, ov_B, 1, M_B\rangle, \tag{3.53b}$$

where

$$\hat{\Xi}^A_m = \begin{cases} \hat{Q}_{xz} & \text{if } m = -1 \\ \hat{Q}_{zz} & \text{if } m = 0 \\ \hat{Q}_{yz} & \text{if } m = +1 \end{cases}$$

$$d_m = \begin{cases} 3 & \text{if } m = -1 \\ -9/2 & \text{if } m = 0 \\ 3 & \text{if } m = +1 \\ 0 & \text{if } m = \pm2 \end{cases}$$

In order to express the widths in (3.52) in terms of observables the proportionality factors of the $Q_{\mu\nu}$ contributing to the widths and the total transition moment Q occurring in the corresponding Einstein coefficient [116]

$$A_{ki} = \frac{\omega^5}{10\hbar c^5}|Q|^2, \tag{3.54}$$

where

$$Q = \sum_{\mu\nu} Q_{\mu\nu}, \tag{3.55}$$

are to be determined. Before we can do that, we have to evaluate the general Q and $Q_{\mu\nu}$, respectively, for a certain transition. Here, we are interested in

transition between an s and a d state. In order to evaluate the corresponding matrix elements, $\hat{Q}_{\mu\nu}$ are expressed in terms of spherical harmonics

$$\hat{Q}_{xx} = e(x^2 - 1/3r^2) = er^2(\sin^2\theta\cos^2\theta - 1/3)$$

$$\hat{Q}_{yy} = e(y^2 - 1/3r^2) = er^2(\sin^2\theta\sin^2\theta - 1/3)$$

$$\hat{Q}_{zz} = e(y^2 - 1/3r^2) = er^2(\cos^2\theta - 1/3)$$

$$\hat{Q}_{xz} = Q_{zx} = e(x^2 - 1/3r^2) = er^2\cos\theta\sin\theta\cos\phi$$

$$\hat{Q}_{xy} = Q_{yx} = e(x^2 - 1/3r^2) = er^2\sin^2\theta\sin\phi\cos\phi$$

$$\hat{Q}_{yz} = Q_{zy} = e(x^2 - 1/3r^2) = er^2\cos\theta\sin\theta\sin\phi$$

$$\Updownarrow \qquad \Updownarrow \qquad \Updownarrow \qquad \Updownarrow \qquad \Updownarrow$$

$$\hat{Q}^Y_{xx} = er^2\left[\sqrt{\frac{4\pi}{30}}(Y_{2,2} + Y_{2,-2}) - \frac{1}{3}\sqrt{\frac{4\pi}{5}}Y_{2,0}\right]$$

$$\hat{Q}^Y_{yy} = -er^2\left[\sqrt{\frac{4\pi}{30}}(Y_{2,2} + Y_{2,-2}) - \frac{1}{3}\sqrt{\frac{4\pi}{5}}Y_{2,0}\right]$$

$$\hat{Q}^Y_{zz} = er^2 6\sqrt{\frac{4\pi}{5}}Y_{2,0}$$

$$\hat{Q}^Y_{xz} = er^2\sqrt{\frac{2\pi}{15}}(Y_{2,1} + Y_{2,-1})$$

$$\hat{Q}^Y_{xy} = -ier^2\sqrt{\frac{2\pi}{15}}(Y_{2,2} - Y_{2,-2})$$

$$\hat{Q}^Y_{yz} = -ier^2\sqrt{\frac{2\pi}{15}}(Y_{2,1} - Y_{2,-1})$$

because having them in this form allows us to employ the Wigner-Eckart theorem for the evaluation

$$\begin{aligned}
Q^M_{\mu\nu} &= \langle ik_A, iv_A, L = 2, M|Q^Y_{\mu\nu}|\Phi^A_0, L' = 0, M' = 0\rangle \\
&= \langle \Phi_d(\mathbf{r})Y_{2,M}|Q^Y_{\mu\nu}|\Phi_s(\mathbf{r})Y_{0,0}\rangle \\
&= \langle \Phi_d(r)|er^2|\Phi_s(r)\rangle_r \langle Y_{2,M}|Q^Y_{\mu\nu}|Y_{0,0}\rangle_{\theta,\phi},
\end{aligned} \qquad (3.56)$$

where the subscripts r and θ, ϕ indicate the variables over which the each integration is performed. Since squared matrix elements $|Q_{\mu,\nu}|^2$ occur in the definition of the width and the Einstein coefficient, we consider

$$|Q_{\mu,\nu}|^2 = \sum_M |Q^M_{\mu,\nu}|^2 = |\langle \Phi_d(r)|er^2|\Phi_s(r)\rangle_r|^2 \underbrace{\sum_M |\langle Y_{2,M}|Q^Y_{\mu\nu}|Y_{0,0}\rangle_{\theta,\phi}|^2}_{\equiv q_{\mu\nu}}.$$

$$(3.57)$$

To evaluate the $q_{\mu\nu}$ the quantum numbers of the s and the d state were inserted. As a result, only the following matrix elements with non-vanishing $3j$-symbols

$$m = 0, \; M' = 0 \quad \Leftrightarrow \quad \begin{pmatrix} 0 & 2 & 2 \\ 0 & 0 & 0 \end{pmatrix} = \frac{1}{\sqrt{5}},$$

$$m = \mp 1, \; M' = \pm 1 \quad \Leftrightarrow \quad \begin{pmatrix} 0 & 2 & 2 \\ 0 & \mp 1 & \pm 1 \end{pmatrix} = -\frac{1}{\sqrt{5}},$$

$$m = \mp 2, \; M' = \pm 2 \quad \Leftrightarrow \quad \begin{pmatrix} 0 & 2 & 2 \\ 0 & \mp 2 & \pm 2 \end{pmatrix} = \frac{1}{\sqrt{5}}.$$

contribute. The values of $q_{\mu,\nu}$ for all directions are given in Tab. 1.

$q_{\mu\nu}$	$\sum_M |\langle Y_{2,M}|Q^Y_{\mu\nu}|Y_{0,0}\rangle_{\theta,\phi}|^2$
q_{xx}	$\frac{1}{5}\left(\frac{1}{9}\frac{4\pi}{5} + \frac{4\pi}{30} + \frac{4\pi}{30}\right) = \frac{1}{5}\frac{16\pi}{45}$
q_{yy}	$\frac{1}{5}\frac{16\pi}{45}$
q_{zz}	$\frac{1}{5}\frac{144\pi}{5}$
$q_{xy} = q_{yx}$	$\frac{1}{5}\frac{4\pi}{15}$
$q_{xz} = q_{zx}$	$\frac{1}{5}\frac{4\pi}{15}$
$q_{yz} = q_{zy}$	$\frac{1}{5}\frac{4\pi}{15}$

Table 1: $q_{\mu\nu}$ values for all directions. The factors $1/5$ stem from the 3j-symbols.

Now, we can rewrite the Einstein coefficient in terms of $q_{\mu\nu}$

$$A_{ki} = \frac{\omega^5}{10\hbar c^5}|Q|^2 \sum_{\mu,\nu} q_{\mu\nu} \tag{3.58}$$

and insert the values from Tab. 1. Thus, we obtain

$$A_{ki} = \frac{1400\pi}{45}\frac{\omega^5 |Q|^2}{50\hbar c^5} \quad \Leftrightarrow \quad |Q|^2 = \frac{45}{1400\pi}\frac{A_{ki}50\hbar c^5}{\omega^5}. \tag{3.59}$$

As the final step, we can calculate the proportionality factor between the squared total quadrupole moment and the partial ones contained in the expression of the

width (3.50). The factor is given by

$$|Q_{\mu\nu}|^2 = |Q|^2 q_{\mu\nu}. \tag{3.60}$$

In (3.50) only the following partial squared quadrupole transition moments are required

$$|Q_{xz}|^2 = |Q_{yz}|^2 = \frac{4\pi}{15} \frac{45}{1400\pi} \frac{A_{ki}50\hbar c^5}{\omega^5} = \frac{3}{350} \frac{A_{ki}50\hbar c^5}{\omega^5}, \tag{3.61a}$$

$$|Q_{zz}|^2 = \frac{162}{175} \frac{A_{ki}50\hbar c^5}{\omega^5}. \tag{3.61b}$$

 Taking into account that the dipole moment of atomic systems is isotropic, the total widths is given by

$$\Gamma_{l=2} = \frac{2\pi}{5} |D_z|^2 \sum_m |Q_{mz}|^2 \tag{3.62}$$

where 1/5 stems averaging over the initial states and using the definition (3.61) $|Q_{mz}|^2$ is defined by

$$|Q_{mz}|^2 = \begin{cases} |Q_{xz}|^2 & \text{if } m = -1 \\ |Q_{zz}|^2 & \text{if } m = 0 \\ |Q_{yz}|^2 & \text{if } m = +1 \end{cases}. \tag{3.63}$$

The dipole moment $|D_z|^2$ is replaced by the photoionization cross section $\sigma(\omega)$ using the relation

$$|D_z|^2 = \frac{1}{4\pi^2} \frac{c}{\omega} \sigma(\omega). \tag{3.64}$$

Now, we can state the asymptotic expression for the decay width of quadrupole excitations

$$\Gamma_{l=2} = \frac{1323}{14\pi} \left(\frac{c}{\omega}\right)^6 \frac{\Gamma_\gamma \sigma(\omega)}{R^8}. \tag{3.65}$$

The final formula (3.41) is proportional to R^{-8}. This the classical dependence of the potential energy of a dipole interacting with a quadrupole [117]. Moreover, the asymptotic expression of decay width is determined by the radiative lifetime of the initial quadrupole excitation $\Gamma_\gamma = A_{ki}$ on isolated subunit A and photoionization cross section of the isolated subunit B. Note, that the quadrupole excitations usually exhibit very long lifetimes.

An asymptotic formula of the decay width of a dipole allowed excitation whose energy is at or very close to a Cooper minimum [120] of the photoionization cross section of the neighbor can be derived analogously. At a Cooper minimum

the first order term of the photoionization cross section becomes zero because it changes its sign. However, the total photoionization cross section is larger than zero due to the terms of higher order. Such points are known as Cooper minima [120] because the total photoionization cross section usually exhibits a local minimum at such points. Hence, the first non-vanishing term is the one due to quadrupole transitions. The derivation of the formulae for those cases, differs only by the definition used: the definition of Einstein coefficients of a dipole transition and the photoionization cross section due to quadrupole transitions must be used. In order to get the definition of the latter we consider the expansion of the total cross section [121]

$$\sigma(\omega) = \frac{4\pi^2\omega}{3c} \left(\left[|D|^2 + |M|^2 + \frac{k^2}{20}|Q|^2 \right] \right). \tag{3.66}$$

where M denotes the magnetic dipole and k is the absolute value of the photon wave vector. According to (3.66) the quadrupole cross section is given by

$$\sigma(\omega) = \frac{\pi^2\omega^3}{15c^3} |\langle \Phi_0 | \sum Q_{\mu,\nu} | \Psi_\omega \rangle|^2 \tag{3.67}$$

and, thus, the asymptotic formula of the ICD widths of a dipole allowed excitation at a Cooper minimum of the photoionization cross section reads

$$
\begin{aligned}
\Gamma_{l=2} &= \frac{3}{2\pi} \frac{1323}{70} \left(\frac{c}{\omega}\right)^6 \frac{\Gamma_\gamma \sigma(\omega)}{R^8} \\
&= \frac{567}{20\pi} \left(\frac{c}{\omega}\right)^6 \frac{\Gamma_\gamma \sigma(\omega)}{R^8}.
\end{aligned} \tag{3.68}
$$

Calculation of Excitation-Transfer-Ionization (ETI) Widths

In order to demonstrate the efficiency and the accuracy of the Fano-Stieltjes-Lanczos (FSL) method, as applied to the calculations of interatomic decay widths of excited states, we determine ETI [19] widths. ETI is a non-radiative decay pathway of outer-valence excitations in clusters, which sets in, if the excitation energy is sufficient to ionize another cluster constituent. The outer valence excitation relaxes by transferring its energy to another cluster subunit and ionizing it (see Fig. 1.1). At interatomic distances of a few Å between the cluster constituents this decay has been shown to be orders of magnitude faster than the competing radiative decay [19].

In the present work, we calculate ETI widths in NeAr and HCN·Mg_n, $n = 1, 2$. The calculations in the comparatively simple NeAr serve to test the selection schemes for the Q and P subspaces necessary to carry out the FSL method [51] and to investigate the quality of the results with respect to the number of the final states used. Moreover, we use this example to depict the course of the FSL method exemplarily. HCN·Mg_n clusters [122] provide us with a realistic system where ETI is possible following an excitation of HCN. At asymptotic internuclear distances we compare the FSL widths to the predictions of the virtual photon transfer model (see Sec. 3) and, where available, to widths obtained previously for these clusters in CAP-ADC calculations [19].

4.1 Applications

ETI in NeAr

In this section widths of Ne*[$2p^{-1}3s$ (^1P)]Ar excitations are calculated. The excitation energy of the $2p^{-1}3s$ (^1P) state of isolated Ne is 16.85 eV [123]. The ionization potential of $3p$ electrons of isolated Ar lies at 15.76 eV [123]. Therefore, the ETI channel is open at asymptotic internuclear distances. On the other hand, the excitation energy is not sufficient to produce either excited states of Ar$^+$ or doubly ionized states. We verified in a separate *ab initio* calculation that the ETI channel remains open at all internuclear distances of interest (between 3 Å and 10 Å) and that no other decay channels occur.

The first step in the course of the FSL approach is a Hartree-Fock (HF) calculation which provided the MOs, their energies, and the corresponding two-electron

integrals. If the HF calculation was successful, one can proceed with the description of the involved excited states. In the framework of the FSL method, the configuration space Q, which describes the resonant states, and the configuration space P, which describes the non-resonant final states of the decay, must be specified. Which occupied MOs are selected depends on the character of the involved states and the open channels.

For the current example, ETI in NeAr originating from the $Ne2p^{-1}3s$ (^1P) excitation, we employed the ADC(2)x method to calculated the resonant initial and the non-resonant final states. Hence, corresponding 1h1p and 2h2p configurations must be specified. In the NeAr cluster the triply degenerate ^1P term of Ne splits into $^1\Sigma$ and $^1\Pi$ states. At first, we consider the decay of $^1\Pi$ states. The electronic configurations of the ground state of Ne and Ar are $(He)2s^22p^6$ and $(Ne)3s^23p^6$, respectively. The $1s$ orbital of Ne and the $1s2s2p$ orbitals of Ar are frozen in the calculations. Tests showed that neglecting those orbitals does not change the calculated properties of the involved states and widths significantly. The configuration space Q describing the Ne $2p^{-1}3s$ $(^1\Pi)$ state consists of all configurations of 1h1p character of appropriate symmetry having a hole in the Ne $2p$ orbital. To account for intra-atomic electron correlation we also include 1h1p configurations with a hole in the Ne $2s$ orbital and all 2h2p configurations with two holes in the Ne $2p$ orbitals. Since only the ETI channel is open, the final states of the decay are 1h1p states with a hole in the Ar $3p$ orbitals and an electron in the continuum. To describe these states we include all 1h1p configurations with a hole in the MOs corresponding to Ar $3p$. To account for intra-atomic correlation in the final states we add all 2h2p configurations with two holes in the Ar $3p$ orbitals.

The results of both the HF and the subsequent FSL calculation depend strongly on the atomic basis sets employed. Thus, after the ADC method and the configuration spaces have been chosen, basis sets appropriate to describe the states must be determined. First, we obtained a basis proper to describe Ne $2p^{-1}3s$ $(^1\Pi)$ excitations. To this end, the following empiric procedure is suitable: A good basis set of origin to describe excited state of $^1\Sigma$ and $^1\Pi$ symmetry in small clusters consisting of rare gas and alkali earth atoms is the aug-cc-pVTZ Gaussian basis set [124]. It is used in order to obtain a reference energy which is compared to the literature value. If the difference is large all steps of the calculation should be checked carefully. On the other hand, if the agreement is decent, the energy can be converged with respect to the basis set by gradually adding Rydberg-like Gaussian functions [125] of s, p, and d symmetry. After each augmentation, the energy must be recalculated. The number of functions of different symmetry added in every step depends on the virtual orbital of the excitation of interest. For example, in order to describe an $Xp^{-1}Ys$ excitation, more functions exhibiting s symmetry should be added. In the present case, a suitable ansatz is to recalculate the energy after adding $2s$, $1p$, and $1d$ function(s). If the excitation energy does

not change at the third digit, it can be considered as having converged. In the case of the $2p^{-1}3s$ ($^1\Pi$) excitation in Ne, we found that the energy is converged employing the aug-cc-pVTZ Gaussian basis set [124] augmented with $12s$, $6p$, $4d$ Rydberg-like Gaussian functions [125] centered on Ne. The calculated energy of the $2p^{-1}3s$ ($^1\Pi$) resonance is 16.7 eV (0.614 a.u.), in good agreement with the literature value of 16.85 eV. The Hamiltonian matrix representing the decaying states of the decay had a dimension of 21200. Since by construction the decaying state lies near the lower spectral boundary, we used the Davidson diagonalization method [126] to compute it.

The final states of the ETI in NeAr are represented by Ne in its ground state, Ar^+, and an electron in the continuum. Consequently, the task to determine a basis set which is appropriate to describe the final states, means to determine basis set appropriate to represent Ar^+ and the outgoing electron. In general, the continuum states of the outgoing electron are physically given by plane waves (see Sec. 2.1). The Stieltjes method used in the FSL approach is based on the idea that matrix elements of a bound and a continuum state (2.18) can be evaluated using an $\mathcal{L}^2$ spectrum to represent the continuum state, since the bound part of the resonant state is non-zero only in a finite spatial region. As a consequence, the matrix element is well described if the continuum state can be reproduced in that region. To represent plane waves in the final spatial region diffuse $\mathcal{L}^2$ functions can be used. Thus, the outgoing electron can be described by augmenting the basis set with diffuse functions. Whether an appropriate description can be achieved depends on the kinetic energy of the outgoing electron. The higher the kinetic energy is the more difficult it is to reproduce the corresponding plane waves using $\mathcal{L}^2$ functions. To obtain a higher flexibility in the basis set it can be helpful to augment the basis sets of all cluster constituents by diffuse functions. In the case of small systems, the introduction of ghost atoms [127] might help as well. The basis set can be considered to be appropriate when the energies of the final spectrum and the width do not change significantly on adding diffuse functions. Usually, the energies converge more rapidly and, thus, their convergence is a byproduct of the convergence of the width. So, the actual task is to converge the width. Within the FSL method, the smoothed spectra of order n consisting of

$$\{\epsilon_j, \gamma_j\}^{(n)}, \tag{4.1}$$

pairs resulting from Stieltjes imaging (see Sec. 2.3) are investigated in order to see whether the width has converged. At the energy of the resonant initial state, the interpolated smoothed spectra approximate the width. If the interpolated spectra do not change on augmenting the basis set further the basis set is suitable to describe the final states.

As in quest of a basis for the decaying state, we started from the Ar aug-cc-pVTZ Gaussian basis set [124]. Employing this basis set, the configuration space representing the final states P contained 50 1h1p configurations and about 6000
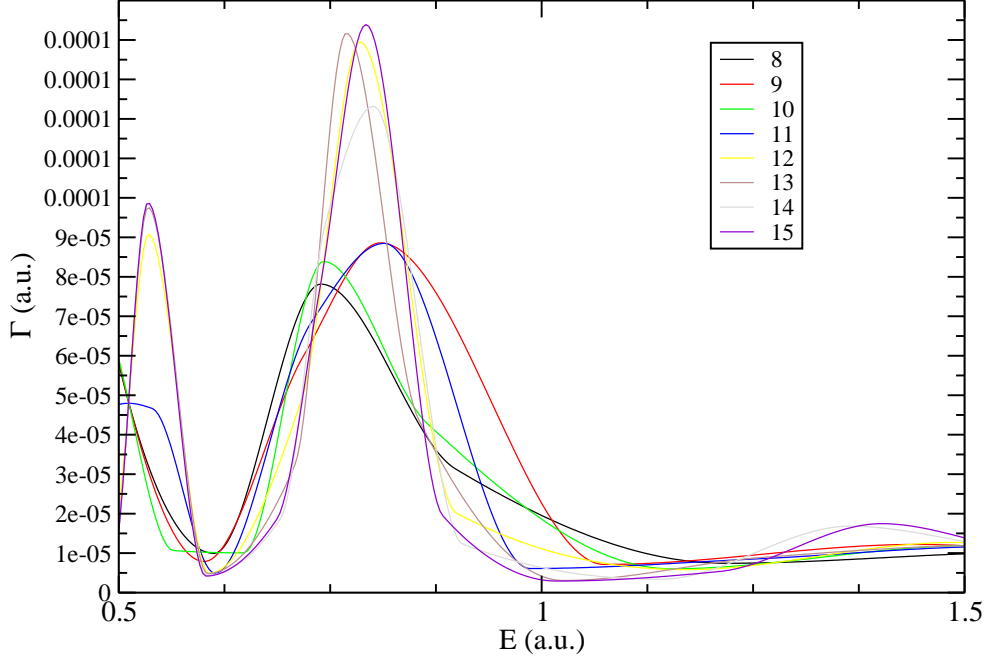
Figure 4.1: Interpolated smoothed spectra at an internuclear distance of 4 Å using the reference basis set.

2h2p configurations. We used all 1h1p configurations to set up the starting block required to perform the Lanczos method and conducted 20 iterations. That the spectrum has been converged with respect to the number of iterations can be verified by examining the spectrum in the energy region around the resonant state: if the number of eigenstates does not change after increasing the number of Lanczos iterations the spectrum has converged with respect to the number of iterations. The resulting interpolated smoothed spectra of order $8 \leq n \leq 15$ are depicted in Fig. 4.1. The smoothed spectra of lower and higher orders are neglected since, in general, spectra of order $n < 7$ consist of so less points that they are usually to rough to be useful and spectra of order $n > 17$ tend to oscillate and, as a consequence, are often not reliable. By looking at the graphs in Fig. 4.1, one can see, that the graphs differ significantly in the energy region of around the resonant initial state (0.55 to 0.7 a.u.). According to the Chebychev relations (2.73) that indicates that the spectra obtained by means of a certain finite number of moments do not bracket the true widths well enough to make a reasonable choice. Furthermore, the spectra change significantly on adding diffuse functions.

Consequently, the basis set has to be expanded in order to improve the description. Since the decaying state exhibits Π symmetry and the $3p$ holes can be of Σ or Π symmetry, the outgoing electron must represented by waves of Σ and Π symmetry. So, we are suppose to add diffuse s and p functions when augmenting the Ar basis set. To this end, we augmented the original basis sets gradually by $2s$, $2p$, and $1d$ diffuse function(s) whose exponents we determine by the even tempered scheme [128, 129] taking the exponent of the most diffuse function of the original basis set as the point of origin. We repeated the outlined convergence check until the smoothed spectra became stable. Here, this occurred using the aug-cc-pVTZ basis set augmented by $6s$, $6p$, and $3d$ functions. The configuration space in this basis contained 18500 configurations of which 80 were 1h1p ones. We employed all 80 1h1p configurations to define the starting block of the Lanczos method and carried out 20 iterations. The corresponding interpolated spectra
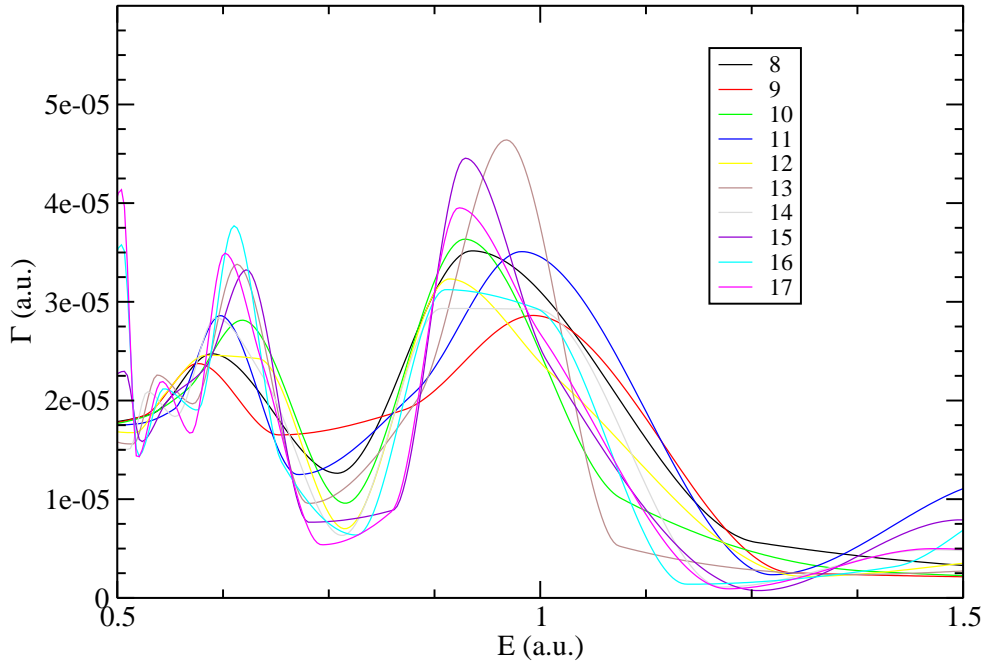
Figure 4.2: Interpolated smoothed spectra at an internuclear distance of 4 Å using the final basis set.

are given in Fig. 4.2. Except extremal orders, the different smoothed spectra are close to each other in the energy region of interest. Thus, the true width is decently bracketed there. Although the spectra of extremal orders deviate from the spectra of middle orders, they are converged and do not change on augmenting

the basis set further. Note that it can happen, that all spectra have stabilized but are not as alike as desired. In such cases the widths can only determine with respect to an relatively high uncertainty. Here, most of the spectra exhibit an uniform behavior even at higher energies.

The widths can be read directly from Fig. 4.2. However, to ensure that the chosen widths is well bracketed in the sense of the Chebychev relations, interpolations from spectra of more than one order are generated. For example, averaging over two orders means taking all the pairs of second $\{\epsilon_j, \gamma_j\}^{(2)}$ and of third order $\{\epsilon_j, \gamma_j\}^{(3)}$, to form a new set

$$\{\epsilon_j, \gamma_j\}^{(2\cup3)} = \{\epsilon_j, \gamma_j\}^{(2)} + \{\epsilon_j, \gamma_j\}^{(3)}. \tag{4.2}$$

and do the interpolation based on $\{\epsilon_j, \gamma_j\}^{(2\cup3)}$. In principle, all spectra could be used to obtain one graph including all smoothed pairs. However, based on our experiences, it is not helpful to take more than three or four orders at once. Fig. 4.3 and Fig. 4.4 depict the interpolated smoothed spectra where, respectively, two or three orders have been used for the interpolations.   By comparing the
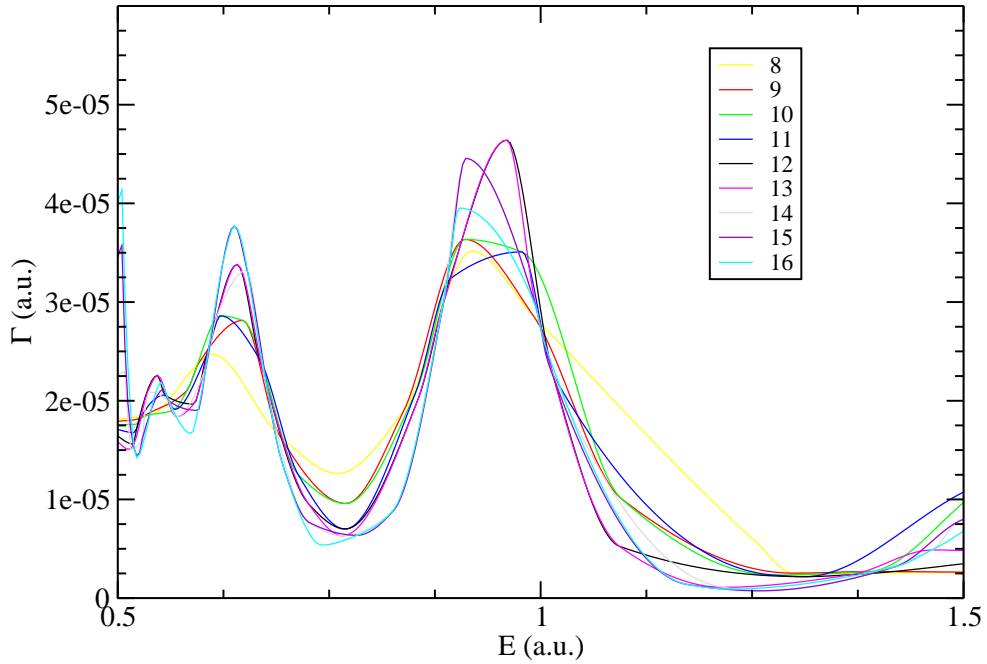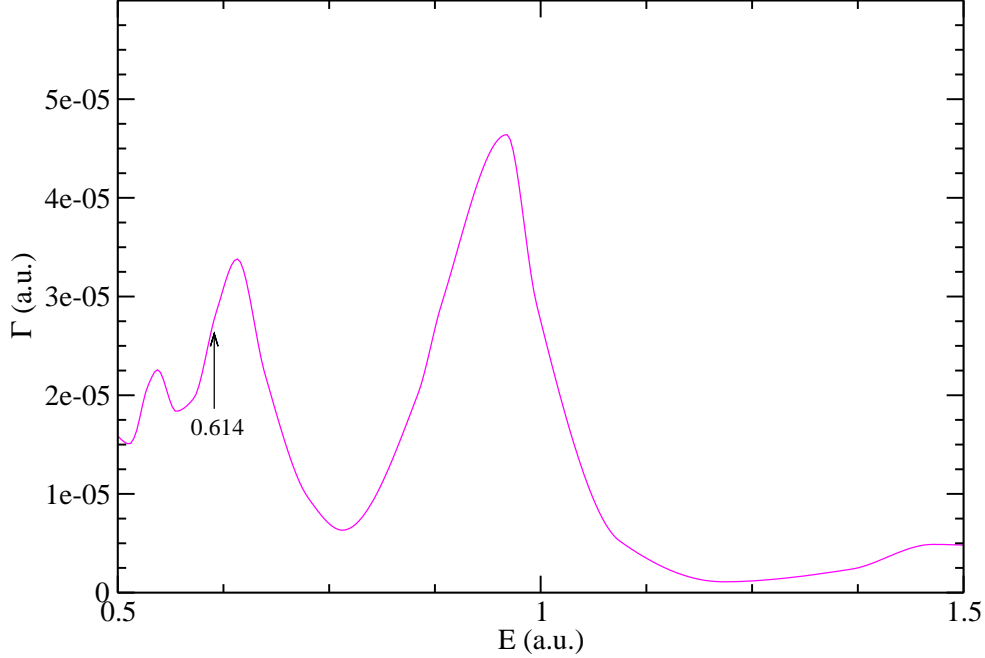

Figure 4.3: Interpolated smoothed spectra at an internuclear distance of 4 Å averaged over two orders.
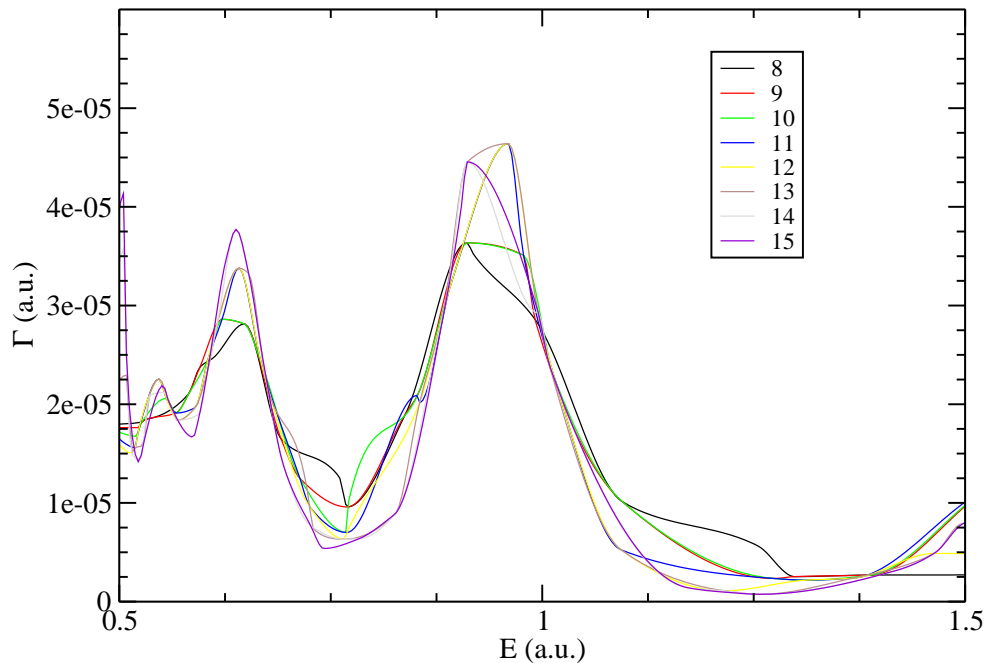
Figure 4.4: Interpolated smoothed spectra at an internuclear distance of 4 Å averaged over three orders.

graphs to the graphs from Fig. 4.2, one can see that the resulting interpolated graphs are closer to each other. Especially, the averaging over two orders produces good results. We read the value of the widths from graph corresponding to the averaging over the orders 8 and 9 given in Fig. 4.3 and separately depicted in Fig. 4.5. In order to get the widths as a function of the internuclear distance, the above described procedure has to be repeated at all cluster geometries of interest. If the resulting width exhibits a smooth shape as a function of R, the widths can be considered as having converged. If, on the other hand, it shows an erratic behavior at some geometries, the calculations around those points should be checked in detail. Especially at geometries where the electronic structure of the system changes rapidly that can occur.

In the course of [25] we carried out a study on the convergence with the number of block Lanczos iterations using the basis sets discussed above. The predominantly 1h1p character of the final states suggests that the best starting block consists of all 1h1p configurations of the final subspace (80 in this case). Using this starting block, we performed Lanczos diagonalization with 1, 5, 10, and 30 block iterations, obtaining 80, 400, 800, and 2400 final states, respectively. The

Figure 4.5: Selected interpolated smoothed spectra at an internuclear distance of 4 Å averaged over two orders. The arrow indicates the value of the width taken at the energy of the resonant state.

calculated widths are given in Fig. 4.6. The figure shows that the decay width is converging extremely fast indicating an excellent choice of the starting vectors for the Lanczos procedure.

In order to check whether the FSL method reproduces the dependence of the ETI rate on the symmetry of the initial state [21] correctly we applied it to the calculation of the width of the Ne $2p^{-1}3s$ ($^1\Sigma$) excitation in the same cluster. We employed the same configuration subspaces and the same Gaussian basis sets as for the $^1\Pi$ state. Although the resulting subspaces are not completely equivalent due to the different symmetry of the initial and final states, we utilized the parameters (block size 80 and 30 block Lanczos iterations) obtained from the study of convergence of the $2p^{-1}3s$ ($^1\Pi$) excitations. For comparison we plotted both graphs in Fig. 4.7. One first notices that the width of Ne $2p^{-1}3s$ ($^1\Sigma$) excitations is larger than the width of $2p^{-1}3s$ ($^1\Pi$) excitations, in accordance with theory [21]. At interatomic distances R larger than 6 Å the widths are proportional to R^{-6} and the quotient of both widths is equal to four, which is exactly the value predicted by the virtual photon transfer model [21] at large interatomic distances. The absolute values are also in good agreement with the
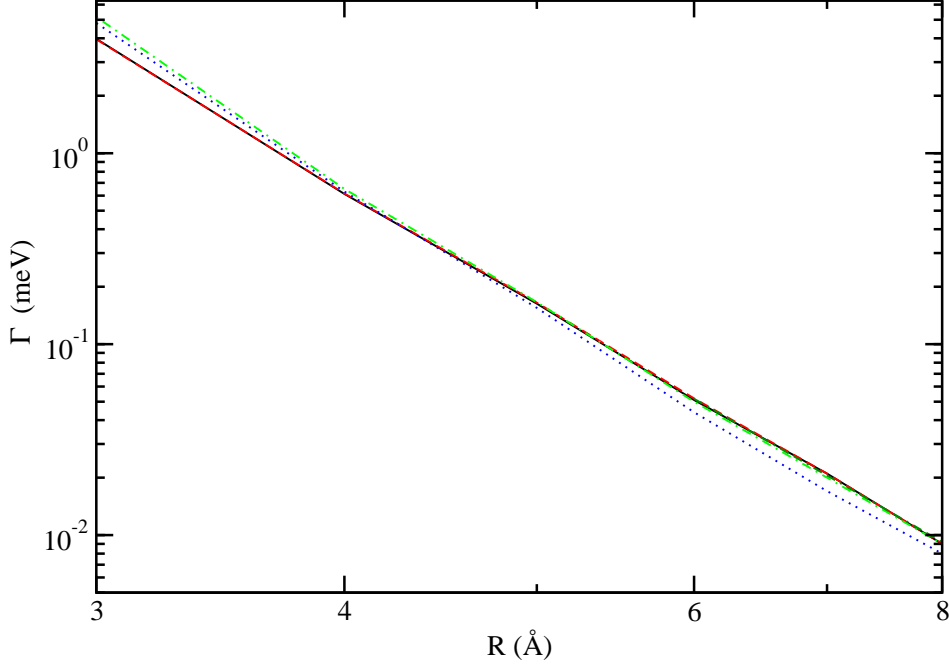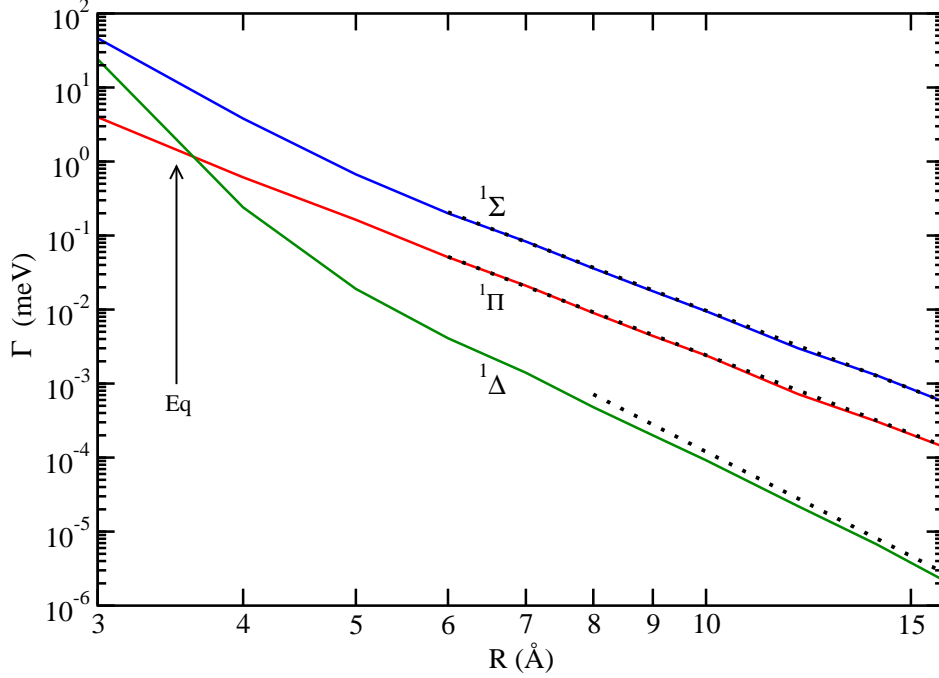
Figure 4.6: ETI widths of the $2p^{-1}3s$ ($^1\Pi$) excitation of Ne in NeAr clusters as a function of the interatomic distance for different numbers of block Lanczos iterations. The starting block is spanned by 80 1h1p configurations. The widths are shown after one (dotted line), five (dash-dotted line), 10 (dashed line), and 30 (full line) iterations. Note the fast convergence.

analytical predictions. At small interatomic distances the width of Ne $2p^{-1}3s$ ($^1\Sigma$) excitation increases faster than the width of the $^1\Pi$ excitation due to the larger orbital overlap between the monomers for the states of Σ symmetry. The resulting lifetime of the Ne $2p^{-1}3s$ ($^1\Sigma$) excitation in NeAr at the equilibrium distance of 3.5 Å is 55 fs which is four orders of magnitude shorter than the 1.6 ns lifetime of the competing radiative decay [25].

The interatomic decay widths have been calculated so far for optically allowed initial states. However, we further tested the method by applying it to dipole forbidden but quadrupole allowed transitions. As has been demonstrated in Ref. [16] the ICD width of quadrupole allowed ionized initial states decreases with R^{-8} at large interatomic distances. The expression for the ETI width derived in Sec. 3 similarly to Ref. [16, 21] reads

$$\Gamma = \frac{1323}{14\pi} \left(\frac{c}{\omega}\right)^6 \frac{\sigma(\omega)}{R^8} \Gamma_{rad} \tag{4.3}$$

Figure 4.7: ETI widths of the Ne $2p^{-1}3s$ ($^1\Pi$), $2p^{-1}3s$ ($^1\Sigma$), and $2p^{-1}3p_z$ ($^1\Delta$) excitations in NeAr clusters as a function of the interatomic distance. We carried out 20 block Lanczos iterations with a block size of 80 (see the text for more details). The predictions of the asymptotic formula are depicted as dotted lines. Note the good agreement of the calculated widths and the analytical predictions. The dotted line close to the graph of the optically forbidden Δ excitation is proportional to R^{-8}.

where ω is the frequency of the virtual photon, $\sigma(\omega)$ is the photoionization cross section of the neighbor Ar, and Γ_{rad} is the radiative width of the excited state of isolated Ne due to photon emission. In this instance, we would like primarily to check whether the FSL method can reproduce the correct asymptotic gradient and, in addition, check whether our approach works for very small numerical values of the width which occur in this case due to its fast decrease with R.

To this end we calculated the decay width of Ne $2p^{-1}3p$ ($^1\Delta$) excitations in NeAr (see Fig. 4.7). The energy value of this excitation is given in the literature with 18.63 eV [123]. We employed the same subspaces and the same Gaussian basis sets as in the calculations above. Using this setup we obtained an excitation energy of 18.8 eV and the decay rate shown in Fig. 4.7. One can see that as the interatomic distance grows the decay width decreases much faster than the decay width of the optically allowed Ne $2p^{-1}3s$ excitations. This can be explained by the fact that the moment the orbital overlap becomes negligible, the rate falls off

as R^{-8} and not as R^{-6} as in the previous case. It is notable that our *ab initio* approach yields the correct R^{-8} behavior even at very large interatomic distances where the absolute numbers are very small.

ETI in HCN·Mg

As a further test we applied the FSL method to the calculation of ETI widths of the $5\sigma\pi^*$ excitation of the HCN molecule in HCN·Mg$_n$, $n = 1, 2$ clusters. The corresponding ETI widths of these systems have been calculated previously with the CAP-ADC method [19]. In addition, all properties of the constituents necessary to evaluate the asymptotic formulae are known, giving us the opportunity to compare the results. The first step was again to define the subspaces of the initial state and final states of the decay. The Hartree-Fock electronic configurations of the ground states of HCN and Mg are $1\sigma^2 2\sigma^2 3\sigma^2 4\sigma^2 5\sigma^2 1\pi^4$ and $(Ne)3s^2$, respectively. By 5σ we understand the non-binding orbital on N. To describe the initial 1h1p $5\sigma\pi^*$ excitation we included all configurations of 1h1p character with a vacancy in the 5σ molecular orbital (MO). To account for electron correlation in the initial state we included, additionally, all 1h1p configurations with a vacancy in a 1π MO and all 1h1p configuration with a vacancy in the 4σ MO. We also added all 2h2p configurations with two vacancies in either 5σ, 4σ, or 1π MOs, and all 2h2p configurations with one vacancy in the 5σ and another in either the 4σ MO, or in the 1π MO.

The final states of the ETI process differ according to the number of neighboring Mg atoms. In the case of HCN·Mg the bound part of the final states consist of HCN in its ground state and Mg$^+$ in its ground state. To describe these states accounting for electron correlation, we included in the configuration space all 1h1p and 2h2p states with one or two holes in the Mg $3s$ orbital. In the calculation of the final states we took as starting vectors of the Lanczos procedure all the 1h1p configurations. After the block Lanczos iterations we selected Lanczos eigenvectors of predominantly 1h1p character and use them in the Stieltjes routine. In this way we ensure that no energetically forbidden doubly excited state contributes to the width. In the case of HCN·Mg$_2$ the final states consist of HCN in its ground state and the Mg dimer in a variety of ionized states. The energy of the initial state is sufficient to produce the ground and lower excited states of Mg$_2^+$ but not the doubly ionized Mg$_2^{++}$. To span the corresponding subspace we included all 1h1p configurations with a vacancy either in the $3\sigma_g$ or $3\sigma_u$ MO of isolated Mg$_2$. We also added all 2h2p configurations with two holes in the $3\sigma_g$, $3\sigma_u$ orbital subset. In the this case we took as starting block the 100 configurations which have the largest coupling to the initial state. We noticed that this coupling is generally much larger for the 1h1p than for the 2h2p configurations. We used all energetically permitted Lanczos eigenvectors in the Stieltjes calculation.

The calculations were carried out using the ADC(2)x method because we found the interactions among 2h2p configurations to be important to describe the initial and the final states of the decay. We employed the aug-cc-pVTZ Gaussian basis sets [124] augmented with $1s$, $1p$, $1d$ Rydberg-like Gaussians [125] centered on H, C, and N and the aug-cc-pVTZ Gaussian basis set [124] augmented with $3s$, $6p$, $2d$ even-tempered diffuse Gaussians centered on each Mg. Since by construction the decaying state lies near the lower spectral boundary, it can again be easily computed by the Davidson diagonalization method [126]. The structure of HCN·Mg was taken to be linear as in Ref. [19] and the equilibrium geometry of HCN·Mg$_2$ was taken from Ref. [122]. The interfragment distance R is taken to be the distance between N and Mg in both cluster. In all calculations, at various R values, the HCN geometry has been kept fixed at the equilibrium one of free HCN, while that of Mg$_2$ was fixed at the equilibrium value of the HCN·Mg$_2$ adduct. The computed asymptotic vertical excitation energy of the $5\sigma\pi^*$ initial state of HCN is 8.8 eV in both clusters, which is in good agreement with the literature value of 8.6 eV [130] of the isolated HCN molecule. The energy remained almost constant at all distances R considered. For HCN·Mg the subspace representing the final states of the decay comprises 44 1h1p and 4100 2h2p configurations. The results converged after 40 block Lanczos iterations using all 44 1h1p configurations as the starting block. In the case of HCN·Mg$_2$ the dimension of the Hamiltonian representing the final states of the decay was 28000 where 88 of them were 1h1p configurations. We used the 100 configurations with the largest overlap with the initial state to define the starting block and the width converged after 40 block Lanczos iterations.

The ETI width of the $5\sigma\pi^*$ excitations in HCN·Mg is given in Fig. 4.8. At very large R the width increases as R^{-6} with decreasing R, as one can see by comparing the calculated width with the one predicted by the asymptotic formula in Eq. (4.4). At around 16 Å the width starts to increase faster, indeed between 9 Å and 16 Å it is proportional to R^{-8} indicating the decay of a dipole forbidden state. This is an unexpected result since the initial state is optically allowed. However, the Mg photoionization cross section [131,132] exhibits a Cooper minimum [120] close to the energy of the $5\sigma\pi^*$ excitation. Due to its presence, the R^{-6} term becomes comparable with the R^{-8} term in the asymptotic expansion of Γ, and both terms should be taken into account in calculating the decay width. The asymptotic formula becomes

$$\Gamma = \frac{3}{8\pi}\left(\frac{c}{\omega}\right)^4\frac{\sigma(\omega)}{R^6}\Gamma_{rad} + \frac{567}{20\pi}\left(\frac{c}{\omega}\right)^6\frac{\sigma^Q(\omega)}{R^8}\Gamma_{rad} \qquad (4.4)$$

where ω is the frequency of the virtual photon, $\sigma(\omega)$ is the photoionization cross section of Mg due to dipole transitions, $\sigma^Q(\omega)$ is the photoionization cross section of Mg due to quadrupole transitions, and Γ_{rad} is the radiative width of the $5\sigma\pi^*$ excitation in HCN. Note that the prefactor of the second term in Eq. (4.4) is
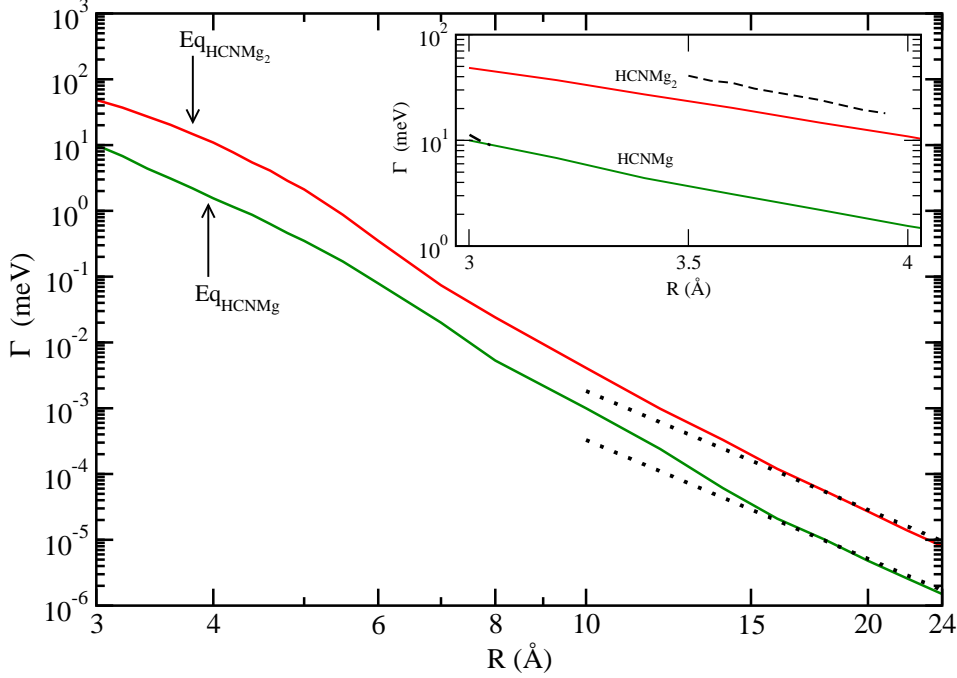
Figure 4.8: The ETI widths of the HCN $5\sigma^{-1}\pi^*$ excitations in HCN·Mg (lower line) and HCN·Mg$_2$ (upper line) clusters as a function of the distance between N and Mg. The results are obtained by using starting blocks of the dimension 44 and 100, respectively, and 40 block Lanczos iterations. The predictions of the first term of Eq. (4.4) are shown as dotted lines. At equilibrium geometries, 3.95 Å and 3.8 Å of HCN·Mg and HCN·Mg$_2$, respectively, the estimated lifetimes are 385 fs and 40 fs, respectively. The inset depicts the comparison between the present results (full lines) and the widths obtained with the CAP-ADC method (dashed lines) where available. The CAP-ADC data is taken from Ref. [19].

different from the prefactor in Eq. (4.3) since the definition of radiative widths and cross sections due to quadrupole transitions differ from the definitions of the same quantities due to dipole transitions. Between 8 and 16 Å the R^{-8} term dominates producing the observed behavior of the width. At interatomic distances larger than 16 Å the R^{-8} contribution becomes so small that the R^{-6} contribution finally governs the behavior of Γ . This is an interesting case where the width of the intermolecular decay is sensitive to the spectroscopic properties of the neighbors. This sensitivity of the intermolecular energy transfer to the properties of the neighbor emphasizes the potential use of ICD as a spectroscopic method as promoted in Ref. [22, 133].

For $5\sigma\pi^*$ excitations in HCN·Mg we obtained a lifetime of about 385 fs at the equilibrium distance (between N and Mg) of 3.9 Å. The obtained width is in

good agreement with the calculations from Ref. [19]. At an N-Mg distance of 3 Å the CAP-ADC method yields a width of 12 meV and the Fano-Stieltjes-Lanczos method predicts here a width of 11 meV (see inset in Fig. 4.8).

The ETI width of the out-of-plane $5\sigma\pi^*$ excitation in HCN·Mg$_2$ is also depicted in Fig. 4.8. At intermolecular distances larger than 20 Å, the width is proportional to R^{-6} and, moreover, is in good agreement with the prediction of the asymptotic formula. Between 9 and 16 Å the width decreases roughly as R^{-7}. We found that the photoionization cross section of Mg$_2$ is roughly one order on magnitude larger than the photoionization cross section of Mg at the same energy of the virtual photon. Consequently, the R^{-6} term in the ETI width of HCN·Mg$_2$ is approximately one order of magnitude larger than the one of HCN·Mg. Thus, both the R^{-8} and R^{-6} terms in equation (4.4) are of comparable size for R between 9 and 16 Å which results in the observed R^{-7} behavior of the width. At the equilibrium geometry we find an ETI lifetime of 40 fs. The ratio of asymptotic ETI widths in HCN·Mg and HCN·Mg$_2$ is approximately six. In the simple case of two independent Mg atoms we would have expected this ratio to be two. Due to the interaction between the Mg atoms the number of channels available for ionization grows non-linearly with the number of atoms which is indicated in the photoionization cross section as well as the ETI width. Our calculations are in good agreement with the results of Ref. [19] as one can see from the inset of Fig. 4.8. At the equilibrium distance the lifetime given by CAP-ADC method is 32 fs.

Possibility of Selfdestructive ETI

When we worked with the P subspace specified above (all 1h1p and 2h2p states with one or two holes in the Mg $3s$ orbital) and all virtual orbitals the calculated widths for $5\sigma\pi^*$ excitations of HCN in HCN·Mg$_n$, $n = 1, 2$ clusters were more than one order of magnitude larger than the ones obtained from CAP-ADC calculations (compare Fig. 4.8, Fig. 4.9, and Ref. [19]). In order to understand the discrepancy, we examined the results of the FSL method carefully and discovered that in the raw spectra, which consist of $\{\Gamma_j, \epsilon_j\}$ pairs, partial widths Γ_j occurred being an order of magnitude larger than all the other partial widths. Those extra-large Γ_j were distributed over the whole spectrum. A analysis of the corresponding eigenstates revealed that all of them correspond to cross excited HCN$^-$·Mg$^+$ states. In those states the electron was not in a continuum orbital. Rather it occupied a virtual valence orbital of HCN. It is clear, that those states are not among the final states of ETI. Consequently, we removed the virtual valence states of HCN from the configuration space P. As a result, the widths decreased to numbers in good agreement with the results from CAP-ADC calculations [25].

The virtual valence states on HCN give rise to electron attachment (EA) and dissociative electron attachment (DEA) shape resonances [134–137]. HCN ex-
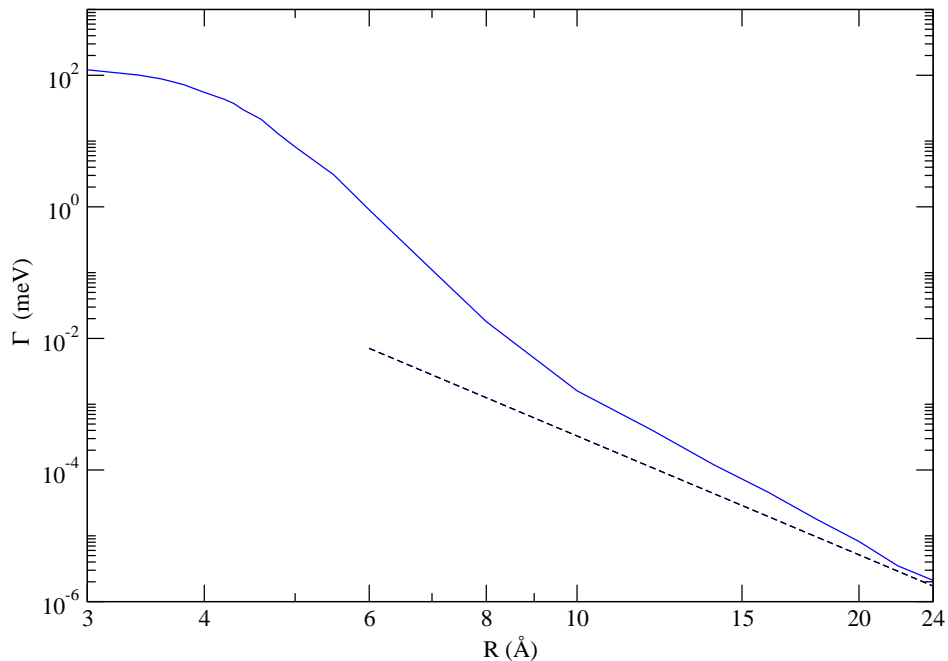
Figure 4.9: Unphysically increased ETI width of HCN $5\sigma^{-1}\pi^*$ excitations in HCN·Mg clusters as a function of the distance between N and Mg. The results have been obtained using the same parameters as in the calculations of the HCN·Mg widths shown in Fig. 4.8. At equilibrium geometries 3.95 Å the estimated lifetimes is 11 fs.

hibits a π^*-resonance, which appears as a structureless ca 1.4 eV broad peak at ca 2.3 eV [134, 135] in the spectrum, and a σ^*-resonance at 6.7 eV [138]. It is important to note that the EA resonances have the same final states as the discussed ETI process. In HCN·Mg the PECs of the HCN*($5\sigma\pi^*$)·Mg and the HCN$^-$·Mg$^+$ state cross in the diabatic picture. Since Mg is only weakly bound to HCN, the electronic coupling between the two state is insignificant. However, in a vicinity of the crossing the states are coupled by bound-continuum-bound interactions [139], see Sec. 5 as well. Since the widths of EA resonances are usually large, this coupling can be significant. Id est, in HCN·Mg the population of the non-dissociative $5\sigma\pi^*$ state of HCN could finally lead to a dissociation of HCN

$$HCN \cdot Mg + N\gamma \rightarrow (HCN)^* \cdot Mg$$
$$\rightarrow (HCN)^{(*,-)} \cdot Mg^+ \rightarrow H + CN^- \cdot Mg^+.$$
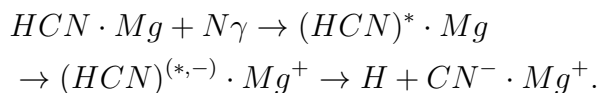
Whether the process can indeed take place has to be investigated. That is not straightforward because the virtual orbitals of HCN are stabilized due to the pres-

ence of Mg^+. Thus, the virtual valence π^* orbital does not give rise to a shape resonance any longer. Even if it still would be a resonance, the states would cross at large internuclear HCN↔Mg distances, far away from the Franck-Condon region, where the nuclear wave packet would properly not appear because it would have been undergone ETI before. On the other hand, the stabilization effect induced by Mg^+ could cast higher lying virtual valence orbitals into EA resonances. The resulting $HCN^*(5\sigma\pi^*)\cdot Mg$ cross excited states would be energetically higher and, as a consequence, the crossing of them and the the the $HCN^*(5\sigma\pi^*)\cdot Mg$ states would be in or close to the Franck-Condon region. *Ab initio* calculations revealed that there are suitbale virtual valence orbitals of HCN. Whether they become the desired EA resonances in the neighborhood of Mg^+ has to be investigated.

Quenching of Photoinduced Reactions by ICD

5.1 Introduction

Excited poly-atomic systems relax by processes involving nuclear rearrangements like photodissociation, isomerization, vibronic coupling, etc [26–28]. If the systems are embedded in an environment the relaxation processes are affected due to interactions with the environment. In liquids, matrices, clusters, and high-pressure gases recombination after photoinduced dissociation due to the *cage effect* [140–143] or relaxation due to vibronic coupling to the environment are just two examples. A special consequence of the presence of environments is ICD [3]. It takes place if the ionization potential of the environment is lower than the excitation energy of the system. During the process the excess energy is transferred to the environment which, as a result, is ionized. The impact of ICD on relaxation processes involving nuclear rearrangements has not been investigated yet, although it is of fundamental interest since the impact is supposed to be significant because of the efficiency of the ICD. The mechanism we investigate here is general, however, for the sake of clearness we illustrate it by considering a diatomic system AB. In electronically excited states $(AB)^*$ the nuclei A and B rearrange. For example, if the excited state is a dissociative one the system will break apart

$$(AB)^* \rightarrow A + B. \tag{5.1}$$

In the presence of a weakly bonded environment Ω the dissociation will usually take place too. Moreover, if the ionization potential of the environment is lower than the excitation energy of the system, the ICD channel opens

$$(AB)^* \cdots \Omega \rightarrow AB \cdots \Omega^+ + e^-. \tag{5.2}$$

Consequently, in the presence of such an environment, the evolution of the system is governed by the competition between dissociation and ICD. In order to be able to predict the evolution the system the competition must be studied quantitatively. In particular, the competition between ICD and photoinduced dissociation is studied in this work. As a concrete example, we consider the dynamics in the four lowest vibrational levels of the $B^1\Sigma^+$ Rydberg state of CO in the presence of Mg.

Photodissociation

The fragmentation of a molecule following the absorption of one or more photons is called photodissociation[1] [26]. The fragmentation can be described as happening in three steps:

$$AB + N\gamma \longrightarrow (AB)^* \longrightarrow A^* + B^*. \tag{5.3}$$

where AB denotes the molecule in a bound state which absorbs N photons γ. The received energy is transferred into internal energy forming the excited intermediate complex $(AB)^*$. The intermediate complex disintegrates into internally excited fragments A^* and B^*. Depending on the shape of the PEC of the intermediate state $(AB)^*$ and on interactions with other states, three major types of photodissociation are distinguished: direct photodissociation, electronic predissociation, and vibrational predissociation [26, 144]. In the first case, the PEC of the intermediate state is purely repulsive and there are no relevant interactions with other states. Hence, the molecule starts to disintegrate immediately and the lifetime of the intermediate complex is usually extremely short. Electronic predissociation takes place if the intermediate state $(AB)^*$ is a bound electronic state which undergoes a radiationless transition to repulsive states. Finally, if the PEC of the intermediate state is dissociative but exhibits a potential well in the vicinity of the equilibrium geometry the nuclear wave function becomes temporarily trapped. This process is summarized by the term vibrational predissociation. Note that while direct dissociation can only occur in the continuous part of the spectrum, discrete states can undergo predissociation. The finite lifetime due to predissociation, then, induces an additional width to the corresponding line in the absorption spectrum.

The efficiency of the photodissociation is given by the photodissociation cross section $\sigma(\omega)$. The photodissociation cross section $\sigma(\omega)$ is closely related to the total photoabsorption cross section $\sigma_T(\omega)$ defined according to Beer's law [26]

$$I(z) = I_0 e^{-z\sigma_T(\omega)\rho}, \tag{5.4}$$

which gives the light intensity after traversiting a column of gas of height z, as a function of the particle density ρ, photon frequency ω, and initial intensity I_0. The photodissociation cross section $\sigma(\omega)$ can be understood as the ability of a system to absorb light of a certain energy which leads to a subsequent dissociation. In systems where the only process competing with photodissociation is photon emission $\sigma \approx \sigma_T$, due to the difference in the timescales of these processes. Using time-dependent perturbation theory in conjunction with the dipole approximation [26, 115], the photodissociation cross section can be expressed by

$$\sigma(\omega) \propto \omega \left| \langle \Psi_f(\omega) | \mathbf{d} | \Psi_i \rangle \right|^2, \tag{5.5}$$

---

[1]Photodissociation means that the molecule dissociates into fragments before it can decay to the electronic ground state, i.e., by photon emission.

where **d** denotes the total dipole operator which is defined as

$$
\begin{aligned}
\mathbf{d} &= -e\sum_{i=1}^{N}\mathbf{r}_i + e\sum_{I=1}^{M}Z_I\mathbf{R}_I \\
&= \mathbf{d}_e + \mathbf{d}_I
\end{aligned}
\tag{5.6}
$$

where $\mathbf{r}_i$ and $\mathbf{R}_I$ denote the position vector of the ith electron and Ith nucleus, respectively. $\mathbf{d}_e$ and $\mathbf{d}_I$ are the contributions of the electrons and the nuclei to the dipole moment. The cross section (5.5) is proportional to the square of the dipole transition matrix element between the initial state $|\Psi_i\rangle$ and the dissociative final state $|\Psi_f(\omega)\rangle$. These states describe the total state of the system, i.e., they describe all electrons and nuclei. Usually, electrons move much faster than nuclei and, hence, it is convenient to decouple the motions because then the electronic and the nuclear problems can be solved separately.

Born-Oppenheimer Approximation

Nuclei are much heavier than electrons and, thus, move slower than the latter. Consequently, the usual way to construct a molecular wave function is to assume that the kinetic energy of the nuclei is small and treat the nuclear motion as a perturbation

$$
\hat{H} = \hat{H}_0 + \hat{H}' = (\hat{T}_e + \hat{V}) + \hat{T}_n
\tag{5.7}
$$

where $\hat{H}_0$ is the electronic part of the Hamiltonian (2.28) and $\hat{H}'$ contains the kinetic energy operator of the nuclei $\hat{T}_n$. If the electronic eigenproblem is solved

$$
\hat{H}_0\phi_n(\mathbf{r},\mathbf{R}) = E_n(\mathbf{R})\phi_n(\mathbf{r},\mathbf{R}),
\tag{5.8}
$$

where the electronic eigenfunctions $\phi_n(\mathbf{R},\mathbf{r})$ and eigenenergies $E_n(\mathbf{R})$ depend only parametrically on $\mathbf{R}$, the molecular wavefunction $\Psi(\mathbf{R},\mathbf{r})$ can be expanded in terms of $\phi_n(\mathbf{R},\mathbf{r})$

$$
\Psi(\mathbf{R},\mathbf{r}) = \sum_n \phi_n(\mathbf{r},\mathbf{R})\chi_n(\mathbf{R}).
\tag{5.9}
$$

The expansion coefficients are the nuclear wave function $\chi_n(\mathbf{R})$. Using (5.9) and (5.7) in the Schrödinger equation, multiplying by $\phi_m^*(\mathbf{R},\mathbf{r})$, and integrating over the electronic coordinates yields

$$
(E_n(\mathbf{R}) - E)\chi_m(\mathbf{R}) + \int\left[\phi_m^*(\mathbf{R},\mathbf{r})\hat{H}'\sum_n\chi_n(\mathbf{R})\phi_n(\mathbf{R},\mathbf{r})\right]d\mathbf{r} = 0.
\tag{5.10}
$$

By defining the coupling coefficients [119]

$$c_{mn} = \int \phi_m^* \hat{H}' \phi_n d\mathbf{r} - \frac{\hbar}{2} \left[\int \phi_m^* \sum_k \frac{1}{M_k} \frac{\partial}{\partial R_k} \phi_n d\mathbf{r} \right] \frac{\partial}{\partial R_k}, \qquad (5.11)$$

(5.10) can be written as

$$(E_n(\mathbf{R}) - \hat{H}')\chi_m(\mathbf{R}) + \sum_n c_{mn}\chi_n(\mathbf{R}) = E\chi_m(\mathbf{R}). \qquad (5.12)$$

The equations (5.8) and (5.12) form a system of coupled equations which is equivalent to the Schrödinger equation. The coupling is given by the matrix $\underline{\mathbf{c}}$, whose elements describe how the different electronic states are coupled by nuclear motion. Different choices of the elements c_{mn} lead to different physical pictures: $c_{mn} = 0$ decouples the motion of nuclei in different electronic states. This approximation is called adiabatic approximation or Born-Oppenheimer approximation (BOA) if the diagonal elements c_{nn} are neglected as well. These approximations lead to the basic concept for molecules, liquids and solids in which electronic potential surfaces are introduced and nuclear wave packets move on them.

The BOA fails if two or more electronic states $|\phi_i\rangle$ lie close in energy. This is the situation encountered in the Jahn-Teller effect [145], Renner-Teller effect [146], or avoided crossings [147]. Vibrational predissociation is caused by avoided crossings of two or more electronic states. In order to describe such situations, it is often reasonable to introduce a representation of the electronic states which minimizes the couplings via nuclear motion [148–150]. Such representations are called diabatic ones.

Diabatic Picture

In order to derive a transformation that links the adiabatic electronic eigenstates (5.8) to diabatic ones, it is helpful to recognize that usually not all electronic eigenstates (5.8) are energetically close. Rather a few states are coupled by nuclear motion and can be regarded as decoupled from all the other states. As a consequence, it is convenient to look for a unitary transformation $\underline{\mathbf{A}}^{\alpha \times \alpha}$ that minimizes the couplings (5.11) within a subset of states α

$$|\phi_i^D\rangle = \sum_j A_{ij}^{\alpha \times \alpha} |\phi_j^{AD}\rangle, \quad i, j = 1, \ldots, \alpha, \qquad (5.13)$$

where the superscripts D and AD indicate that the marked state belongs to the diabatic or adiabatic representation, respectively. In the diabatic basis the couplings

$$\underline{\mathbf{F}}^{(k)} = \langle \phi_i^{AD} | \frac{\partial}{\partial \mathbf{R}_k} | \phi_j^{AD} \rangle \qquad (5.14)$$

are to be minimized, which allows one to write down a differential equation for the transformation matrix [151, 152]

$$\underline{\mathbf{F}}^{(k)}\underline{\mathbf{A}}^{\alpha\times\alpha} + \frac{\partial}{\partial\mathbf{R}_k}\underline{\mathbf{A}}^{\alpha\times\alpha} = 0. \tag{5.15}$$

To solve the equation (5.15) the $\underline{\mathbf{F}}^{(k)}$ must be known. There are numerical approaches to determine the so-called derivative couplings [152, 153], but calculating them is a cumbersome task. Moreover, it can be shown that there is no general solution for (5.15) except for diatomic molecules [151], i.e., there is no real diabatic basis in general and, thus, the non-adiabatic couplings cannot be removed completely [151, 154]. On the other hand, there are methods to derive diabatic bases which do not rely on the calculation of the derivative couplings. Thus, Werner and Meyer diagonalize the dipole operator [155], while Hendeković proposed a method where the sum of the occupation probabilities of natural spin orbitals is maximized [156]. In the present work, we use an approach which was triggered by a work of Özkan *et al* [157]. In its framework, the electronic Hamiltonian is block diagonalized [158]. A description of the approach can be found in App. A.

5.2 Photodissociation of Carbon Monoxide

Carbon monoxide (CO) is one of the most abundant molecules in the universe; it plays a major role in interstellar clouds and, thus, its dynamics in the ultra violet (UV) region are of general interest. In the UV region CO undergoes predissociation and, consequently, discrete broadened lines are observed in its UV absorption spectrum [159] which is mainly consisting of Rydberg states. A large amount of experimental data for these states is available [30–32, 159]. The goal of the present work is to study how the nuclear dynamics of the Rydberg $B^1\Sigma^+$ state of CO molecule change if it is placed in an environment. Before we can consider the influence of the environment we review what is known about the dynamics in that state of isolated CO.

Letzelter *et al* measured the photoabsorption and photodissociation cross section of several CO isotopes between 10.7 eV and 14.0 eV with synchrotron radiation [159]. They found the $X^1\Sigma^+(\nu = 0) \rightarrow B^1\Sigma^+(\nu = 0)$ excitation at 10.767 eV. The $B^1\Sigma^+(\nu = 1)$ and $B^1\Sigma^+(\nu = 2)$ states were detected at 11.034 eV and 11.282 eV, respectively. Eidelsberg *et al* investigated both the absorption and emission band spectrum of $X^1\Sigma^+(\nu = 0, 1, 2, 3) \rightarrow B^1\Sigma^+(\nu = 0, 1, 2)$ excitations and determined vibrational and rotational molecular constants of the $B^1\Sigma^+$ Rydberg state for several isotopes of CO [30, 31]. Baker *et al* were the first observing the $\nu = 3$ level of the $B^1\Sigma^+$ state [32]. They could assign the diffuse band at 11.507 eV to the $X^1\Sigma^+(\nu = 0) \rightarrow B^1\Sigma^+(\nu = 3)$ transition by comparing the experimental spectrum to a calculated spectrum using the diabatic two-state model given in Ref. [29]; see below for a discussion. The agreement of the calculated and the

measured spectra was very good. Recently, Baker could identify the diffuse $\nu = 4$ and $\nu = 5$ vibrational level of the $B^1\Sigma^+$ Rydberg state [160]. Theoretical calculations predict even higher vibrational levels in this electronic state [161,162].
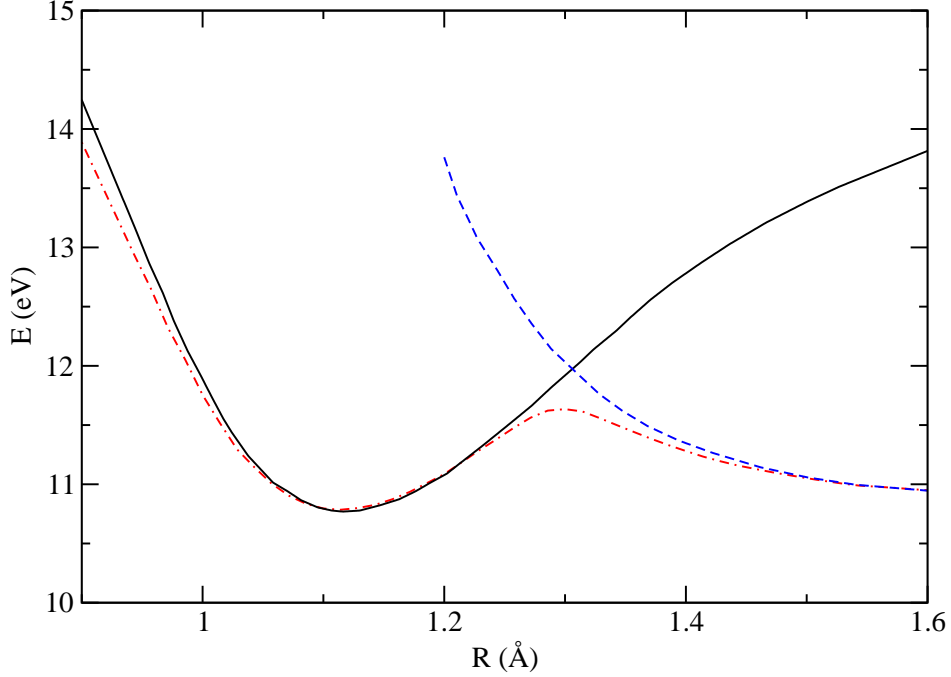
Figure 5.1: Diabatic PECs of the $B^1\Sigma^+$ and the $D^1\Sigma^+$ state of CO obtained by means of the Rydberg-Klein-Rees method [29]. The depicted adiabatic PEC is calculated from the diabatic PECs.

In all cited works it was found that the first two vibrational levels of the $B^1\Sigma^+$ Rydberg state exhibit fluorescence. In contrast, the third vibrational level $\nu = 2$ does not appear in the fluorescence spectrum. However, it is observable in the photoabsorption spectrum where the corresponding line is broadened. Similarly, the higher lying vibrational levels $\nu = 3, 4, 5$ occur in the absorption spectrum only and exhibit strongly broadened lines. These observations suggest that CO undergoes predissociation in the higher vibrational levels of the $B^1\Sigma^+$ state. In order to understand the underlying mechanism theoretical investigation is required.

The first theoretical study providing insight into the complicated electronic excitation spectrum of CO was done by Cooper and Kirby [163] who calculated the PECs and dipole moments of low lying $^1\Sigma$ and $^1\Pi$ states of CO employing

multiconfiguration SCF. They deduced from the W-shape of the PEC that the $B^1\Sigma^+$ Rydberg state is strongly interacting with the $D'^1\Sigma^+$ valence state at internuclear distances larger than the equilibrium displacement. The nuclear dynamics

ν	$\Gamma[\text{meV}]^a$	$\Gamma[\text{meV}]^b$	$\Gamma[\text{meV}]^c$	$\Gamma[\text{meV}]^d$	$\Gamma[\text{meV}]^e$	$\Gamma[\text{meV}]^f$
0	0.000	0.000	0.000	0.000	0.000	0.000
1	0.000	0.000	0.000	0.000	0.000	0.000
2	0.111	0.111	0.111	0.111	0.110	0.012
3	11.266	11.271	11.270	11.271	-	2.852
4	99.361	99.423	99.415	99.414	-	-
5	229.89	229.89	229.88	229.93	-	-

[a] from Ref. [164]
[b] from Ref. [161]
[c] from Ref. [165]
[d] from Ref. [162]
[e] from Ref. [29]
[f] from Ref. [166]

Table 1: Calculated predissociation widths of the first five vibrational levels of the CO $B^1\Sigma^+$ state.

in the Rydberg state were carried out by Tchang-Brillet *et al* who derived a diabatic two-state model including the $B^1\Sigma^+$, the valence $D'^1\Sigma^+(\pi\pi^*)$ state and the electronic coupling between them [29]. The two diabatic PECs were obtained by means of the Rydberg-Klein-Rees (RKR) method [119] where the required molecular constants were taken from [30, 31]. With the aid of this model they computed the nuclear dynamics in the three lowest vibrational levels of the $B^1\Sigma^+$ state using the close-coupling method [29]. For the sake of comparison they derived the corresponding adiabatic curves from the diabatic model and calculated the corresponding adiabatic widths. They found that the first two vibrational levels are stable with respect to dissociation and that the third vibrational level undergoes predissociation. The computed predissociation widths were 0.11 meV and 0.22 meV using the diabatic or adiabatic model, respectively. Later on, the same model predicted the position and the shape of the photoabsorption line corresponding to the next vibrational level $\nu = 3$ of the $B^1\Sigma^+$ state in agreement with experimental results [160]. The good agreement of the results with the experimental observations suggested that the coupling between the Rydberg and the valence state is indeed the reason for the observed predissociation.

This assumption is additionally supported by a number of theoretical works. Yan Li *et al* calculated the predissociation widths of the first eleven vibrational levels of the $B^1\Sigma^+$ state with the aid of a diabatic two-state model from [161]. To obtain the widths they expanded the nuclear wave functions in the basis of complex harmonic oscillator functions which is equivalent to complex scaling according to the Cauchy-Coursat theorem for integration of an analytical function [167]. The resulting complex potential energy matrix is evaluated numerically by

Gauss-Hermite quadrature. The resulting widths were in good agreement with the one from [29]. In their second paper on the CO dynamics Yan Li *et al* determined predissociation widths of the $B^1\Sigma^+$ and $C^1\Sigma^+$ Rydberg state using adiabatic PECs obtained by multireference CI calculations [166]. To account for the coupling between the states they calculated the non-adiabatic couplings c_{nm} and the nuclear kinetic energy corrections c_{nn}. The widths were obtained with the same method as in the work above [161]. The widths are in good agreement with the previous calculated ones and can be found in Tab. 1.

Monnerville and Robbe calculated predissociation widths of the $B^1\Sigma^+$ state for the first eleven vibrational levels and for the third level $\nu = 2$ the widths for the rotational levels $J = 0, \ldots, 15$ using a two-state model [162]. To describe the resonant states they added a CAP to the Hermitian Hamiltonian. The employed diabatic PECs were taken from [29]. Four years later Monnerville and Robbe applied the above described method using an adiabatic two-state model [165]. The adiabatic PECs and non-adiabatic couplings were calculated from the diabatic model used in the previous work. The results of both works are in good agreement with the preceding theoretical and experimental investigations (see Tab. 1).

Karlsson calculated the first eleven vibrational levels of the $B^1\Sigma^+$ state in the diabatic and the adiabatic picture using smooth exterior scaling [168, 169] in conjunction with the discrete variable representation (DVR) [164]. The resulting widths - which are also displayed in Tab. 1 - are in good agreement to calculated widths from Ref. [161] and Ref. [165].

ν^a	Energy[eV]	Γ_{exp}[meV]	Γ_{calc}[meV]^b	Γ_{calc2}[meV]^c	[I(0-ν)/I(0-0)]
0	10.776	0.00003	0.00	0.00	1.00
1	11.034	0.00003	0.00	0.00	0.15
2	11.281	0.086-0.248	0.11	0.012	0.008
3	11.505	11.10	11.00	2.80	0.0011
4	11.741	43	99	-	0.0005
5	12.033	55	223	-	0.0008

[a]Exp. data: $\nu = 0 - 2$ from Ref. [29–31]; $\nu = 3$ from Ref. [32]; $\nu = 4, 5$ from Ref. [160]
[b]from Ref. [164]
[c]comes from Ref. [161]

Table 2: Energies and experimental and theoretical predissociation widths of the six lowest vibrational levels of the $B^1\Sigma^+$ state of CO. The experimentally obtained Franck-Condon factors ([I(0-ν)/I(0-0)]) a given as well.

Adiabatic Picture

Before we can study the influence of an environment on the photodissociation dynamics of CO it is necessary to check whether one is able to reproduce the

dynamics taking place in isolated CO. As mentioned above, accurate electronic states have been calculated *ab initia*lly by means of multireference CI [163, 166], or using experimentally obtained parameters and the RKR method [29]. Our goal was to conduct a fully *ab initio* study of the dynamics. Since our FSL program produces ICD widths based on ADC calculations, we tried to obtain accurate PECs using the ADC method in order to obtain a consistent description.

We calculated the PECs of the ground and the first six excited states of the Σ^+ symmetry of isolated CO at inter-nuclear distances between 0.9 and 1.4 Å. At the equilibrium geometry (1.128 Å) we could identify the first five Rydberg states: $B^1\Sigma^+(3s\sigma)$, $C^1\Sigma^+(3p\sigma)$, $F^1\Sigma^+(3d\sigma)$, $J^1\Sigma^+(4s\sigma)$, and $4p\sigma^1\Sigma^+$. The calculations were carried out using the ADC(2)x scheme and aug-cc-pVTZ basis sets [124] augmented with 3s, 3p, and 3d Rydberg-like Gaussian functions [125] centered on C and O. The configuration space used to construct the ADC Hamiltonian consisted of all 1h1p configurations with one hole in 3σ, 4σ, 5σ, and 1π. To account for electron correlation we included all 2h2p configurations one can construct from the holes located in the 3σ, 4σ, 5σ, and 1π MOs. The dimension of the resulting ADC matrix was around 60000. Since the desired states lie by definition at the lower boundary of the spectrum we employed the Davidson method [126] to calculate them. In Tab. 3 the calculated energies are compared to

State	Calc. Energy [eV]	Exp. Energy [eV][a]
$B(3s\sigma)^1\Sigma^+$	10.49	10.76
$C(3p\sigma)^1\Sigma^+$	11.25	11.39
$F(3d\sigma)^1\Sigma^+$	12.20	12.30
$J(4s\sigma)^1\Sigma^+$	12.33	12.56
$4p\sigma^1\Sigma^+$	12.63	12.77

[a]taken from Ref. [159]

Table 3: Comparison between experimentally measured and calculated electronic energies of the first five Rydberg states of CO at the equilibrium geometry (1.128 Å). The calculated values were obtained with the aid of the ADC(2)x method.

experimental ones. As one can see, the calculated energies are in good agreement with the measured ones. Additionally, the results are in good agreement with the results from Trofimov's PhD thesis [170] where the first four Rydberg state were calculated at inter-nuclear distances between 0.85 and 1.25 Å utilizing the same method in conjunction with different basis sets. The PECs resulting from our ADC(2)x calculations are depicted in Fig. 5.2. At inter-nuclear distances larger than 1.15 Å one can observe the effect of the $D'(\pi\pi^*)^1\Sigma^+$ valence state which "crosses" through the Rydberg series and deforms the PECs. The induced perturbation is strong and complicated since the crossing $D'^1\Sigma^+$ state interacts with all Rydberg states non-adiabatically [29, 30, 163]. The first adiabatic excited state is affected the most. At smaller inter-nuclear distances it is of the $B^1\Sigma^+$
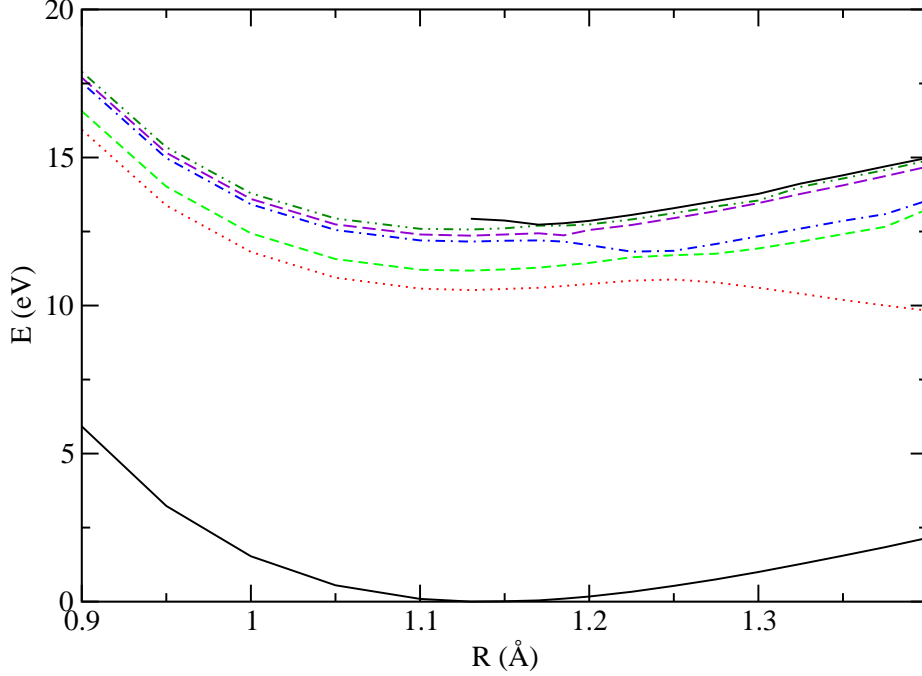
Figure 5.2: PECs of the ground state and the six energetically lowest adiabatic excited states of CO of Σ^+ symmetry obtained by means of the ADC(2)x method. At inter-nuclear distances larger than 1.17 Å the $D'(\pi\pi^*)^1\Sigma^+$ state crosses through the Rydberg series.

Rydberg character; at inter-nuclear larger than 1.2 Å it has lost its Rydberg character completely and becomes the long range manifestation of the $D'^1\Sigma^+$ valence state.

The perturbation induced by the $D'^1\Sigma^+$ state leads to the observed predissociation [29,161] in the higher vibrational levels of the $B^1\Sigma^+$ state. In particular, the perturbation becomes manifest in the location, the shape, and the height of the potential barrier at 1.24 Å (see Fig. 5.2). The comparison of the well resulting from our calculation with the well resulting from RKR calculations [29] reveals large differences: our well is lying at larger inter-nuclear distances and is lower as shown in Fig. 5.3. That the *ab initio* results increasingly differ from the RKR model as the inter-nuclear distance grows can be explained by the fact that the systems becomes open shell. The employed method is only adapted for closed shell determinants [87].

Since the predissociation widths are very sensitive to the height and the location of the barrier, we cannot use the calculated PECs to carry out our study, because this would lead to dissociation widths much larger than the experimentally ob-
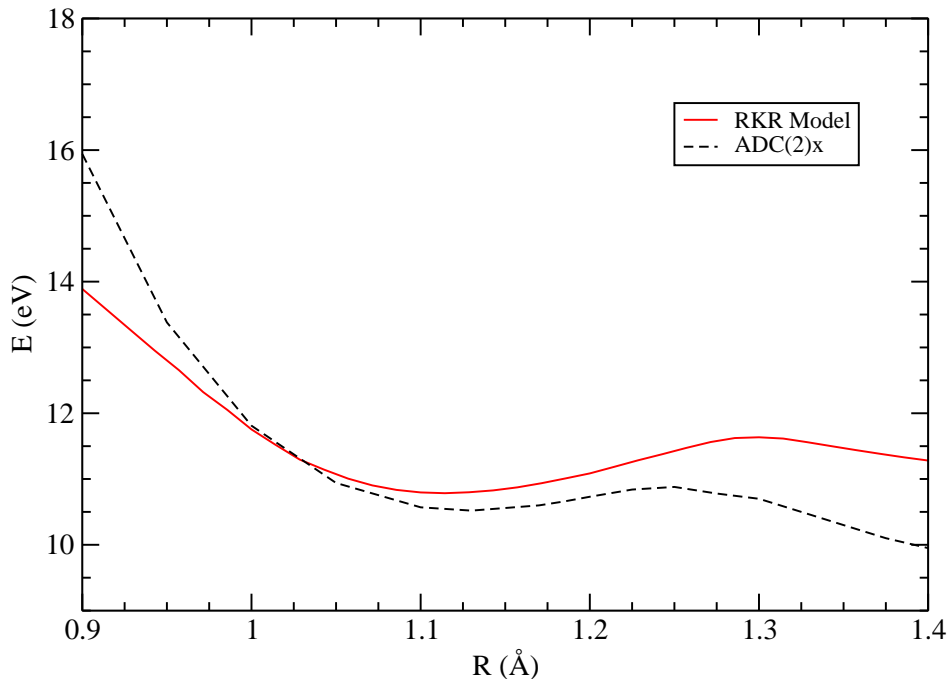
Figure 5.3: Comparison between the adiabatic CO $B^1\Sigma^+$ state of the RKR model and the CO $B^1\Sigma^+$ state obtained via ADC(2)x calculations.

served ones. Since we cannot obtain the required PECs sufficiently accurate by means of ADC, we decided to use the two state model from [29] which is based on PECs obtained by means of the RKR method. This model will be referred to as *the RKR model* in the following. The model has been proven to produce nuclear dynamics in good agreement with experimental results [29,161,162]. Corresponding models for CO embedded in an environment do not exist. However, we can still use the RKR model if we can show that the PECs of interest are affect only insignificantly by the presence of the environment. To this end, the PECs of interest of CO·Mg are calculated by means of the ADC(2)x method and then compared to the PECs of isolated CO given in Fig. 5.2. Before it, however, we determine the non-adiabatic coupling between the $B^1\Sigma^+$ and the $D'^1\Sigma^+$ state in isolated CO. The coupling between the states can be compared to corresponding coupling in CO·Mg. Thus, we can check precisely whether the interaction between the states, which is relevant for the predissociation, is affected by the presence of Mg. Moreover, comparing the coupling obtained by means of the ADC method to the couplings of the RKR model enables one to understand better where the deviations come from and, if strong deviations are found, whether

it is necessary to correct the widths which is designated to be used in conjunction with the RKR model although it is based on ADC calculations.

Diabatic Picture

The non-adiabatic coupling between the $B^1\Sigma^+$ and the $D'^1\Sigma^+$ state can be determined conveniently in the diabatic picture where it occurs as electronic coupling. The diabatic states can be calculated with the aid of the block diagonalization method [158]. In its framework a diabatic basis is derived by block diagonalizing the adiabatic Hamiltonian matrix $\underline{\mathbf{H}}$ using the unitary matrix $\underline{\mathbf{F}}$

$$\underline{\mathcal{H}} = \underline{\mathbf{F}}^\dagger \underline{\mathbf{H}} \underline{\mathbf{F}}, \tag{5.16}$$

where

$$\underline{\mathbf{F}} = \underline{\mathbf{S}}_{BD}^\dagger (\underline{\mathbf{S}}_{BD} \underline{\mathbf{S}}_{BD}^\dagger)^{1/2}. \tag{5.17}$$

The underlying assumption is that diabatic states correspond mainly to one main space configuration. Thus, $\underline{\mathbf{S}}_{BD}$ is constructed of the leading configurations of the adiabatic eigenstates of interest and their contribution to the other adiabatic eigenstates of interest. Naturally, the choice of $\underline{\mathbf{S}}_{BD}$ is not unique. Exemplarily,

State	Energy [eV]	Tran	1st	2nd	3rd
2	10.34960	0.99871	-.3659(23)	-.3067(26)	-.3067(25)
3	11.16815	-1.00164	-.3660(11)	-.3623(23)	0.3214(26)
4	11.31832	-0.73511	0.5073(33)	-.4141(21)	-.3896(17)
5	12.41556	0.24291	0.4574(17)	0.3841(27)	-.3780(21)
7	12.59418	0.02655	-.6705(1)	0.3546(23)	-.2800(17)
8	12.75482	0.38164	-.6828(5)	-.3313(33)	-.2344(17)

Table 4: The 1h1p configurations which contribute the most to the first six states of CO in Σ^+ symmetry at an inter-nuclear distance of 1.225 Å. The number in parentheses denotes the number of the configuration in the calculation.

we show how the transformation is obtained at an inter-nuclear distance of 1.225 Å between C and O, where the two states of interest are about to cross (see Fig. 5.2). Although the choice of the configurations constituting $\underline{\mathbf{S}}_{BD}$ is ambiguous, analyzing the most contributing configurations of the states of interest (see Tab. 4) usually allows to make a reasonable selection.

Here we chose the following configurations:

$$(25)[\pi^{-1}\pi] \quad (11)[5\sigma^{-1}3s] \quad (33)[5\sigma^{-1}3p_z]$$
$$(17)[5\sigma^{-1}4s] \quad (1)[5\sigma^{-1}4p_z] \quad (5)[5\sigma^{-1}s](5).$$

The order is *not* arbitrary. It means, e.g., that configuration 25 represents state 2 of Tab. 4, configuration 11 state 3, etc. The kind of excitation the current configuration is associated with is stated in the square brackets. We decided to incorporate the first six adiabatic states into the transformation because the $D'^1\Sigma^+$ state crosses through all of them. By decoupling all six states we are able to track the $D'^1\Sigma^+$ state better. Having the configurations and their corresponding coefficients at hand, the block diagonalization procedure for the chosen subspace can be carried out. In this case the matrix reads (in a.u.):

$$\underline{\mathbf{S}}_{BD} = \begin{pmatrix} -0.307 & 0.321 & -0.003 & -0.042 & -0.066 & 0.002 \\ -0.278 & -0.366 & -0.123 & -0.280 & -0.010 & -0.226 \\ 0.028 & 0.034 & 0.507 & -0.080 & 0.085 & -0.331 \\ -0.013 & -0.011 & -0.390 & 0.457 & -0.280 & -0.234 \\ -0.196 & -0.290 & 0.142 & -0.243 & -0.671 & 0.193 \\ -0.050 & -0.082 & -0.184 & -0.118 & -0.155 & -0.683 \end{pmatrix}$$

Each row corresponds to a configuration and each column to state. For example, the first row represents the contribution of configuration 25 to all the eigenvectors and, on the other hand, the first column corresponds to state 2. Note that the smaller off-diagonal elements cannot be read from Tab. 4. The choice of $\underline{\mathbf{S}}_{BD}$ leads to the following transition matrix (in a.u.):

$$\underline{\mathbf{F}} = \begin{pmatrix} -0.718 & -0.645 & -0.074 & -0.157 & -0.124 & 0.206 \\ 0.686 & -0.655 & -0.034 & -0.117 & -0.267 & 0.125 \\ -0.014 & -0.157 & 0.865 & -0.292 & 0.223 & -0.303 \\ -0.080 & -0.216 & 0.172 & 0.840 & -0.249 & -0.387 \\ -0.091 & 0.264 & 0.070 & -0.328 & -0.864 & -0.252 \\ -0.005 & -0.185 & -0.459 & -0.251 & 0.235 & -0.798 \end{pmatrix}.$$

Using the known diagonal matrix of adiabatic eigenvalues (in eV)

$$\underline{\mathbf{\Lambda}} = \begin{pmatrix} 10.349 & 0.000 & 0.000 & 0.000 & 0.000 & 0.000 \\ 0.000 & 11.168 & 0.000 & 0.000 & 0.000 & 0.000 \\ 0.000 & 0.000 & 11.318 & 0.000 & 0.000 & 0.000 \\ 0.000 & 0.000 & 0.000 & 12.415 & 0.000 & 0.000 \\ 0.000 & 0.000 & 0.000 & 0.000 & 12.594 & 0.000 \\ 0.000 & 0.000 & 0.000 & 0.000 & 0.000 & 12.755 \end{pmatrix},$$

the following block diagonal energy matrix of the diabatic picture is obtained (in eV)

$$\underline{\mathbf{\Delta}} = \underline{\mathbf{F}}^\dagger \underline{\mathbf{\Lambda}} \, \underline{\mathbf{F}} = \begin{pmatrix} 10.766 & -0.381 & -0.068 & -0.131 & 0.061 & 0.199 \\ -0.381 & 11.059 & 0.056 & -0.350 & -0.397 & 0.356 \\ -0.068 & 0.056 & 11.654 & 0.283 & -0.290 & 0.446 \\ -0.131 & -0.350 & 0.283 & 12.294 & 0.023 & 0.071 \\ 0.061 & -0.397 & -0.290 & 0.023 & 12.392 & 0.144 \\ 0.199 & 0.356 & 0.446 & 0.071 & 0.144 & 12.434 \end{pmatrix}.$$

Note that we only consider one block, thus, the block diagonal structure, which
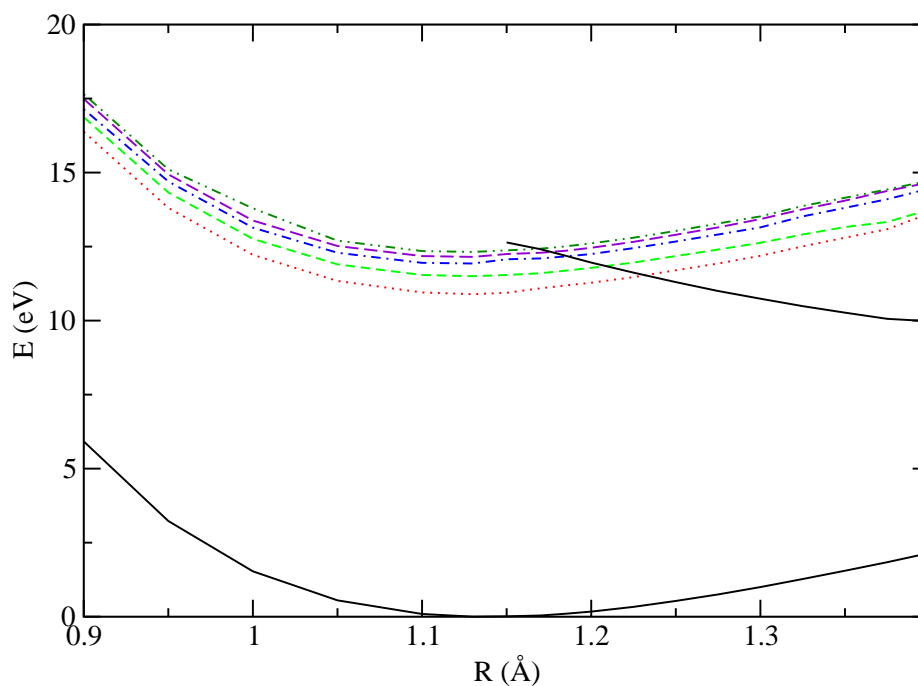
Figure 5.4: The ground state and the six energetically lowest excited states of CO of Σ^+ symmetry given in the diabatic basis obtained by means of the block diagonalization method.

the complete Hamiltonian matrix exhibits, is not visible. The couplings corresponding to the PECs of Fig. 5.4 are given farther below in Fig. 5.8. Moreover, they are compared to the couplings in CO·Mg and to the couplings of the RKR model there.

## 5.3 Carbon Monoxide in the Presence of Magnesium
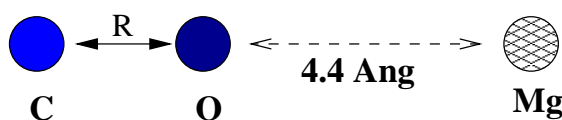
Figure 5.5: Schematic illustration of the geometry of the CO·Mg cluster. In the model employed, the Mg atom is fixed with respect to the center of mass of CO.

In order to get an environment capable of ICD an Mg atom is placed in the vicinity of CO. According to a geometry optimization [171], CO·Mg arranges in a linear manner where the Mg atom is lying 4.8 Å away from the center of mass of CO in front of the O end; a schematic illustration is given in Fig. 5.5. The $CO^*B^1\Sigma^+$ state is 10.77 eV above the ground state and, thus, higher in energy than the ionization potential of Mg which lies at 7.67 eV [123]. As a consequence, the $B^1\Sigma^+$ state can relax via ICD by emitting an electron from the Mg with an kinetic energy of about 3.1 eV. Besides from the fact that Mg allows for ICD, it was chosen as neighbor because, firstly, it is a closed shell system and, secondly, it is only weakly bound to the CO molecule: the corresponding binding energy is 0.01 eV [171] which is less compared to the binding energy of CO 11.2 eV [29, 30, 159]. The first aspect is important since the employed ADC method is based on a closed-shell determinant [67]. The second aspect enables us to fix the Mg atom in good approximation with respect to the center of mass of CO. As a consequence, there is only one nuclear coordinate in the following which specifies the distance between the C and the O atom. Moreover, according to the binding energy, the influence of the presence of Mg on the electronic spectrum of CO is supposed to be weak. That is important because, as mentioned above, we are not able to calculate the corresponding PECs of CO·Mg accurately. However, the PECs of the RKR model can be used if we show that the influence of Mg on the real part of the PECs is minor.

Adiabatic Picture

In order to verify that the impact is minor, we determined the PECs of interest of CO·Mg using the ADC(2)x method. If the corresponding PECs of CO and CO·Mg are alike, the PECs of CO can be used in good approximation to describe the dynamics of CO in CO·Mg. The comparison of the PECs can simply be done by comparing the adiabatic PECs. Additionally, we compare the electronic coupling between the states of isolated CO to the coupling of the corresponding states in CO·Mg in the next subsection.

To determine the PECs of CO·Mg by means of the ADC(2)x method we employed aug-cc-pVTZ basis sets [124] augmented with 3s, 3p, and 3d functions with Rydberg-like Gaussian functions [125] centered on C and O. To represent Mg we chose the aug-cc-pVTZ basis set augmented with 5s, 5p, and 5d Gaussian functions with even tempered exponents [128, 129]. The configuration space consisted of all 1h1p configurations with one hole in 3σ, 4σ, 5σ, and 1π. To account for electron correlation we included all 2h2p configurations containing holes in 3σ, 4σ, 5σ, and 1π MOs. The dimension of the resulting ADC matrix was around 80000. Since by construction the states of interest lie near the lower spectral boundary, we used the Davidson diagonalization method [126] to compute them.

The PECs obtained are depicted in Fig. 5.6. The lowest curve corresponds to the ground state $X^1\Sigma^+$. The first excited state (dotted line) is relevant for the
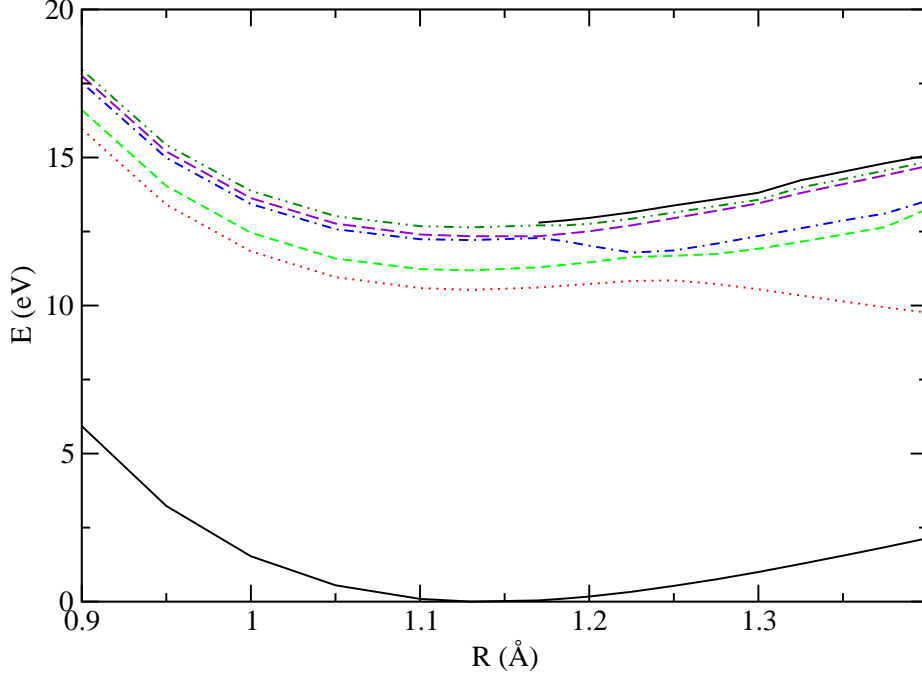
Figure 5.6: PECs of the ground state and the six energetically lowest adiabatic excited states of CO·Mg of Σ^+ symmetry calculated with the ADC(2)x method.

dynamics we are interested in. It corresponds to the diabatic $B^1\Sigma^+$ state at internuclear distances smaller than 1.2 Å. After the well at 1.25 Å, it corresponds to the diabatic $D'^1\Sigma^+$ state. In front of the well, the existence of the diabatic $D'^1\Sigma^+$ state becomes only manifest in the perturbations of the higher Rydberg states. Comparing the PEC of first excited state to the corresponding PECs of isolated CO given in Fig. 5.2 shows that the states are very alike. The effect of the neighboring Mg atom on the excitation spectrum of CO is minor. In particular, at equilibrium geometry we obtained an energy of 10.53 eV for the $B^1\Sigma^+$ state in CO·Mg. The corresponding value in isolated CO is 10.49 eV. Moreover, the location and the height of the well are virtually equivalent in both systems. As a consequence, it is reasonable to use the PECs of the RKR model to carry out the dynamics of CO in CO·Mg.

Diabatic Picture

In order to determine the coupling between the $B^1\Sigma^+$ and the $D'^1\Sigma^+$ states of CO in CO·Mg we transform the corresponding PECs obtained by ADC calculations

into the diabatic picture. There, the coupling is given by the electronic coupling between the states. Again, we discuss the transformation exemplarily at an inter-nuclear distance between C and O of 1.225 Å. As above, the first step is to define

State	Energy [eV]	Tran	1st	2nd	3rd
2	10.31977	1.06252	-.282645(45)	-.250353(65)	-.240752(23)
3	11.14988	0.89336	0.310569(23)	-.289575(17)	0.275551(45)
4	11.33063	-0.88601	-.491936(43)	0.389967(59)	-.341114(29)
5	12.41818	0.01121	-.377465(21)	0.371162(11)	0.368962(39)
7	12.60832	-0.04688	0.538036(7)	0.439188(1)	0.286958(53)
8	12.84897	0.34004	0.481587(11)	-.369331(23)	-.293372(39)

Table 5: The 1h1p configurations contributing the most to the six energetically lowest states of CO·Mg in Σ^+ symmetry at an inter-nuclear distance of 1.225 Å. The number in parentheses denotes the number of the configuration.

$\underline{\mathbf{S}}_{BD}$. The comparison of Tab. 5 and Tab. 4 reveals that the structures of the part of the excitation spectrum of interest are alike. We chose the following configurations

$$(45)[\pi^{-1}\pi] \quad (23)[5\sigma^{-1}3s] \quad (43)[5\sigma^{-1}3p_z]$$
$$(21)[5\sigma^{-1}4s] \quad (7)[5\sigma^{-1}4p_z] \quad (11)[5\sigma^{-1}s]$$

to define $\underline{\mathbf{S}}_{BD}$. The excitation stated in the square brackets behind the number of the configuration indicates the physical meaning of the current configuration. The resulting transformation matrix reads

$$\underline{\mathbf{F}} = \begin{pmatrix} 0.740 & -0.605 & -0.012 & -0.002 & 0.222 & -0.193 \\ 0.659 & 0.641 & -0.045 & -0.077 & -0.370 & 0.099 \\ -0.073 & -0.157 & -0.931 & -0.184 & -0.260 & -0.030 \\ -0.008 & 0.012 & 0.107 & -0.937 & 0.248 & 0.220 \\ 0.101 & 0.273 & -0.329 & 0.261 & 0.751 & 0.417 \\ 0.041 & -0.352 & 0.103 & 0.116 & -0.347 & 0.854 \end{pmatrix}.$$

Using the stated transformation, the following diabatic energy matrix (in eV) was obtained

$$\underline{\mathbf{\Delta}} = \begin{pmatrix} 10.714 & 0.390 & -0.023 & 0.059 & -0.048 & 0.237 \\ 0.390 & 11.170 & -0.170 & 0.025 & 0.629 & -0.438 \\ -0.023 & -0.170 & 11.497 & -0.202 & -0.342 & -0.018 \\ 0.059 & 0.025 & -0.202 & 12.393 & -0.067 & 0.067 \\ -0.048 & 0.629 & -0.342 & -0.067 & 12.227 & 0.059 \\ 0.237 & -0.438 & -0.018 & 0.067 & 0.059 & 12.674 \end{pmatrix}.$$

The resulting diabatic PECs of CO·Mg are given in Fig. 5.7. The corresponding electronic couplings between the $B^1\Sigma^+$ and the $D'^1\Sigma^+$ state are depicted
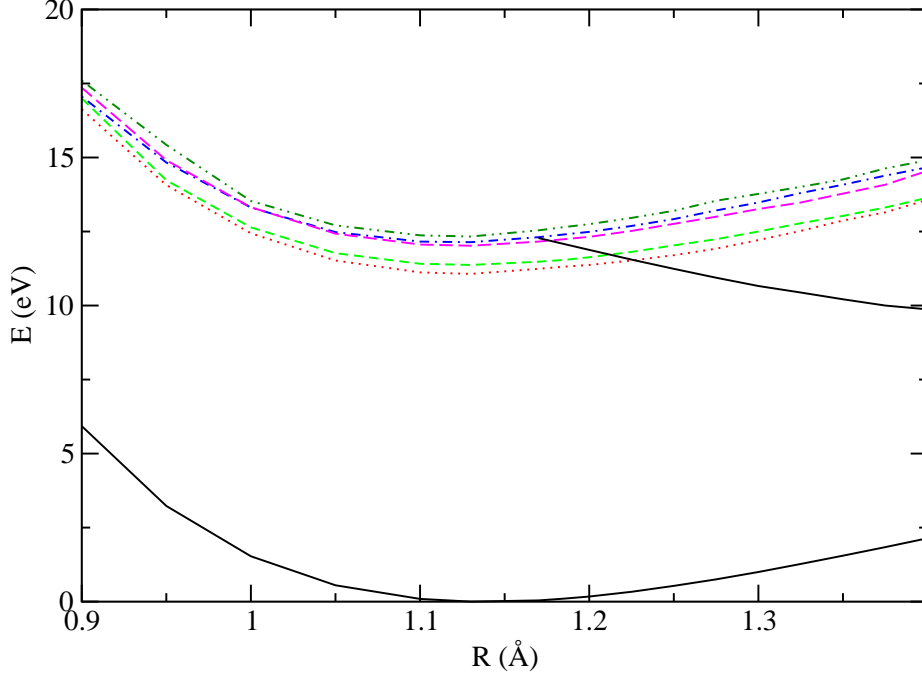
Figure 5.7: The ground state and the six energetically lowest excited states of CO·Mg of Σ^+ symmetry given in the diabatic basis obtained by means of the block diagonalization method.

in Fig. 5.8. Moreover, Fig. 5.8 contains the electronic couplings between the afore mentioned states and the corresponding electronic couplings of the RKR two-state model. Comparing the electronic couplings in CO and CO·Mg shows that the interaction between the states is hardly affected by the presence of Mg. Especially, in the region of the well the agreement is very good. At larger and smaller inter-nuclear distances the deviations are slightly larger but there the impact of the coupling is generally weaker due to the larger energy difference between the states. Moreover, the couplings of the RKR model are in decent agreement with the computed ones. At larger and smaller inter-nuclear distances the ADC method overestimates and underestimates the couplings, respectively. Since the ICD widths depend on the oscillator strength (3.41) and because the oscillator strength of the valence state is much larger than the one of the Rydberg state [163], it can be assumed that the ICD width of the first adiabatic excited state (which corresponds to the diabatic Rydberg state at small inter-nuclear distances) is underestimated at small inter-nuclear distances of CO and overestimated at large ones. However, since the deviations are moderate, we do assume that the obtained widths are reasonable and go well together with the
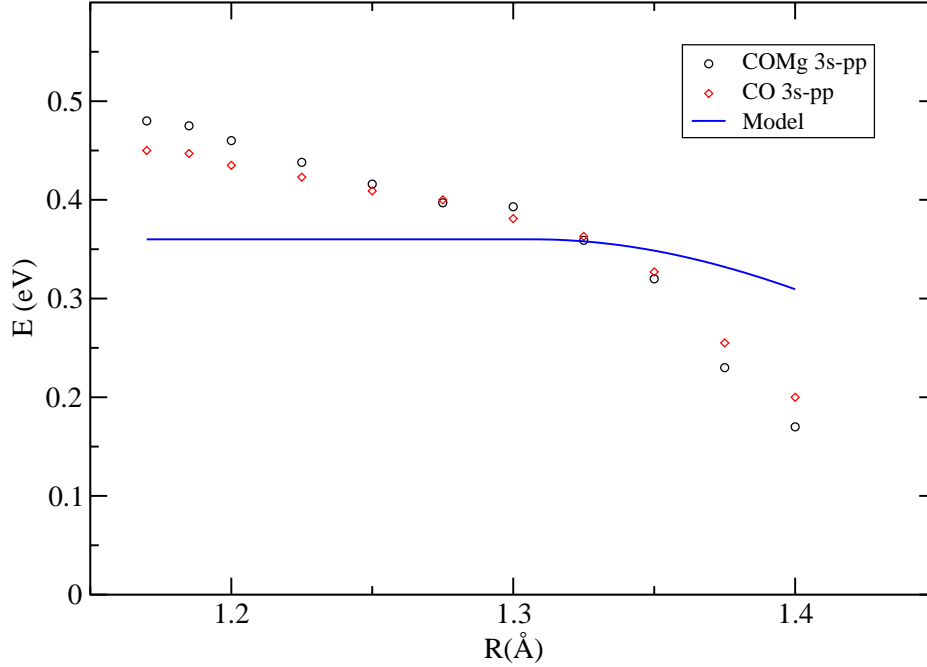
Figure 5.8: Comparison of the electronic couplings between the $B^1\Sigma^+$ and the $D^1\Sigma^+$ state in CO and CO·Mg at several inter-nuclear distances between C and O. The couplings were obtained by means of the block diagonalization method. The continuous line depicts the electronic couplings of the RKR model.

RKR model. The most important inclusion, however, is that the interaction of the states of interest is only insignificantly affected by the presence of Mg. Thus, it is reasonable to work with the quantities of isolated CO to describe the nuclear dynamics of CO in CO·Mg.

5.4 Quenching Predissociation by ICD: Explicit Computations

In this section we study how the dynamics in $B^1\Sigma^+$ Rydberg state of CO change in the presence of Mg. In the presence of Mg, which is only weakly bound to CO, the photoinduced dissociation of CO in the higher vibrational levels of the $B^1\Sigma^+$ state takes place too. However, the $B^1\Sigma^+$ state is higher in energy than the ionization potential of Mg and, hence, the ICD channel is open

$$(CO)^* \cdots Mg \rightarrow CO \cdots Mg^+ + e^-. \tag{5.18}$$

Consequently, the evolution of the system is governed by the competition between the dynamics of CO and the ICD. The goal of the this section is to investigate this competition.

Equations of Nuclear Motion

At the inter-nuclear distances $0.8\ \text{Å} \leq R \leq 1.4\ \text{Å}$ of CO, the excitation energies of both the $B^1\Sigma^+$ and the $D'^1\Sigma^+$ state are higher than the ionization potential of the neighboring Mg atom. Thus, both states can decay by ICD in this interval. How the nuclear dynamics of CO are affected by the additional decay pathway has to be investigated. To this end, we derive working equations in the time-dependent and time-independent picture to understand and describe the nuclear dynamics. The derivation in the time-independent picture is helpful to understand the impact of ICD on the coupled resonant states and, as will become apparent below, the time-dependent picture is more convenient to conduct the calculations.

In the presence of a weakly bound neighbor, all bound states above the ionization potential of the neighbor turn into resonances. Since the $B^1\Sigma^+$ and the $D'^1\Sigma^+$ state interact with each other, two overlapping resonances have to be considered here. Overlapping resonances have also been topic of the works of Royal [172], Hazi [173] Estrada [174], and Feuerbacher [175]. However, the situation at hand, two states which can decay due to ICD and are coupled non-adiabatically via an avoided crossing, has not been investigated yet. While PECs of bound states are represented in the adiabatic or a diabatic picture, the complex PECs of overlapping resonances require an extension of those representations. Consequently, the following pictures are introduced:

- *Complex Adiabatic Picture*: the real and the imaginary part of the electronic energy matrix are diagonal; the PECs are coupled non-adiabatically via the kinetic energy operator of the nuclei.

- *Complex Diabatic Picture*: the real and the imaginary part of the electronic energy matrix can exhibit off-diagonal elements. The real off-diagonal elements stem from the direct coupling of the electronic states since the diabatic states are no eigenstates of the electronic Hamiltonian. The imaginary couplings stem from the coupling through the electronic continuum.

In the present case, it is more convenient to work in the *Complex Diabatic Picture*. That is why we derive the working equations using diabatic resonant states.

Time-Independent Approach

Working equations which depend on the diabatic representation of the Rydberg $B^1\Sigma^+$, the valence $D^1\Sigma^+$ state, as well as the coupling between them are derived.

The use of the PECs corresponding to the ICD final states, which are unknown, is circumvented by introducing optical potentials [46, 83, 173, 176, 177]. As a result, ICD widths enter the equations.

Starting point of the derivation is the total wave function

$$|\Psi\rangle = |\phi_R\rangle|\chi_R\rangle + |\phi_V\rangle|\chi_V\rangle + \sum_j \int dE' c_{E',j}|\psi_{E',j}\rangle, \tag{5.19}$$

where $|\phi_R\rangle$ and $|\phi_V\rangle$ are the resonant electronic states in CO·Mg which consist of the $B^1\Sigma^+$ Rydberg $|\tilde{\phi}_R\rangle$ and the $D^1\Sigma^+$ valence $|\tilde{\phi}_V\rangle$ state of CO, respectively, and Mg in its ground state $|\phi_G^{Mg}\rangle$. Due to the weak interaction, the electronic states of CO·Mg can be written as direct products of the states of CO and that of Mg

$$|\phi_R\rangle = |\tilde{\phi}_R\rangle|\phi_G^{Mg}\rangle, \tag{5.20}$$
$$|\phi_V\rangle = |\tilde{\phi}_V\rangle|\phi_G^{Mg}\rangle. \tag{5.21}$$

The corresponding nuclear wave functions, $|\chi_R\rangle$ and $|\chi_V\rangle$, respectively, are given by a set of discrete vibrational functions $u_\nu(R)$ and a set of scattering states $u_E(R)$

$$|\chi_R\rangle = \sum_\nu a_\nu u_\nu(R), \tag{5.22}$$

$$|\chi_V\rangle = \int dE b_E u_E(R). \tag{5.23}$$

The non-resonant final states of the ICD process in CO·Mg are given by

$$|\psi_{E,j}\rangle = |\phi_0\rangle|\phi_{Mg}^+\rangle \sum_\tau n_\tau(R) f_{j,\tau}(E_k), \tag{5.24}$$

where E_k the kinetic energy of the outgoing electron. The states consist of the wave function of CO in its ground state $|\phi_0\rangle$, the wave function representing the ionized Mg atom $|\phi_{Mg}^+\rangle$, and the wave function describing the electron in the continuum $f_{j,\tau}(E)$. $n_\tau(R)$ are the corresponding vibrational functions.

Inserting the ansatz (5.19) into the Schrödinger equation

$$\hat{H}|\Psi\rangle = E|\Psi\rangle, \quad \text{with} \quad \hat{H} = \hat{T}_N + \hat{H}_e, \tag{5.25}$$

where $\hat{T}_N$ denotes the kinetic energy operator of the nuclei and $\hat{H}_e$ the electronic part of the Hamiltonian, and multiplying the Schrödinger equation by $\langle\phi_R|$, $\langle\phi_V|$,

and $\langle\psi_{E',j}|$ from the left, respectively, yields three coupled equations

$$\left[\hat{T}_N + V_R - E\right]|\chi_R\rangle = -\langle\phi_R|\hat{H}_e|\phi_V\rangle|\chi_V\rangle - \int dE' c_{E',j}\langle\phi_R|\hat{H}_e|\psi_{E',j}\rangle,$$

(5.26a)

$$\left[\hat{T}_N + V_V - E\right]|\chi_V\rangle = -\langle\phi_V|\hat{H}_e|\phi_R\rangle|\chi_R\rangle - \int dE' c_{E',j}\langle\phi_V|\hat{H}_e|\psi_{E',j}\rangle,$$

(5.26b)

$$\left[E' - E\right]c_{E',j} = -\langle\psi_{E',j}|\hat{H}_e|\phi_V\chi_V\rangle_R - \langle\psi_{E',j}|\hat{H}_e|\phi_R\chi_R\rangle_R. \qquad (5.26c)$$

V_R and V_V are the respective electronic energies of $|\phi_R\rangle$ and $|\phi_V\rangle$ and the subscript R at the matrix elements means that it is to be integrated over the electronic and the nuclear coordinates. In order to decouple (5.26a) and (5.26b) from (5.26c), (5.26c) is solved for $c_{E',j}$. In order to deal with singularity of $c_{E',j}$ at $E = E'$, Dirac's formal solution [85]

$$c_{E',j} = \left\{\mathrm{P}\frac{1}{E - E'} + z(E)\delta(E - E')\right\}\sum_r \langle\psi_{E',j}|\hat{H}_e|\phi_r\chi_r\rangle_R, \qquad (5.27)$$

where $r = \{R, V\}$ and P indicates the principal value of the following quantity, has been used. In order to ensure outgoing boundary conditions $z(E)$ must be chosen as $z(E) = -i\pi$ [83].

Introducing the definitions

$$V_{rs} = \langle\phi_r|\hat{H}_e|\phi_s\rangle, \qquad (5.28a)$$

$$\tilde{\Lambda}_{rs} = \int dE' \int dR' \frac{\langle\psi_{E',j}(R')|\hat{H}_e|\phi_r\rangle_{R'}}{E - E' + i\epsilon}\langle\phi_s|\hat{H}_e|\psi_{E',j}(R)\rangle, \qquad (5.28b)$$

the system of equations for $|\chi_r\rangle$, $r, s = \{R, V\}$, decoupled from the nuclear motion in the non-resonant states is given by

$$(E - \hat{T} - V_r)|\chi_r\rangle = \sum_{s\neq r} V_{rs}|\chi_s\rangle + \sum_s \tilde{\Lambda}_{rs}\chi_s(R'). \qquad (5.29)$$

(5.28b) describes the decay of the resonant state due to the interaction with the electronic continuum. Inserting the explicit expressions for the non-resonant functions (5.24) into (5.28b)

$$\tilde{\Lambda}_{rs} = \int dE' \int dR' \sum_{j,\tau} \frac{\langle\phi_0\phi^+_{Mg}n_\tau(R')f_{j,\tau}(E_k)|\hat{H}_e|\phi_r\rangle}{E - E' + i\epsilon}$$

$$\times\langle\phi_s|\hat{H}_e|\phi_0\phi^+_{Mg}n_\tau(R)f_{j,\tau}(E_k)\rangle, \qquad (5.30)$$

shows that the interaction is non-local: the nuclear wave functions included in first matrix element depend on the integration variable R' while the functions

of the second matrix element depend on the inter-nuclear distance R. The non-locality complicates the solution of the system of equations significantly.

The non-locality can be removed by introducing approximations. First, we consider the diagonal elements $\tilde{\Lambda}_{rr}$. If the energy of the outgoing electron is significantly larger than the vibrational spacing in the final state, it is reasonable to assume that the matrix elements $\langle \phi_0 \phi_{Mg}^+ n_\tau(R) f_{j,\tau}(E_k) | \hat{H}_e | \phi_r \rangle$ are approximately independent of the vibrational level $n_\tau(R)$ and, hence, can be written as

$$n_\tau(R)\langle \phi_0 \phi_{Mg}^+ f(E_k) | \hat{H}_e | \phi_r \rangle = n_\tau(R)\langle \psi_E | \hat{H}_e | \phi_r \rangle, \tag{5.31}$$

where $|\psi_E\rangle = |\phi_0 \phi_{Mg}^+ f(E_k)\rangle$. Thus, the energy- and nuclear coordinate dependency of the matrix elements are separated. As a consequence, the electronic final states are only a function of the kinetic energy of the outgoing electron E_k which is completely determined by the total energy E and the energy difference of the electronic potential of the respective resonant state V_r and the electronic potential of the ionic final state $V_F = \langle \phi_0 \phi_{Mg}^+ | \hat{H}_e | \phi_0 \phi_{Mg}^+ \rangle$ at the inter-nuclear distance R. In CO·Mg this assumption is justified since the kinetic energy of the outgoing electron amounts to 3.1 eV which is considerably larger than the vibrational spacing of CO $E_{\Delta\nu} \approx 0.25$ eV. Under these circumstances, the energy is sufficient to populated enough vibrational levels to consider the sum over the vibrational levels to be approximately complete

$$\sum_\tau n_\tau(R') n_\tau(R) \approx \delta(R - R'). \tag{5.32}$$

This approximation is known as local approximation [83, 139]. Inserting the closure relation (5.32) into (5.30) leads to

$$\tilde{\Lambda}_{rr} = \int dE' \frac{\langle \psi_{E'} | \hat{H}_e | \phi_r \rangle \langle \phi_r | \hat{H}_e | \psi_{E'} \rangle}{E - E' + i\epsilon}. \tag{5.33}$$

Performing the integration over E' yields

$$\tilde{\Lambda}_{rr} = \Delta_{rr} - i\pi \langle \psi_E | \hat{H}_e | \phi_r \rangle \langle \phi_r | \hat{H}_e | \psi_E \rangle \tag{5.34}$$

where

$$\Delta_{rr} = \mathrm{P} \int dE' \frac{\langle \psi_{E'} | \hat{H}_e | \phi_r \rangle \langle \phi_r | \hat{H}_e | \psi_{E'} \rangle}{E - E'}. \tag{5.35a}$$

$\mathrm{P}\int$ means that the principal value of the integral is to be taken. The shift Δ_{rr} is real and it is of the order of the width [83, 173, 177]. For the states at hand the excitation energy V_r is much larger and, hence, Δ_{rr} is neglected. According to (2.18), the imaginary part of the diagonal elements $\tilde{\Lambda}_{rr}$ can be identified as the widths of the electronic state $|\phi_r\rangle$

$$\Gamma_r = 2\pi |\langle \psi_E | \hat{H}_e | \phi_r \rangle|^2. \tag{5.36}$$

Thus, due to the interaction with the continuum the resonant states acquire a finite width that is related to the lifetime of the state $\tau = 1/\Gamma$ [45].

Now, we consider the off-diagonal elements $\tilde{\Lambda}_{rs}$. The two matrix elements included in $\tilde{\Lambda}_{rs}$ depend on different resonant states. If it is assumed that the matrix elements are independent of the nuclear wave functions (5.31), the off-diagonal elements vanish at all inter-nuclear distances except in a small interval around the crossing point of the two resonances. The reason is that the resonant states, $|\phi_R\rangle$ and $|\phi_V\rangle$, cannot couple to the same non-resonant state $|\psi_E\rangle$ unless they overlap energetically. However, this can only happen where the states cross in the diabatic picture and in the small vicinity around that point, where the resonant states overlap due to their widths. There the local approximation can be employed and the corresponding expression reads

$$\tilde{\Lambda}_{rs} = \int dE' \frac{\langle\psi_E|\hat{H}_e|\phi_r\rangle\langle\phi_s|\hat{H}_e|\psi_E\rangle}{E - E' + i\epsilon}. \tag{5.37}$$

Performing the energy integration, the expression simplifies to

$$\tilde{\Lambda}_{rs} = \Delta_{rs} - i\pi\langle\psi_E|\hat{H}_e|\phi_r\rangle\langle\phi_s|\hat{H}_e|\psi_E\rangle \tag{5.38}$$

We define

$$\Gamma_{rs} = 2\pi\langle\psi_E|\hat{H}_e|\phi_r\rangle\langle\phi_s|\hat{H}_e|\psi_E\rangle. \tag{5.39}$$

Γ_{rs} cannot be calculated by means of the FSL methods. However, in the context of the local approximation it can be approximated by

$$\Gamma_{rs} = \sqrt{\Gamma_r}\sqrt{\Gamma_s}. \tag{5.40}$$

We have assumed that the real part Δ_{rs} is negligible since the electronic coupling is at least one order to magnitude larger in the present case. The physical meaning of the imaginary off-diagonal elements is complicated. From (5.29) and (5.37) one can deduce that they represent a coupling between the resonant states via the continuum and, simultaneously, they represent simultaneous decay from the two resonant states into the non-resonant states.

Making use of the local imaginary potentials, (5.36) and (5.40), the nuclear motion in the two coupled resonances can be described by

$$\left[\begin{pmatrix} \hat{T} & 0 \\ 0 & \hat{T} \end{pmatrix} + \begin{pmatrix} V_R - i\Gamma_R/2 & W - ig(R)\Gamma_{RV}/2 \\ W - ig(R)\Gamma_{VR}/2 & V_V - i\Gamma_V/2 \end{pmatrix} \right] \begin{pmatrix} |\chi_R\rangle \\ |\chi_V\rangle \end{pmatrix}$$
$$= E \begin{pmatrix} |\chi_R\rangle \\ |\chi_V\rangle \end{pmatrix}. \tag{5.41}$$

$g(R)$ is a step function which is equal to one in the interval where the resonances overlap and zero elsewhere. The relevant ICD widths vanish at inter-nuclear

distances larger than 1.4 Å. Theoretically, the system of equations (5.41) could be solved by inserting the ansätze for the nuclear wave functions (5.22) and solving for the coefficients. However, the functions representing $|\chi_V\rangle$ are non-$\mathcal{L}^2$ and, thus, the solution involves the evaluation of bound-continuum matrix elements. Numerically, it is much more convenient to compute the dynamics in the time-dependent picture.

Time-Dependent Approach

Physically the time-independent and the time-dependent pictures are completely equivalent; they merely provide different representations. In the present work the nuclear dynamics are carried out in the time-dependent picture by means of wave packet propagation [26, 34, 35]. We chose this picture because, firstly, the dynamics of CO in CO·Mg can be treated more conveniently and, secondly, a program to propagate wave packets was already at hand where the current working equations could be incorporated. There are several numerical methods to carry out the propagation and the reader is referred to textbooks in order to get an overview [26–28, 178]. In this work we use a method introduced by Pahl *et al* [34, 35] which is outlined below.

As a first step, the time-dependent working equations for two-state model of the CO·Mg system are derived. In our model the Mg atom is fixed with respect to the center of mass of CO which is why all nuclear time-dependent wave packets represent the dynamics of CO. Consequently, the total wave function $|\Psi_{tot}(t)\rangle$ can be written as

$$|\Psi_{tot}(t)\rangle = |\phi_R\rangle|\chi_R(t)\rangle + |\phi_V\rangle|\chi_V(t)\rangle + \sum_j \int dE |\psi_j(E)\rangle|\chi_j(E,t)\rangle \quad (5.42)$$

where $|\chi_j(E,t)\rangle$ is the wave packet of the final states of the ICD and the electronic functions $|\phi_r\rangle$ correspond to the corresponding states in CO·Mg (5.20) and $|\psi_j(E)\rangle$ represents the electronic state CO·Mg$^+$ and the electron in the continuum with kinetic energy E. Inserting (5.42) into the time-dependent Schrödinger equation

$$i|\dot{\Psi}_{tot}\rangle = \hat{H}|\Psi_{tot}\rangle, \quad \hat{H} = \hat{T} + \hat{H}_e \quad (5.43)$$

and multiplying it from the left with $\langle\phi_R|$, $\langle\phi_V|$, and $\langle\psi_j(E)|$, respectively, yields three coupled equations

$$i|\dot{\chi}_R(t)\rangle = (\hat{T} + V_R)|\chi_R(t)\rangle + W|\chi_V(t)\rangle + \sum_j \int \Lambda_{R,j}|\chi_j(t)\rangle dE, \quad (5.44a)$$

$$i|\dot{\chi}_V(t)\rangle = (\hat{T} + V_V)|\chi_V(t)\rangle + W^\dagger|\chi_R(t)\rangle + \sum_j \int \Lambda_{V,j}|\chi_j(t)\rangle dE, \quad (5.44b)$$

$$i|\dot{\chi}_j(t)\rangle = (\hat{T} + V_0 + E)|\chi_j(t)\rangle + \Lambda_{R,j}^\dagger|\chi_R(t)\rangle + \Lambda_{V,j}^\dagger|\chi_V(t)\rangle. \quad (5.44c)$$

The following definitions were used in (5.44)

$$V_r = \langle\phi_r|\hat{H}_e|\phi_r\rangle, \quad r = R, V, \tag{5.45}$$

$$V_0 + E = \langle\psi_j(E)|\hat{H}_e|\psi_j(E)\rangle, \tag{5.46}$$

$$W = \langle\phi_R|\hat{H}_e|\phi_V\rangle, \tag{5.47}$$

$$\Lambda_{R,j}(E) = \langle\phi_R|\hat{H}_e|\psi_j(E)\rangle, \tag{5.48}$$

$$\Lambda_{V,j}(E) = \langle\phi_V|\hat{H}_e|\psi_j(E)\rangle. \tag{5.49}$$

In order to decouple the nuclear motion in the two resonant states, $|\phi_V\rangle$ and $|\phi_V\rangle$, from the nuclear motion in the final states $|\psi_j(E)\rangle$, we can express $|\chi_j(t)\rangle$ by its formal solution

$$|\chi_j(t)\rangle = -i\int_{-\infty}^{t} e^{i(\hat{T}+V_0+E)(t'-t)}[\Lambda_{R,j}|\chi_R(t')\rangle + \Lambda_{V,j}|\chi_V(t')\rangle]dt' \tag{5.50}$$

and insert the solution into the equations of motion for the resonant states

$$i|\dot{\chi}_r(t)\rangle = (\hat{T}+V_V)|\chi_r(t)\rangle + W|\chi_s(t)\rangle \tag{5.51}$$
$$- i\sum_j \int dE' \int dt' \Lambda_{r,j}^{\dagger}(E')e^{i(\hat{T}+V_0+E)(t'-t)}\Lambda_{s,j}(E)|\tilde{\chi}_R(t')\rangle$$
$$- i\sum_j \int dE' \int dt' \Lambda_{r,j}^{\dagger}(E')e^{i(\hat{T}+V_0+E)(t'-t)}\Lambda_{r,j}(E)|\tilde{\chi}_V(t')\rangle.$$

By introducing the local approximation as done above in the time-independent picture and evaluating the time integrals [34] one obtains

$$i|\dot{\chi}_R(t)\rangle = (\hat{T}+V_R-i\Gamma_R/2)|\chi_R(t)\rangle + (W-ig(R)\Gamma_{RV}/2)|\chi_V(t)\rangle, \tag{5.52a}$$
$$i|\dot{\chi}_V(t)\rangle = (\hat{T}+V_V-i\Gamma_V/2)|\chi_R(t)\rangle + (W-ig(R)\Gamma_{VR}/2)|\chi_R(t)\rangle, \tag{5.52b}$$

where

$$\Gamma_R = 2\pi\Lambda_R^{\dagger}\Lambda_R, \tag{5.53a}$$

$$\Gamma_V = 2\pi\Lambda_V^{\dagger}\Lambda_V, \tag{5.53b}$$

$$\Gamma_{RV} = \Gamma_{VR} = 2\pi\Lambda_R^{\dagger}\Lambda_V = 2\pi\Lambda_V^{\dagger}\Lambda_R, \tag{5.53c}$$

with

$$\Lambda_r = \langle\phi_r|\hat{H}_e|\psi(E)\rangle. \tag{5.54}$$

Now, $|\psi(E)\rangle$ depends only on the energy of the outgoing electron. As discussed above, the step function $g(R)$ ensures that the imaginary off-diagonal couplings only occur in a small interval around the crossing point of the real part of the

diabatic PECs. The system of equations describing the nuclear dynamics is completed by the equation for the nuclear dynamics in the final state

$$i|\dot{\chi}(E,t)\rangle = (\hat{T} + V_0 + E)|\chi(E,t)\rangle + \Lambda_R|\chi_R(t)\rangle + \Lambda_V|\chi_V(t)\rangle. \tag{5.55}$$

The nuclear dynamics are affected by the way the involved excited states are populated. In our model we assume an optical excitation from the ground state of CO·Mg to the $B^1\Sigma^+$ Rydberg state $|\phi_R\rangle$. The coupling between the ground and the Rydberg state due to the electromagnetic field is given by

$$\hat{F}(t) = \langle\phi_R|\hat{\mathbf{D}}|\phi_0\rangle \cdot \mathbf{E}(t), \tag{5.56}$$

where $\hat{\mathbf{D}}$ is the dipole operator and $\mathbf{E}(t)$ denotes the electric field. The coupling via the electric field causes oscillation-like populating and depopulating of the two electronic states. In the equation of the nuclear wave packets of the Rydberg $|\chi_R(t)\rangle$ (5.52) and the ground state $|\chi_0(t)\rangle$

$$i|\dot{\chi}_0(t)\rangle = [\hat{T}_N + V_I]|\chi_0(t)\rangle, \tag{5.57}$$

where V_I is the electronic potential of the ground state of CO·Mg, $\hat{F}(t)|\chi_0(t)\rangle$ and $\hat{F}^\dagger(t)|\chi_R(t)\rangle$, respectively, would appear as additional inhomogeneities. In general, $\hat{F}(t)$ can be expressed by the product of the transition operator $\hat{V}$ which contains the dependence on the nuclear coordinates and the time-dependent excitation function $g(t)$ [34]

$$\hat{F}(t) = \hat{V}g(t). \tag{5.58}$$

Here we simplify the description by assuming, firstly, that the weak field approximation is valid. Id est, there is no coupling back from the Rydberg state to the ground state due to the electro-magnetic field [34,35]. Hence, there is no inhomogeneity in the equations for $|\chi_0(t)\rangle$. Secondly, we assume that the excitation is induced by a broad band excitation: the excitation function $g(t)$ can be approximated by a δ-function in time. So, there is no inhomogeneity in the equations of motion of $|\chi_R(t)\rangle$ due to the excitation process; instead the inhomogeneity is substituted by the initial condition

$$|\chi_R(0)\rangle = |\chi_0(0)\rangle, \tag{5.59}$$

where $|\chi_0(t)\rangle$ represents the nuclear wave function in the ground state.

Another important aspect which has to be considered is the repulsive nature of the valence state. Once the wave packet has reached the valence state and passed through the region where the ICD channel is open, the wave packet propagates

towards larger inter-nuclear distances and might reach the end of the grid before the dynamics are completed and, thus, provoke unphysical effects. To prevent this a CAP was placed at an inter-nuclear distance of 1.6 Å between C and O [35, 76]. The CAP absorbs the wave packet before it can reach the end of the grid. This has to be taken into account in calculations of the population of the states: due to the CAP $\hat{C}$ the norm changes in time as [34, 35]

$$\frac{d}{dt}\langle\chi(t)|\chi(t)\rangle = -2\langle\chi(t)|\hat{C}|\chi(t)\rangle. \tag{5.60}$$

In this work we used a CAP of the form

$$\hat{C} = \eta(x - x_0)^3\theta(x - x_0), \tag{5.61}$$

where $x_0 = 1.6$ Å, $\theta(x - x_0)$ is the Heaviside step function, and $\eta = 0.01$ eV/Å.

The computational details of the propagation scheme applied can be found in Ref. [34, 35]. Here we only outline the procedure: First, the initial wave packet has to be determined. To this end, the Schrödinger equation of the nuclear wave function of the ground state (5.57) is solved. That is achieved by diagonalizing the corresponding Hamiltonian which is represented by a discrete variable representation [179, 180]. Since we consider a broad band excitation the wave packet is simply put on the surface of the excited state at $t = 0$. There the packet starts to propagate immediately. The numerical propagation is achieved by diagonalizing the complex Hamiltonian matrix at every time-step by means of the Lanczos-Arnodli method [181] which is the generalization of the Lanczos method [182, 183]. The application of $\hat{H}$ on $|\Psi\rangle$ is done by a fast Fourier transformation [184]. In the calculations for the present work the grid where the wave packets could move on was based on the PECs from Fig. 5.1 and it ranged from 0.8 to 1.65 Å. The corresponding Hamilton operator was represented by a DVR with a spacing of 0.005 Å. We used a time step size of 0.1 fs for the time integration.

The ICD Width of CO·Mg

The working equations (5.41) and (5.52) depend on the PECs, V_R and V_V, and the electronic coupling W. All those quantities are associated with the diabatic representations of the Rydberg and the valence state. Moreover, the working equations depend on the ICD widths Γ_R, Γ_V, and Γ_{RV} of those diabatic states. This is important, because the ICD widths obtained by means of the FSL program are not the corresponding ones. Consequently, the widths computed by means of our FSL program have to be transformed before they can be used in the working equations. Before we discuss the required transformation, the determination of the widths using our FSL program is discussed.
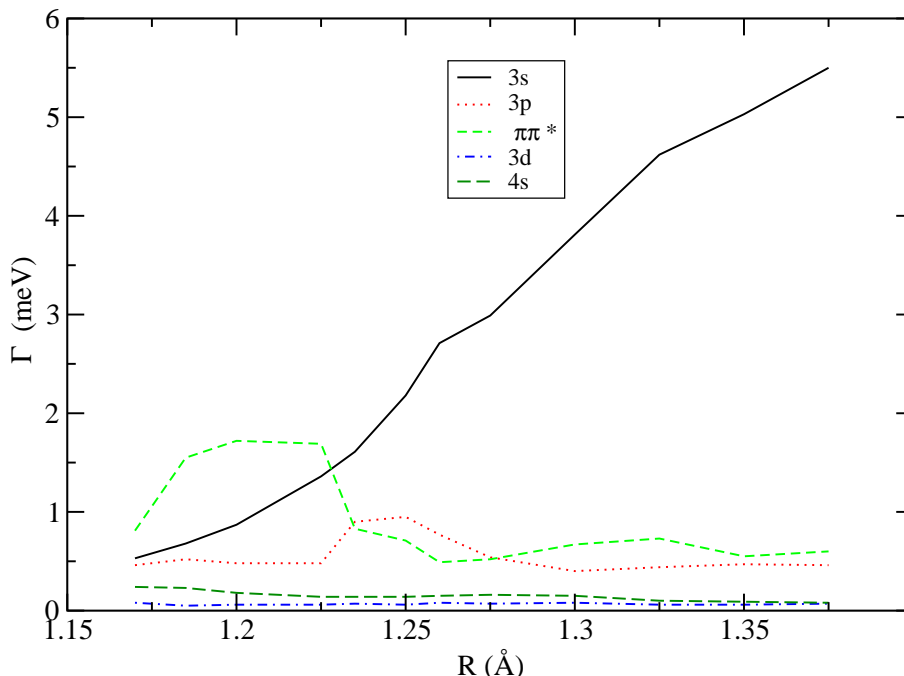
Figure 5.9: The figure shows the ICD widths of the five energetically lowest adiabatic excited states of CO·Mg of Σ^+ symmetry. The notation in the legend indicates the electronic character of the corresponding decaying state at small inter-nuclear distances.

In the calculations we employed the ADC(2)x method and used aug-cc-pVTZ basis sets [124] augmented with 3s, 3p, and 3d functions with Kaufmann exponents [125] centered on C and O. To represent Mg and the electron in the continuum we used the aug-cc-pVTZ basis set augmented with 5s, 5p, and 5d functions with even tempered exponents [128,129]. In order to represent the resonant states we used a configuration space which consists of all 1h1p configurations with one hole in the 3σ, 4σ, 5σ, and 1π MOs of CO. To account for electron correlation we included all possible 2h2p configurations having holes in the 3σ, 4σ, 5σ, and 1π MOs. The dimension of the resulting ADC matrix was around 80000. The decaying states of interest are at the bottom of the spectrum. Therefore, we computed them with the Davidson method [126]. The non-resonant final states of the decay consist of CO in its ground state and Mg$^+$ in its ground state. To describe these states including electron correlation, we included in the configuration space all 1h1p and 2h2p configurations with one or two holes in the Mg $3s$ orbital. In the Lanczos calculation of the non-resonant spectrum the starting block consisted of all 1h1p configurations.
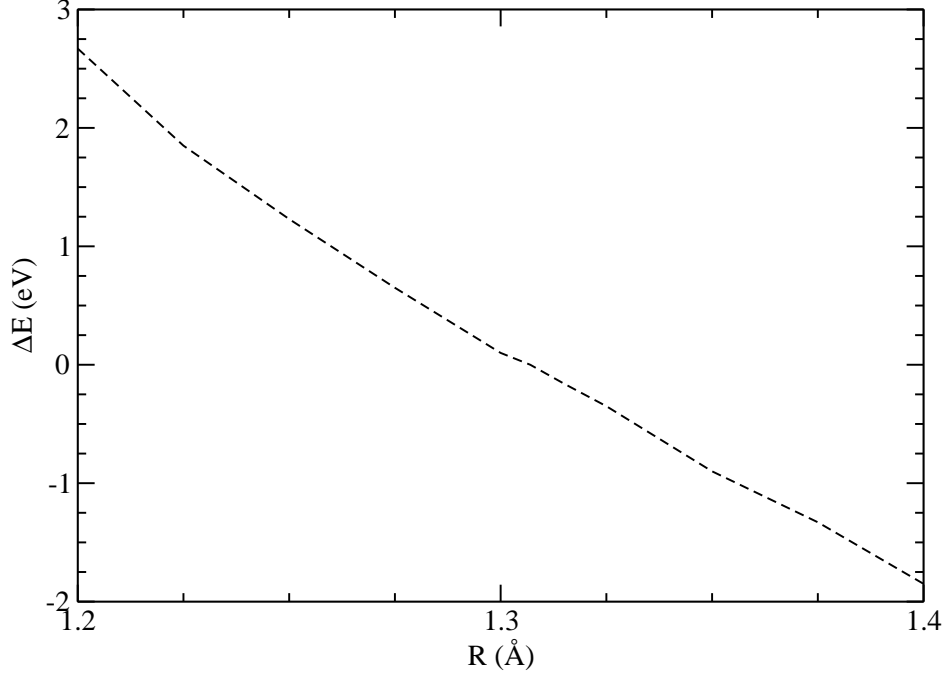
Figure 5.10: The figure shows the energy difference between the $D'^1\Sigma^+$ and the $B^1\Sigma^+$ states of the RKR model as a function of the inter-nuclear distance R between C and O.

The resulting widths are depicted in Fig. 5.9. The figure shows the widths of the five energetically lowest excited states of Σ^+ symmetry for inter-nuclear distances 1.17 Å $\leq R \leq$ 1.4 Å between C and O in CO·Mg. The graphs labeled by $3s$ and $\pi\pi^*$ are relevant for the dynamics we are interested in. Obviously, these two widths cross. This crossing stems from the electronic mixing of the $B^1\Sigma^+$ and the $D'^1\Sigma^+$ state. At small inter-nuclear distances the $3s$-width can be associated with the diabatic $B^1\Sigma^+$ state. At large inter-nuclear distances that widths belongs to the diabatic $D'^1\Sigma^+$ state. The widths labeled by $\pi\pi^*$ can be regarded as the widths of the diabatic $B^1\Sigma^+$ at large inter-nuclear distances and at small inter-nuclear distances it can be associated with the diabatic $D'^1\Sigma^+$ state. However, it is virtually impossible to resolve the adiabatic $D'^1(\pi\pi^*)\Sigma^+$ there and, thus, the calculated width is not reliable in that region. We account for that by letting the corresponding diabatic widths cease to zero at the beginning of that region (see the 'Mg Valence' width in Fig. 5.13). Thus, we may underestimate the width but are on the safe side.

Now, we consider how we can obtain the desired diabatic widths necessary in order to use the working equations. At first, we clarify which representation
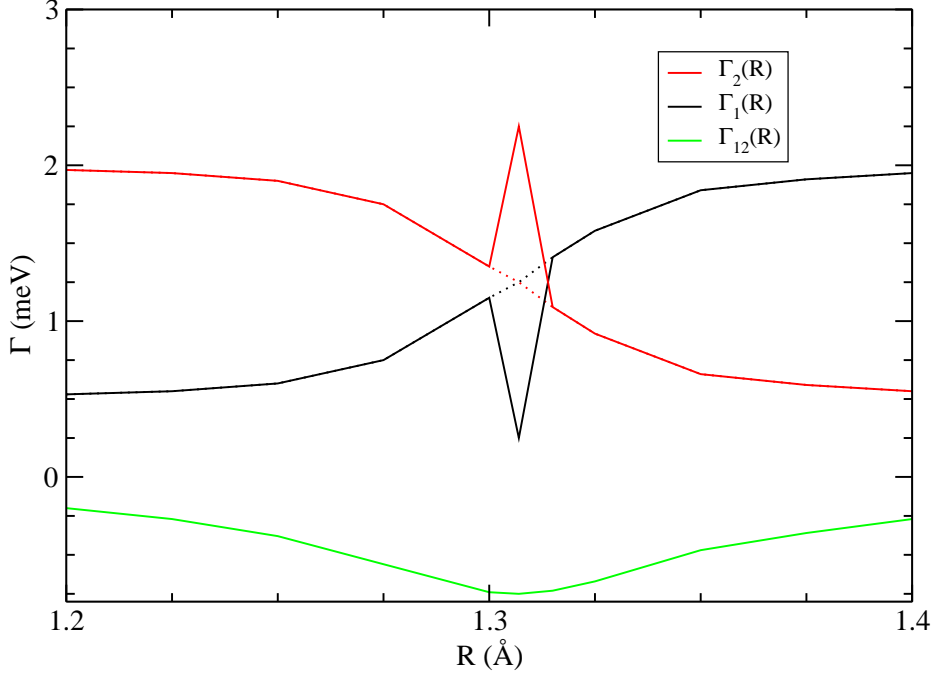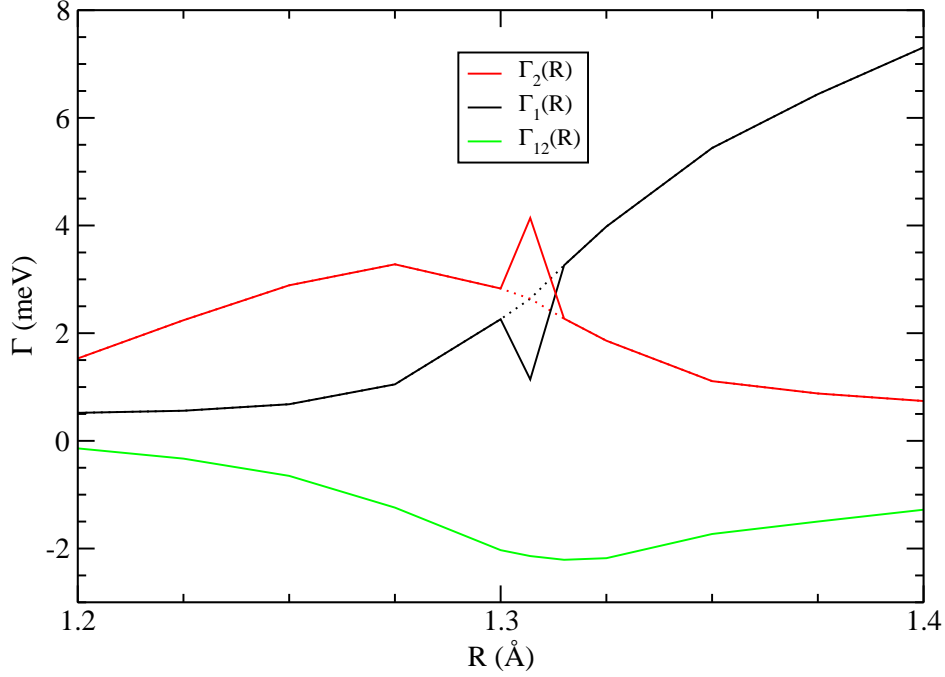
Figure 5.11: ICD widths Γ_1 and Γ_2 of the adiabatic $B^1\Sigma^+$ and the adiabatic $D'^1\Sigma^+$ state, respectively, and the off-diagonal coupling Γ_{12} obtained from the model of constant diabatic widths. See text for details.

the widths resulting from our FSL program belong to. The FSL program produces widths Γ_i associated with states of energy E_i which are not adiabatic with respect to the full Hamiltonian; rather they are *"adiabatic"* with respect to $\hat{Q}\hat{H}\hat{Q}$. In the problem considered here, the contribution of the residual part of the electronic Hamiltonian $\hat{P}\hat{H}\hat{P}$ to E_i is small: due to the interaction with the (non-resonant) $\hat{P}\hat{H}\hat{P}$ part of the Hamiltonian the (resonant) $\hat{Q}\hat{H}\hat{Q}$ states are energetically shifted. However, the shift is small and can be neglected [45, 46]. For that reason, we denote the representation as *adiabatic* in the following, i.e., the calculated widths (resulting from the FSL program) are adiabatic ones. On the other hand, the contribution of $\hat{P}\hat{H}\hat{P}$ to Γ_i is significant. Consequently, the imaginary part can introduce couplings between the states. Hence, widths obtained with the aid of the FSL program do not belong to the *Complex Adiabatic Picture*.

Since it is convenient to use the diabatic RKR model to carry out the nuclear dynamics we would like to work in the *Complex Diabatic Picture* where the PECs, the corresponding electronic couplings, and the widths are determined by the

diabatic states. In the present case, the PECs and the couplings are known but the widths are unknown and they cannot be calculated directly. Thus, it is necessary to connect them to the widths resulting from FSL calculations with the aid of a transformation.

Figure 5.12: ICD widths Γ_1 and Γ_2 of the adiabatic $B^1\Sigma^+$ and the adiabatic $D'^1\Sigma^+$ state, respectively, and the off-diagonal coupling Γ_{12} obtained from the model of diabatic widths where Γ_R is constant and Γ_V increases linearly. See text for details.

The transformation, $\underline{\mathbf{F}}$, that links the widths of the FSL program Γ_i, $i = 1, 2, 12$ to the widths of the diabatic states Γ_r, $r = R, V, RV$ is given by the eigenvectors of the diabatic energy matrix

$$\begin{pmatrix} V_R & W \\ W & V_V \end{pmatrix}. \tag{5.62}$$

In (5.62) W denotes the electronic coupling and V_r, $r = \{R, V\}$, are the energies of the diabatic states. If the transformation is known the matrix of widths $\underline{\mathbf{\Gamma}}^{AD}$ obtained by means of the FSL program can be obtained from the matrix of diabatic widths $\underline{\mathbf{\Gamma}}^D$:
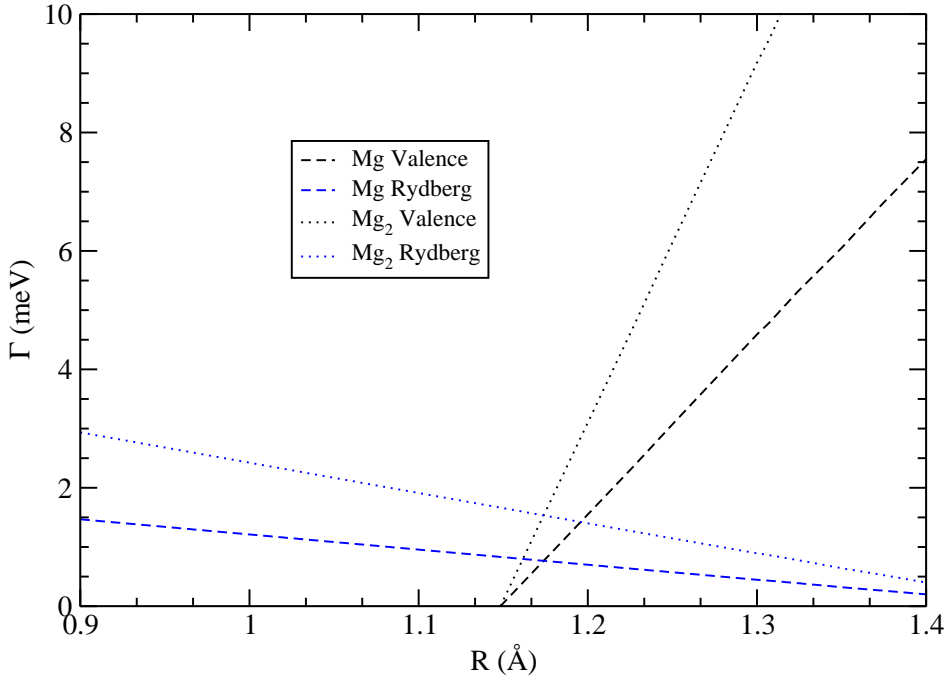
$$\underline{\mathbf{\Gamma}}^{AD} = \underline{\mathbf{F}}\,\underline{\mathbf{\Gamma}}^D\underline{\mathbf{F}}^\dagger = \begin{pmatrix} \Gamma_1 & \Gamma_{12} \\ \Gamma_{12} & \Gamma_2 \end{pmatrix}, \tag{5.63}$$

where

$$\underline{\mathbf{\Gamma}}^D = \begin{pmatrix} \Gamma_R & \Gamma_{RV} \\ \Gamma_{RV} & \Gamma_V \end{pmatrix} \tag{5.64}$$

Since we use the PECs and the coupling of the RKR model [29], the transformation is obtained from the corresponding parameters.

Figure 5.13: The optimal models of the diabatic widths of the $B^1\Sigma^+$ Rydberg and the $D'^1\Sigma^+$ valence states in CO·Mg and CO·Mg$_2$, respectively. Optimal means that the depicted diabatic widths reproduce the calculated adiabatic widths most accurately upon transformation into the adiabatic picture (see text for details). For CO·Mg the adiabatic widths following from the transformation of the depicted ones are given in Fig. 5.14.

Before we apply the transformation, we investigate theoretically how the transformation modifies the widths. To this end, we consider the simple two-state model where the adiabatic representation of the resonant states, $|\phi_1\rangle$ and $|\phi_2\rangle$ are given by

$$|\phi_1\rangle = (1 - c^2)^{\frac{1}{2}}|\phi_R\rangle + c|\phi_V\rangle, \tag{5.65a}$$

$$|\phi_2\rangle = -c|\phi_R\rangle + (1 - c^2)^{\frac{1}{2}}|\phi_V\rangle. \tag{5.65b}$$

$|\phi_R\rangle$ and $|\phi_V\rangle$ denote diabatic representations of the resonant states and $0 \leq c \leq 1$ is a mixing coefficient depending on the inter-nuclear distance. Inserting the (5.65) into the expression for the widths, (5.36) and (5.39), yields

$$\Gamma_1 = \Gamma_R + c^2[\Gamma_V - \Gamma_R] + 2c(1 - c^2)^{\frac{1}{2}}\langle\phi_V|\hat{H}_e|\psi\rangle\langle\psi|\hat{H}_e|\phi_R\rangle \tag{5.66a}$$

$$\Gamma_2 = \Gamma_V + c^2[\Gamma_R - \Gamma_V] - 2c(1 - c^2)^{\frac{1}{2}}\langle\phi_R|\hat{H}_e|\psi\rangle\langle\psi|\hat{H}_e|\phi_V\rangle \tag{5.66b}$$

$$\Gamma_{12} = c(1 - c^2)^{\frac{1}{2}}[\Gamma_V - \Gamma_R] + \langle\phi_R|\hat{H}_e|\psi\rangle\langle\psi|\hat{H}_e|\phi_V\rangle$$
$$- 2c^2\langle\phi_V|\hat{H}_e|\psi\rangle\langle\psi|\hat{H}_e|\phi_R\rangle. \tag{5.66c}$$

The corresponding expressions of the diabatic picture follow by setting $c = 0$. One can read from (5.66) that in the adiabatic picture the imaginary off-diagonal element Γ_{12} can be non-zero even far off the crossing. Since Γ_{12} cannot be calculated directly and depends on the electronic mixing of the states, it is very difficult to estimate it reasonably. Thus, we cannot obtain the diabatic widths from the ones calculated by means of the FSL method directly via a transformation simply because the the off-diagonal elements are missing.

Although the information provided by the width calculations of the FSL program are not sufficient to obtain the diabatic widths via a transformation and, although, the diabatic widths Γ_r, $r = R, V, RV$ cannot be calculated directly, it is possible to set up reasonable models for the widths of the *Complex Diabatic Picture* by guessing Γ_r, $r = R, V$. They can be guessed reasonably by considering asymptotic values of the widths resulting from the FSL computations Γ_i, $i = 1, 2$. As already mentioned above, at small inter-nuclear distances between C and O, the first adiabatic excited state (see Fig. 5.6) corresponds to the diabatic $B^1\Sigma^+$ state. Hence, we can assume that $\Gamma_1 \approx \Gamma_R$ there. Additionally, at large inter-nuclear distances it holds $\Gamma_2 \approx \Gamma_R$ Moreover, the first adiabatic excited state corresponds to the diabatic $D'^1\Sigma^+$ state at large inter-nuclear distances and, consequently, one can suppose $\Gamma_1 \approx \Gamma_V$ there. Since the electronic character of diabatic states depends only minor on the inter-nuclear distance, it can be assumed that widths of diabatic states are close to straight lines. The gradient of the widths is of course more difficult to guess. Whether the asymptotic value and the guessed shape are reasonable can be check by transforming the widths of the model back to the adiabatic picture. Then they can be compared to the calculated widths depicted in Fig. 5.9. As a side product we obtain the full $\underline{\mathbf{\Gamma}}^{AD}$ which can be diagonalized subsequently in order to obtain the complex PECs of the *Complex Adiabatic Picture*. This is potentially interesting because it could help to understand features of widths calculated by means of CAPs or complex scaling.

The first model, which we set up, supposed that the widths of both, the $B^1\Sigma^+$ and the $D'^1\Sigma^+$ state, are constants with respect to the inter-nuclear distance between C and O. We chose the constants with respect to the *ab initio* FSL
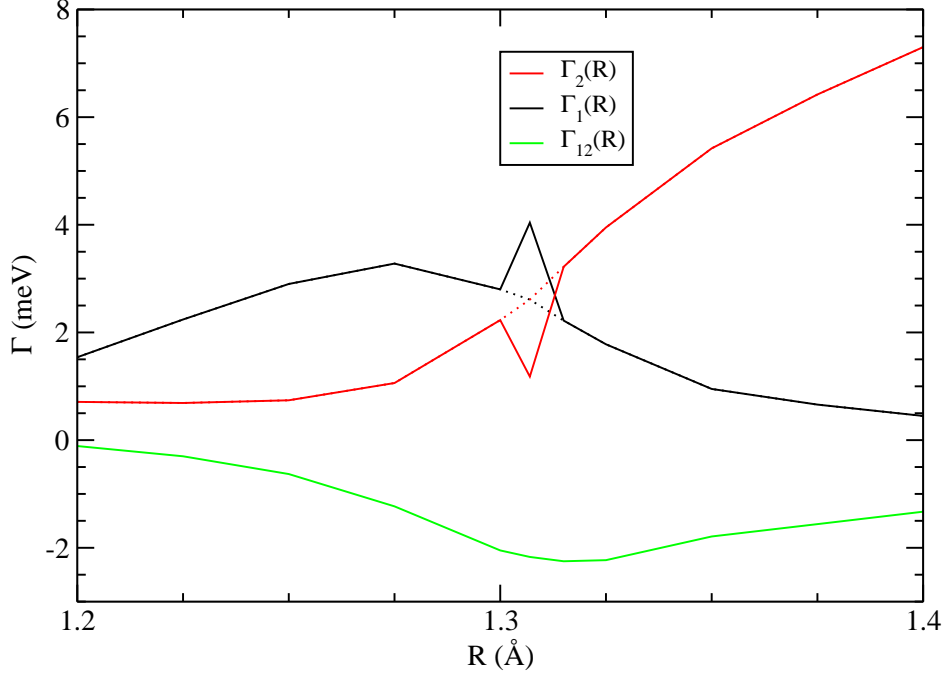
Figure 5.14: ICD widths Γ_1 and Γ_2 of the adiabatic $B^1\Sigma^+$ and the adiabatic $D'^1\Sigma^+$ state, respectively, and the off-diagonal coupling Γ_{12} obtained from the model of diabatic widths depicted in Fig. 5.13. See text for details.

widths given in Fig. 5.9. For the width of the $B^1\Sigma^+$ Rydberg and the $D'^1\Sigma^+$ valence state we chose 0.5 meV and 2.0 meV, respectively. According to Fig. 5.9 the choice of the widths for the valence state seems to be pretty low. However, the starting with a value below average ensures that we do not overestimate the impact of ICD. Using the electronic coupling (Fig. 5.8) and the PECs from the RKR model (Fig. 5.1) to define the transformation $\underline{\mathbf{F}}$ (5.63), we obtained the adiabatic widths depicted in Fig. 5.11. Now, the obtained widths can be compared to the calculated widths given in Fig. 5.9: the model reproduces the widths at small inter-nuclear distances decently. The crossing point of the widths occurs at larger inter-nuclear distances, which can be explained by the fact, that the crossing of the PECs in the RKR model occurs at larger inter-nuclear distances too. At larger inter-nuclear distances, the rise of the first adiabatic state is not reproduced and the widths of the second adiabatic state is too large. The peaks of the solid lines in Fig. 5.11 are caused by Γ_{RV} which is non-zero at the crossing point in the *Complex Diabatic Picture*. The values of Γ_{RV} were determined with the aid of (5.40). Since we performed the transformation only at a finite number

of inter-nuclear distances, the peaks exhibit an unphysical shape and are way too broad. The exact shape of the peaks is unknown, however, since we do not use the adiabatic widths in calculations, the knowledge of the exact shape is not crucial here. (5.66) shows why the peaks do not occur in calculated adiabatic widths depicted in Fig. 5.9: the $\langle\phi_V|\hat{H}_e|\psi\rangle\langle\psi|\hat{H}_e|\phi_R\rangle$ terms are not taken into account in the calculations of the FSL method.

In order to improve the agreement of the model and the *ab initio* results, we set up a second model where the width of the valence state Γ_V increases linearly. As a consequence, we expect to reproduce the enhancement of Γ_{3s} from Fig. 5.9 better at large inter-nuclear distances. The explicit values of Γ_V as functions of the inter-nuclear distance between C and O are depicted in Fig. 5.13. As in the preceding model, the widths of the Rydberg state Γ_R was taken to be a constant of 0.5 meV. Carrying out the transformation (5.63) for this model, the adiabatic widths depicted in Fig. 5.12 are obtained. From the figure one can see, that the slope of the second adiabatic state is reproduced better than in the previous model. However, at large inter-nuclear distances, Γ_2 is still too high. At 1.4 Å it is about 1.6 meV while the corresponding values is 0.55 meV in Fig. 5.9. As a consequence, we set up another diabatic model where Γ_R decreases linearly with the inter-nuclear distance. Both widths used in this third model, Γ_R and Γ_V are given explicitly in Fig. 5.13. The corresponding adiabatic widths resulting from the transformation (5.63), are shown in Fig. 5.14. At large inter-nuclear distances the values of Γ_2 are in agreement with the values from the *ab initio* calculations. Moreover, since the overall agreement is very good we decided use this model in order to carry out the dynamics in the *Complex Diabatic Picture*.

Visualization and Interpretation of the Time Propagation

In order to interpret the results of the propagation, we calculate the change in the population of the states as the system evolves. At all times t it holds

$$\frac{d}{dt}\langle\Psi_{tot}(t)|\Psi_{tot}(t)\rangle = 0. \tag{5.67}$$

In order to monitor the populations of the involved states, we determine the evolution of the norms of $|\chi_R(t)\rangle$, $|\chi_V(t)\rangle$, and $|\chi(E,t)\rangle$. The evolution of the
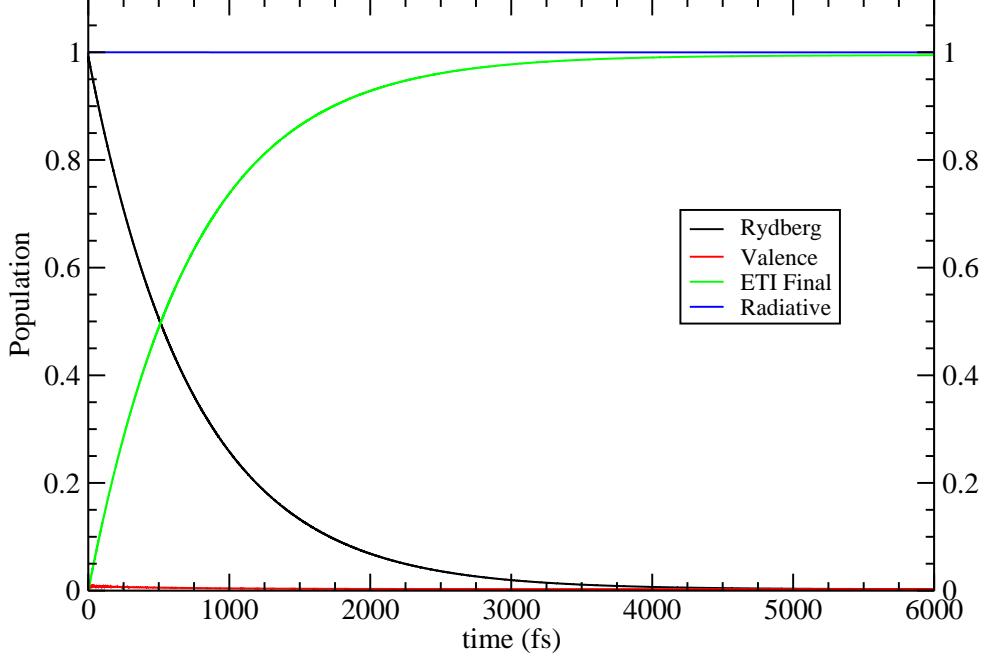
Figure 5.15: Changes in the population in time after an excitation into the lowest vibrational level of the $B^1\Sigma^+$ Rydberg state using the diabatic ICD widths given in Fig. 5.13. Additionally, the depopulation of the Rydberg state due to radiative decay (in the absence of ICD) is depicted.

norm of $|\chi_R(t)\rangle$ in time can be determined using the result from (5.52a)
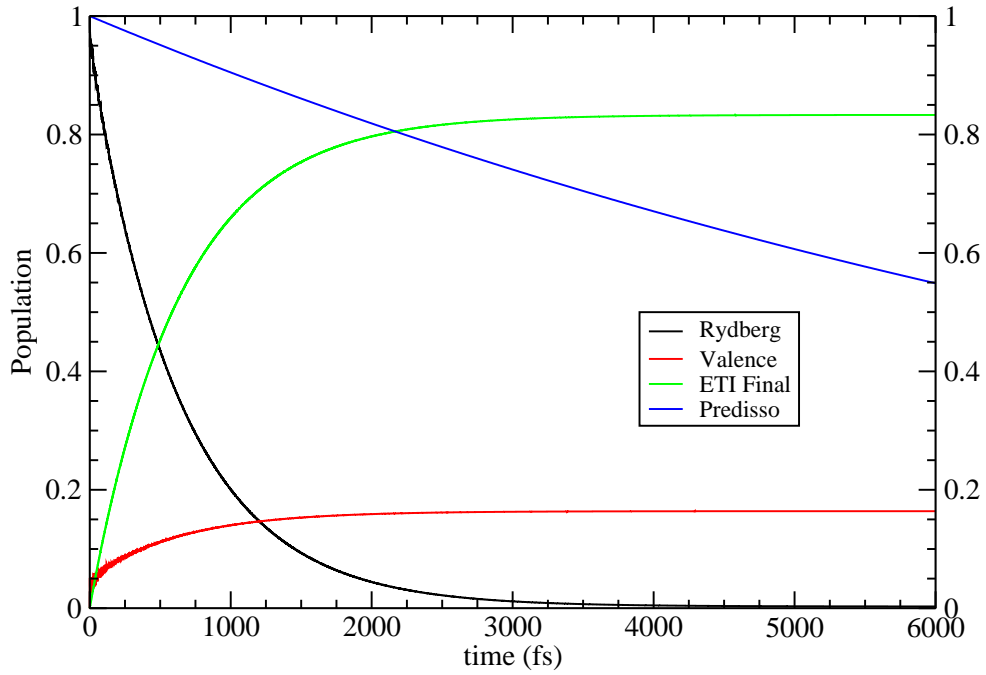
$$
\begin{aligned}
\frac{d}{dt}\langle\chi_R(t)|\chi_R(t)\rangle &= \langle\chi_R(t)|\dot{\chi}_R(t)\rangle + \langle\dot{\chi}_R(t)|\chi_R(t)\rangle \\
&= \langle\chi_R(t)|(-i)(\hat{T} + V_R - i\Gamma_R/2)|\chi_R(t)\rangle \\
&\quad + \langle\tilde{\chi}_R(t)|i(\hat{T} + V_R + i\Gamma_R/2)|\chi_R(t)\rangle \\
&\quad + \langle\chi_R(t)|(-i)(W - ig(R)\Gamma_{RV}/2)|\chi_V(t)\rangle \\
&\quad + \langle\chi_V(t)|i(W + ig(R)\Gamma_{RV}/2)|\chi_R(t)\rangle \\
&= -\langle\chi_R(t)|\Gamma_R|\chi_R(t)\rangle - i\langle\chi_R(t)|W^\dagger|\chi_V(t)\rangle + i\langle\chi_V(t)|W|\chi_R(t)\rangle \\
&\quad - \langle\chi_R(t)|\Gamma_{RV}/2|\chi_V(t)\rangle - \langle\chi_V(t)|\Gamma_{RV}/2|\chi_R(t)\rangle \\
&= -\langle\tilde{\chi}_R(t)|\Gamma_R|\tilde{\chi}_R(t)\rangle + 2i\mathrm{Im}\langle\chi_R(t)|W|\chi_V(t)\rangle - g(R)\mathrm{Re}\langle\chi_R(t)|\Gamma_{RV}|\chi_V(t)\rangle
\end{aligned}
$$

(5.68)

101

The population of the Rydberg state $\langle\chi_R(t)|\chi_R(t)\rangle$ at time t is given by

$$\int_{t_0}^{t} dt'\big[-\langle\chi_R(t')|\Gamma_R|\chi_R(t')\rangle + 2i\mathrm{Im}\langle\tilde{\chi}_R(t')|W|\tilde{\chi}_V(t')\rangle$$

$$-g(R)\mathrm{Re}\langle\chi_R(t')|\Gamma_{RV}|\chi_V(t')\rangle\big] \tag{5.69}$$

The formula for the valence state is analog.

Figure 5.16: Changes in the population in time after an excitation into the third vibrational level ($\nu = 2$) of the $B^1\Sigma^+$ Rydberg state using the diabatic ICD widths given in Fig. 5.13. For comparison, the depopulation of the Rydberg state due to predissociation (in the absence of ICD) is depicted.

In order to estimate the decay through the ICD channel, the norm of the final state $|\chi(E,t)\rangle$ is required. It can be calculated from the integrated form of (5.55)

$$i\frac{d}{dt}[e^{i(\hat{H}+V_0+E)t}|\chi(E,t)\rangle] = e^{i(\hat{H}+V_0+E)t}[\Lambda_R|\chi_R(t)\rangle + \Lambda_V|\chi_V(t)\rangle] \tag{5.70}$$

$$\Leftrightarrow e^{i(\hat{H}+V_0+E)t}|\chi(t)\rangle = -i\int e^{i(\hat{H}+V_0+E)t'}[\Lambda_R|\chi_R(t')\rangle + \Lambda_V|\chi_V(t')\rangle]dt'. \tag{5.71}$$

Now, the norm can be expressed by

$$\int \langle \chi(E,t)|\chi(E,t)\rangle dE = \int dE \int dt' \int dt'' [\langle \chi_R(t)|\Lambda_R^\dagger + \langle \chi_V(t)|\Lambda_V^\dagger]$$
$$\times e^{-i(\hat{H}+V_0+E)t'} e^{i(\hat{H}+V_0+E)t''} [\Lambda_R|\chi_R(t'')\rangle + \Lambda_V|\chi_V(t'')\rangle]. \qquad (5.72)$$

Because $\langle \chi(E,t)|\chi(E,t)\rangle = 0$ if $E < 0$ the integration limits can be changed

$$\int_0^\infty dE \to \int_{-\infty}^\infty dE \qquad (5.73)$$

and, thus, apply the well known relation

$$\int_{-\infty}^\infty dE e^{i(\hat{H}+V_0+E)(t''-t')} = 2\pi\delta(t''-t'). \qquad (5.74)$$

Now, we can simplify (5.72) to

$$\int \langle \chi(t,E)|\chi(t,E)\rangle dE = 2\pi \int_0^t dt' [\langle \chi_R(t')|\Lambda_R^\dagger \Lambda_R|\chi_R(t')\rangle \qquad (5.75)$$
$$+ \langle \chi_V(t')|\Lambda_V^\dagger \Lambda_V|\chi_V(t')\rangle + \langle \chi_R(t')|\Lambda_R^\dagger \Lambda_V|\chi_V(t')\rangle + \langle \chi_V(t')|\Lambda_V^\dagger \Lambda_R|\chi_R(t')\rangle].$$

For the evolution in time it follows

$$\frac{d}{dt} \int \langle \chi(E,t)|\chi(E,t)\rangle dE = \langle \chi_R(t)|\Gamma_R|\chi_R(t)\rangle$$
$$+ \langle \chi_V(t)|\Gamma_V|\chi_V(t)\rangle + 2g(R)\text{Re}\langle \chi_R(t)|\Gamma_{RV}|\chi_V(t)\rangle. \qquad (5.76)$$

The population at time t can be obtained by integrating to this point in time (see (5.69)).

Results: The Dynamics of CO in the Presence of Mg

It is assumed that CO·Mg is exposed to a broad band excitation energetically centered around the $X^1\Sigma^+(\nu = 0) \leftrightarrow B^1\Sigma^+(\nu = 0)$ transition. At room temperature virtually only the lowest vibrational level of the ground state of CO is populated and, hence, before the excitation, the wave packet is assumed to be in the lowest vibrational level of the ground state. The Franck-Condon factors of $X^1\Sigma^+(\nu = 0) \leftrightarrow B^1\Sigma^+(\nu = 0, 1, 2, 3)$ transitions are given in Tab. 2. Due to the excitation the nuclear wave packet is transferred from the ground state to the vibrational levels of the Rydberg state. We assume that the dynamics can be carried out in each vibrational level separately since the vibrational spacing is much larger than the widths of the vibrational levels. In order to get the total branching ratio, the results of the respective vibrational level must be weighted by the corresponding Franck-Condon factor. We employed two different models
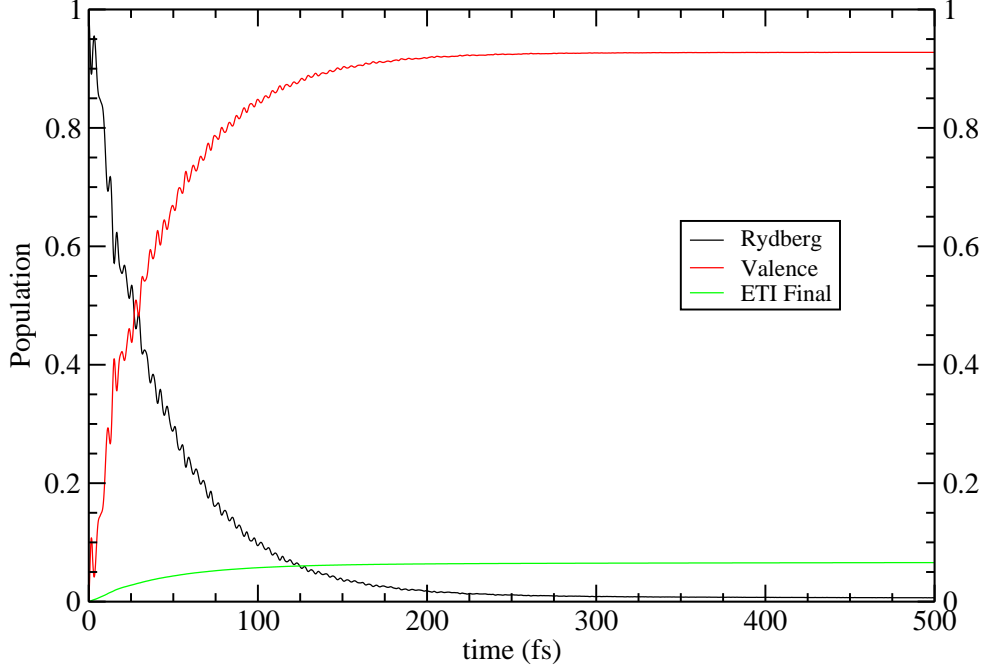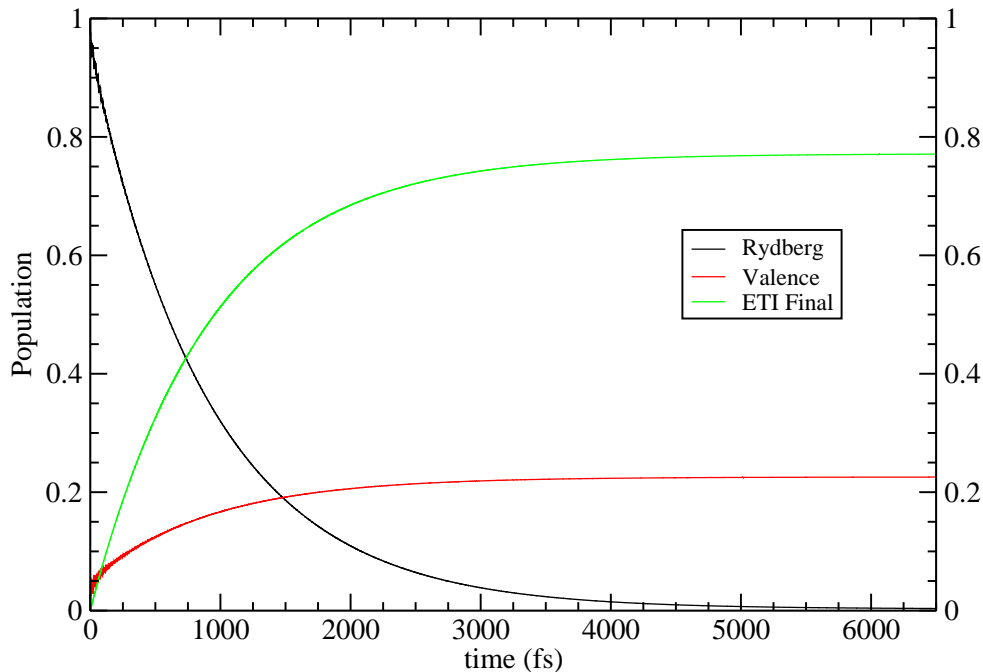
Figure 5.17: Changes in the population in time after an excitation into the fourth vibrational level ($\nu = 3$) of the $B^1\Sigma^+$ Rydberg state using the diabatic ICD widths given in Fig. 5.13.

for the diabatic ICD widths. The optimal one given in Fig. 5.13. The dynamics carried out using this model are supposed to approximate the true ones. The second model is the one where both diabatic widths are constants. Its purpose is to elucidate the impact of the imaginary off-diagonal term Γ_{RV} on the dynamics.

First, we employed the optimal model. In the subsequent calculations the imaginary off-diagonal coupling had been neglected since we suppose that its impact is really minor since it only occurs at one grid point (due to finite resolution of the grid). The evolution of the populations after an $X^1\Sigma^+(\nu = 0) \leftrightarrow B^1\Sigma^+(\nu = 0)$ excitation are depicted in Fig. 5.15. One can see that at the end of the dynamics, after 4 ps, 100% of the wave packet have been undergone ICD. The decay due to photon emission, which is depicted as well, can be neglected. Consequently, the fluorescence from the $B^1(\nu = 0)\Sigma^+$ level is quenched completely. The same applies to the second vibrational level ($\nu = 1$). Since the evolution of the populations in time is virtually equivalent to the evolution of the first level ($\nu = 0$), the corresponding evolution of the population is not depicted. The dynamics taking place after $X^1\Sigma^+(\nu = 0) \leftrightarrow B^1\Sigma^+(\nu = 2)$ excitations are of particular interest because in this vibrational level CO undergoes predissociation. The evolution
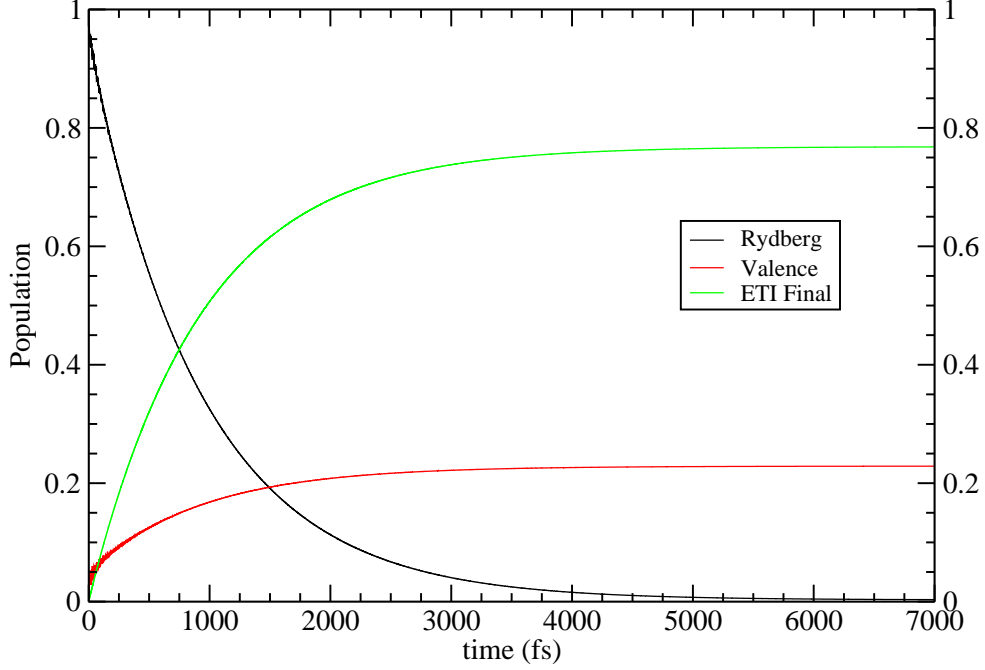
Figure 5.18: Changes in the population in time after an excitation into the third vibrational level ($\nu = 2$) of the $B^1\Sigma^+$ Rydberg state using the model of constant diabatic widths. The imaginary off-diagonal term has been neglected.

of the populations in time are shown in Fig. 5.16. As one can see there, the dynamics are complete after ca 4 ps. At that point in time, 84% of the wave packet have been decayed due to ICD. The remaining 16% of the wave packet go into the dissociation channel. That is, the photoinduced dissociation is strongly suppressed by the ICD. The dynamics following $X^1\Sigma^+(\nu = 0) \leftrightarrow B^1\Sigma^+(\nu = 3)$ excitations are depicted in Fig. 5.17. The dynamics are complete after ca 300 fs. In this level the dissociation is roughly 20 times more efficient than the ICD and, thus, the ICD has only very little time to absorb parts of the quickly outrunning wave packet. As a result, 8% of the wave packet undergo ICD and 92% of it end up in the dissociation channel.

In order to investigate the impact of the imaginary coupling term Γ_{RV} on the branching ratio we carried out the nuclear dynamics in the third vibrational level ($\nu = 2$), at first, neglecting the term and, after that, taking it into account. In the calculations we used the model of constant diabatic widths. In the first calculations, whose results are depicted in Fig. 5.18, the dynamics are completed after 6 ps. At that point in time, $77,0\%$ of the wave packet have undergone ICD.

Figure 5.19: Changes in the population in time after an excitation into the third vibrational level ($\nu = 2$) of the $B^1\Sigma^+$ Rydberg state using the model of constant diabatic widths. The imaginary off-diagonal term has been included.

$23,0\%$ of the packet are absorbed by the CAP. The corresponding results of the dynamics where Γ_{RV} has taken into account are depicted in Fig. 5.19. As in the first calculation, the dynamics are complete after 6 ps. But in this case $23,2\%$ of the wave packet undergo ICD and $76,8\%$ go into the dissociation channel. That means that the influence of Γ_{RV} is minor in the present case. In the case of overlapping resonances with large widths the region where the term occurs would be larger and, thus, the impact could be more important. However, in the problems considered in this work, it is well justified to neglect it.

The preceding calculations already show that ICD caused by one neighboring atom can be used to quench photoinduced nuclear dynamics. A very important aspect of ICD is that it becomes more efficient as the number of ICD-capable neighbors grows [16, 25, 50]. In order to study this effect, Mg is replaced by Mg_2. The geometry of the system is depicted in Fig. 5.20. As in the case of CO·Mg, we fixed the Mg_2 cluster with respect to the center of mass of CO. We calculated the ICD widths of the first excited adiabatic state at several internuclear distances between C and O. From the results we constructed the diabatic
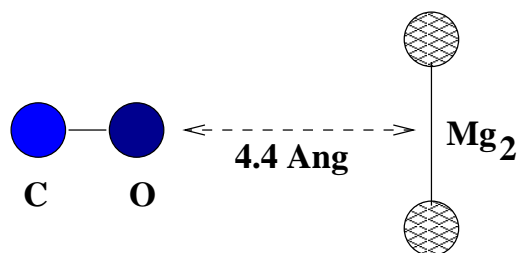
Figure 5.20: Schematic illustration of the geometry of the CO·Mg$_2$ cluster.

widths in Fig. 5.13 by the procedure described above in the case of CO·Mg. Using these widths and the PECs and couplings of the RKR model, we carried out the dynamics in the third vibrational level ($\nu = 2$). The corresponding results are depicted in Fig. 5.21. As one can see there, the dynamics are complete after ca 2.5 ps. At that point in time, 90% of the wave have undergone ICD. Only 10% of the packet have gone into the dissociation channel. Hence, by adding another Mg atom we were able to quench 6% of the wave packet additionally.
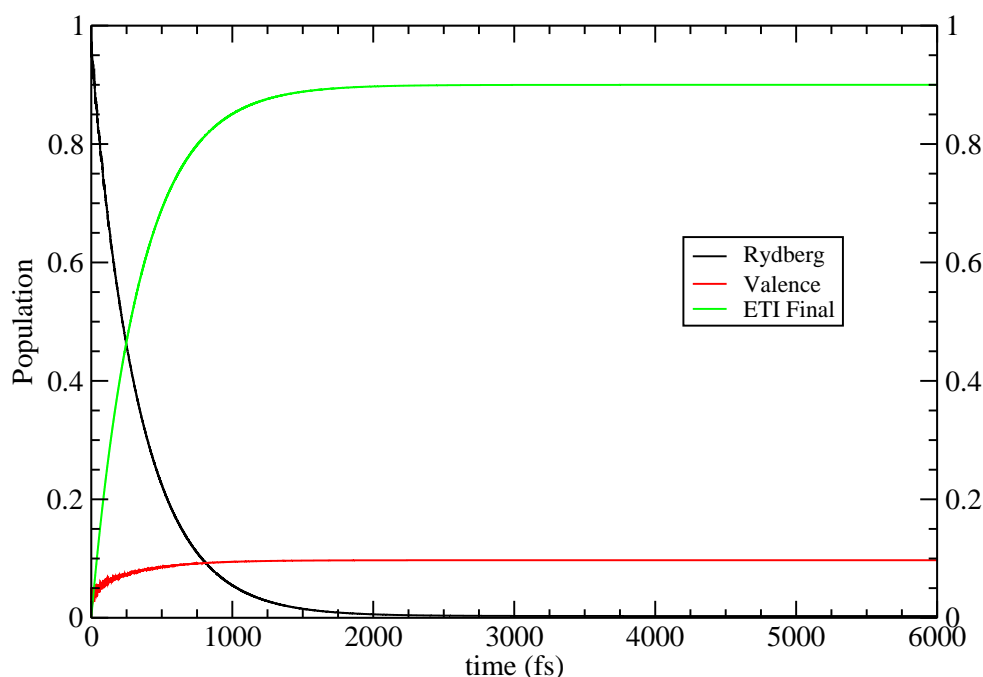
Figure 5.21: Changes in the population in time after an excitation into the third vibrational level ($\nu = 2$) of the CO$^*B^1\Sigma^+$ Rydberg state in CO·Mg$_2$.

Resonant Interatomic Coulombic Decay (RICD)

In this section we apply the FSL method to calculations of RICD widths. In particular, we determine the RICD widths of Ne$2s^{-1}3p$ excitations in NeMg. The corresponding widths have been calculated previously and, consequently, the following calculations should be regarded as a test of the method in the case of inner-valence excitations. The results of this section have been published in Ref. [25].

The interatomic decay following an inner-valence excitation of a cluster subunit is referred to as RICD [7,18]. After the excitation the inner-valence vacancy is filled by an outer-valence electron of the same subunit (spectator RICD or sRICD) or by the electron promoted to the virtual orbital in the excitation step (participator RICD or pRICD), while the excess energy is used to ionized a neighboring cluster subunit [18]. A schematic illustration of both processes is given in Fig. 1.1. The energy absorbed in exciting an inner-valence electron in an atom or molecule usually exceeds the first ionization potential. Hence, inner-valence excitations can decay by AI too. Consequently, RICD and AI compete with each other. This stresses the importance of the accurate knowledge of both widths.

6.1 Applications

Calculations of RICD widths in NeMg clusters

Here we apply our approach to the calculation of RICD widths in NeMg clusters following the $2s^{-1}3p$ excitation in Ne. The RICD widths of this system have been previously obtained by the Wigner-Weisskopf approach [18] and, moreover, all properties of the constituent atoms which are required to evaluate asymptotic formulae are known, thus, giving us the opportunity for independent assessment of the Fano-Stieltjes-Lanczos widths at large distances. As a first step we define the configuration subspaces for the initial and the final states of the decay. The electron configuration of the ground state of Ne is $(\text{He})2s^22p^6$. To describe the $2s^{-1}3p$ initial state, we include all 1h1p configurations with the hole in the Ne $2s$ orbital and, to account for some electron correlation, all 2h2p configurations with two holes in the $2s2p$ shell. The subspace of the final states of the decay differs depending whether one considers pRICD, sRICD, or autoionization. The definition of the subspace of the final states of the decay in the case of autoionization has been described in Ref. [25].

In the case of pRICD the final states of the system consist of Ne in its ground state and the Mg atom in a variety of ionized states. The energy of the initial

excitation is sufficient to produce the ground and excited states of Mg^+ as well as the ground state of Mg^{++}. Therefore, we take a final state subspace comprising all 1h1p and 2h2p configurations with holes in the Mg 3s orbital. The initial state couples in first order to the final states of 1h1p character, while it couples to the final states of 2h2p character only in second order, not accounted for by the ADC(2)x scheme. Usually these second order effects are small and we assume that they will not affect our results by much.

In the case of sRICD the final states of the system consist of Ne in an excited $2p^{-1}3p$ state and the Mg atom in the same ionized states as in the pRICD case. Consequently, in this case the configuration subspace of the final states comprise all 2h2p configurations with one vacancy in a Ne 2p orbital and one in the Mg 3s orbital. To describe the shake-up and doubly ionized states of Mg following sRICD we would need 3h3p configurations. These configurations are not available in the ADC(2) scheme and appear for the first time in the ADC(4) scheme. However, the coupling to these states is of second order and is usually smaller than the first order coupling to the 2h2p states given above.

We have shown above how the starting block of the Lanczos procedure should be selected in case the final states are predominantly of 1h1p character. Thus, to calculate the widths of pRICD process we have chosen the subspace spanned by all 1h1p configurations as the starting block. In the case of sRICD the final states of the decay are of 2h2p character. The size of the subspace spanned by these configurations is usually extremely large. We thus used the 100 2h2p configurations with one vacancy in the Mg 3s and one in a Ne 2p orbital which have the largest coupling to the initial state.

As a first test, we calculated the sRICD width of the Ne $2s^{-1}3p$ ($^1\Pi$) initial state as a function of the interatomic distance for different numbers of block Lanczos iterations (see Fig. 6.1). The calculations were carried out with an aug-cc-pCVTZ basis augmented with 12s, 8p, 6d Rydberg-like Gaussians centered on Ne and an aug-cc-pVTZ basis set augmented with 6s, 8p, 6d continuum-like Gaussians centered on Mg. To improve the description of the final 2h2p states we performed all calculations using the ADC(2)x scheme, which gives these states to first order in perturbation theory. The obtained energy of the Ne $2s^{-1}3p$ decaying state is 45.65 eV at large interatomic distances, in good agreement with the literature value of 45.54 eV [123] for the isolated Ne. The resulting dimension of the final 2h2p subspace is 28000. After five and ten block Lanczos iterations the decay width oscillates with R, becoming smooth after 30 or more block Lanczos iterations. For 60 and more iterations the width is converged at large interatomic distances but still increases slightly at interatomic distances where the orbital overlap is significant. Due to the observed slow convergence we tried to increase the size of the starting block, however, the convergence is not significantly improved by this.

We can offer two main reasons for the slow convergence at such interatomic
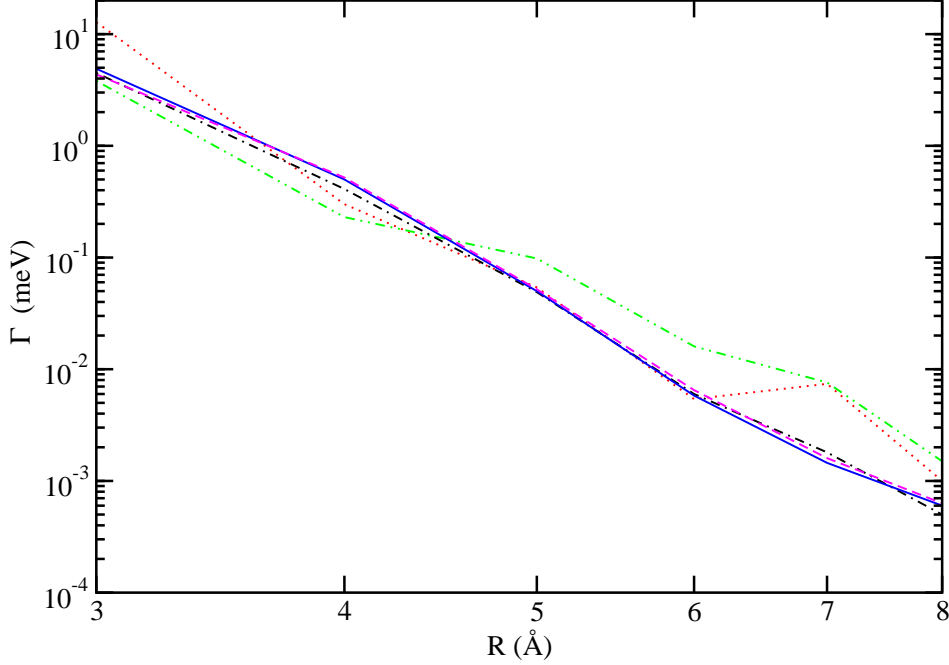
Figure 6.1: Spectator RICD width of $\text{Ne}2s^{-1}3p$ ($^1\Pi$) excited states in NeMg as a function of the interatomic distance for several numbers of block Lanczos iterations. The widths are shown after 5 (dotted line), 10 (dash-double-dotted line), 30 (dash-dotted line), 60 (dashed line), and 100 (full line) block Lanczos iterations with a block size of 100.

distances. Firstly, there is a large number of final states of 2h2p character contributing to a comparable degree to the decay width, thus, requiring many iterations to produce them. Secondly, since electron correlation is large among the final states of 2h2p character, many iterations are again needed to describe them accurately. Consequently, at interatomic distances close to the equilibrium geometry, the widths obtained employing a number of Lanczos states much smaller than the subspace dimension are expected to be underestimated compared with widths obtained by full diagonalization. To estimate the error introduced by the incomplete description of the P subspace we recalculated the sRICD width at equilibrium geometry by fully diagonalizing the corresponding $P\hat{H}P$ matrix. We obtained a value of 0.3 meV, exceeding the Fano-Stieltjes-Lanczos result by a factor of 1.7. It seems that a choice of starting block based on the coupling to the initial state is not completely sufficient and more sophisticated procedures ought to be worked out for cases involving doubly excited final states. Alternatively, other methods such as filter diagonalization [185–188] may be considered in cases

where Fano-Stieltjes-Lanczos underperforms.
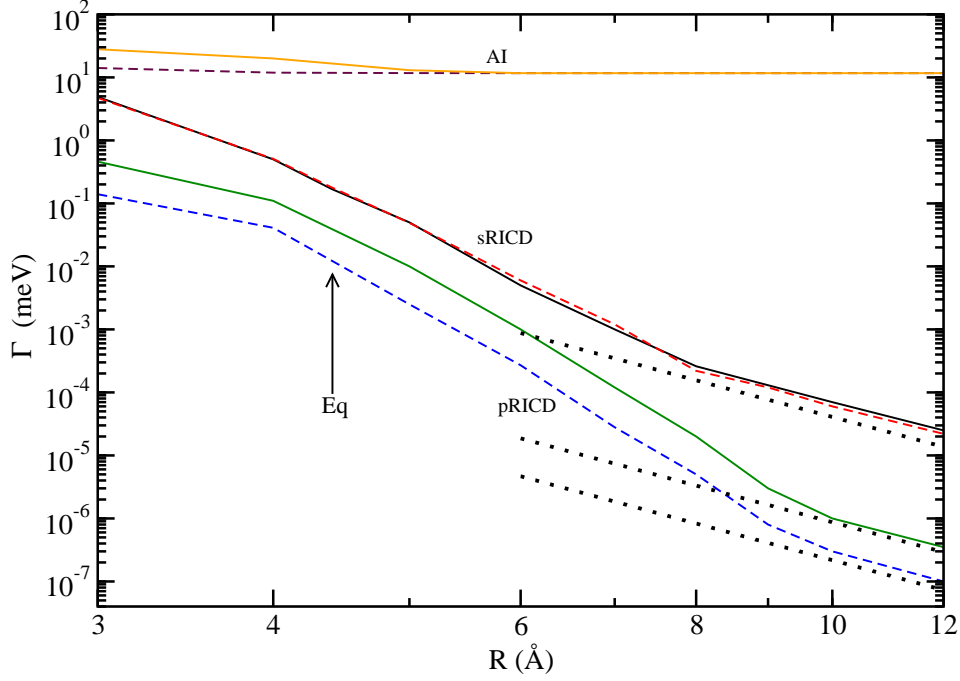
Figure 6.2: Decay widths of different electronic decay processes following Ne $2s^{-1}3p$ ($^1\Pi$) and $2s^{-1}3p$ ($^1\Sigma$) excitations, respectively, in NeMg as a function of the interatomic distance. In the case of pRICD and autoionization (AI) the width converged using 40 block Lanczos iterations and a starting block size of 80. For the depicted sRICD widths we used a block size of 100 and 100 block Lanczos iterations. The widths of the excitations in Π symmetry the are depicted as dashed lines. The full lines correspond to the widths of the excitations of Σ symmetry. The dotted lines show the prediction of the corresponding asymptotic formula. Note that the ionization cross section of Mg is low explaining the small interatomic widths. The radiative width of the initial state which is required to evaluate the asymptotic formula for the sRICD case was taken from Ref. [189].

Next, we calculated the decay widths for the following electronic decay pathways of the Ne $2s^{-1}3p$ $^1\Sigma$ and $^1\Pi$ initial states (see Fig.6.2): autoionization , sRICD, and pRICD. The autoionization width of the $2s^{-1}3p$ resonance in isolated Ne obtained by the Fano-Stieltjes-Lanczos method is 11.68 meV [25]. To compare it with the interatomic decay widths we calculated the autoionization widths of the Ne $2s^{-1}3p$ $^1\Sigma$ and $^1\Pi$ in the presence of Mg. To this end we employ the scheme described in Ref. [25] where the P subspace comprises 80 1h1p and 40000 2h2p configurations. To calculate the width with the block Lanczos method we use all 80 1h1p configurations as the starting block. About 40 block-Lanczos iterations resulting in 3200 final states were needed to converge the width. The autoion-

ization width of the Ne $2s^{-1}3p$ ($^1\Pi$) excitation remains virtually constant as a function of the interatomic distance. A small enhancement of the Ne $2s^{-1}3p$ ($^1\Sigma$) width is visible at interatomic distances below 6 Å. We have explained this enhancement previously [18] as arising due to the orbital overlap more pronounced in the state of $^1\Sigma$ symmetry. The values obtained are in good agreement with the autoionization width of the isolated Ne [25] and better than the values obtained with the less precise Wigner-Weisskopf method [18], which are three times smaller.

In the case of pRICD the subspace of the 1h1p final states comprises 80 1h1p configurations and 35000 2h2p configurations; the decay rate converged after 40 block Lanczos iterations with a starting block composed of all 80 1h1p configurations. The pRICD width of Ne $2s^{-1}3p$ ($^1\Pi$) and Ne $2s^{-1}3p$ ($^1\Sigma$) at large interatomic distances fall off as R^{-6} and differ roughly by a factor of four, in good agreement with the predictions of the virtual photon transfer model [21]. At interatomic distances smaller than 9 Å the $^1\Pi$ and the $^1\Sigma$ widths increase - compared to the values predicted by the asymptotic formulae - due to orbital overlap, whereas their ratio remains roughly four. At the equilibrium distance (4.4 Å) the Ne $2s^{-1}3p$ ($^1\Pi$) and the Ne $2s^{-1}3p$ ($^1\Sigma$) resonances have a width of 0.012 meV and 0.037 meV, respectively. Thus, they are roughly 4 and 13, respectively, times smaller than the corresponding sRICD width and two orders of magnitude larger than the corresponding values obtained with the Wigner-Weisskopf method [18]. The significant difference can be explained by the fact that the description of the virtual orbitals of the initial and the final states are significantly improved in Fano-Stietljes-Lanczos calculations.

The sRICD widths of the $2s^{-1}3p$ ($^1\Pi$) and the $2s^{-1}3p$ ($^1\Sigma$) states are virtually equal. This is because the excited electron, which determines the symmetry of the initial state, is not directly involved in the decay process [18]. At large interatomic distances both widths are proportional to R^{-6} and in good agreement with the predictions of the virtual photon transfer model. At interatomic distances smaller than 8 Å both widths increase due to orbital overlap. At the equilibrium distance of 4.4 Å both width are at 0.16 meV and, therefore, roughly 70 times smaller than the autoionization width and 8 times smaller than the sRICD width obtained by the Wigner-Weisskopf method [18]. However, we would not like to draw definitive conclusions from the comparison between the Wigner-Weisskopf and the present Fano-Stieltjes-Lanczos sRICD widths, since the latter are not converged with the number of Lanczos states.

Conclusion

The impact of ICD on photoinduced dynamics has been studied. In particular, we considered the photoinduced dynamics in the four lowest vibrational levels of the $B^1\Sigma^+$ Rydberg state of CO in CO·Mg. In isolated CO the two lowest vibrational level of the $B^1\Sigma^+$ Rydberg state decay within 30 ns by photon emission. The third and the fourth vibrational level undergo predissociation within a few ps. The predissociation in the $B^1\Sigma^+$ Rydberg state is caused by non-adiabatic interactions with the repulsive $D^1\Sigma^+$ valence state. Because Mg is only weakly bound to CO, both states are affected only insignificantly by its presence. However, since at internuclear distances between C and O smaller than 1.4 Å their excitation energy is sufficient to ionize 3s electrons from Mg, whose ionization potential amounts to 7.67 eV, both states can decay by ICD additionally. In the presence of Mg, consequently, the evolution in these states is governed by the competition between the dynamics taking place in isolated CO and that of ICD. In order to investigate the evolution of the states in the presence of Mg, working equations have been derived which depend on the PECs of the $B^1\Sigma^+$ Rydberg state and the $D^1\Sigma^+$ valence state, their coupling, and their ICD widths.

The results of the calculation of the nuclear dynamics show that ICD changes the evolution of the system. In the two lowest vibrational levels, the radiative decay is quenched completely. Instead, the states decay via ICD within less than 4 ps. In the third vibrational level, which is of particular interest since it undergoes predissociation within a few ps in isolated CO, the ICD suppresses the predissociation significantly: in CO·Mg 84% of the nuclear wavepacket undergo ICD and only 16% dissociate. Therefore, ICD can be used to quench relaxations due to nuclear rearrangements. In the fourth vibrational level of the $B^1\Sigma^+$ state in CO·Mg the relaxation due to predissociation proceeds roughly 20 times faster (the corresponding lifetime is 60 fs) than the decay due to ICD. In this level predissociation remains the predominant decay mode. 8% of the nuclear wave packet undergo ICD. Additionally, we investigated the dynamics of CO in the third vibrational level of the $B^1\Sigma^+$ Rydberg state in CO·Mg$_2$. In this system the decay due to ICD is twice as efficient. The larger ICD widths lead to an even stronger suppression of the predissociation: 90% of the nuclear wavepacket undergo ICD.

The quenching mechanism found in the course of the study of the dynamics of CO in CO·Mg is not restricted to fluorescence and predissociation, in fact, it is a general one: in the presence of environments which are weakly bound to a poly-atomic system, the nuclear rearrangements taking place in electronic

excited states of the system proceed in good approximation as in the isolated system. However, if the ionization potential of the environment is lower than the excitation energy, the ICD channel opens. Then the evolution of the system is governed by the competition between ICD and the relaxation due to nuclear rearrangements. Usually, the dynamics are significantly affected because ICD is normally very efficient.

In order to study the competition between ICD and relaxations due to nuclear rearrangements, it is necessary to know the ICD widths. To this end, we have introduced and implemented an efficient and simultaneously accurate method in this work which is adapted to the calculations of ICD widths of neutral excited states. The proposed method combines the Fano formalism and Stieltjes imaging with the Lanczos method. The method is applicable to all problems where the subspaces of the initial and final states of the ICD process can be defined in a physically meaningful way. The accuracy of the method is based on the application of many-body methods accounting for electron correlation in the determination of the initial states, final states of the decay and the coupling between them. The efficiency of the proposed method stems from the application of the block-Lanczos method. In the framework of the standard Stieltjes approach, used to reconstruct a continuous function $\Gamma(E)$ from the underlying $\mathcal{L}^2$ pseudo-spectrum, the pseudo-spectrum is obtained by a full diagonalization of the corresponding Hamiltonian matrix. By representing the Hamiltonian matrix by its Lanczos approximation the full diagonalization is bypassed. The results obtained for the final states of predominantly 1h1p character converge fast with the number of block-Lanczos iterations. A suitable choice for the starting block is given by configurations with the largest coupling to the initial state. The efficiency allows one to determine ICD widths of cluster consisting of poly-atomic systems. In the case of final states of 2h2p character, e.g. following sRICD, the convergence with the number of block-Lanczos iterations is fast at asymptotic distances, while it becomes slow at around the equilibrium geometry. This is explained by the large number of 2h2p configurations contributing comparably strong to the corresponding states.

We tested the proposed method by applying it to calculations of interatomic decay widths of outer-valence excited states in NeAr, HCN·Mg$_n$, $n = 1, 2$ and inner-valence excited states in NeMg. The accuracy of the obtained results is well documented by the quality of the decay widths at large interatomic distances where they are in good agreement to the predictions of the asymptotic formulae. In addition, in the case of HCN·Mg$_n$, $n = 1, 2$ we were able to compare the widths calculated by the present approach with widths obtained previously by the CAP-ADC method and the results are in good agreement. Having tested the method successfully, we subsequently utilized it to compute the ICD widths required to investigate the dynamics in CO·Mg. At the equilibrium geometry we found ICD widths of 0.6 meV and 1.3 meV for the Rydberg state in the case

of CO·Mg and CO·Mg$_2$, respectively. In the HCN·Mg$_n$ systems the respective widths are 1.8 meV and 16 meV, implying that ICD can very efficiently quench even fast processes in more favorite cases than CO·Mg$_n$. The latter systems have been studied because of the availability of all the required photodissociation data for isolated CO.

Chapter 7

Acknowledgment

At this point I would like to wholeheartedly thank Lenz for supporting and advising me during the past years.

Moreover, I thank Kirill, Siggi, Stefan, Evgenij, Jochen, Vitali, Letitia, Tsveta, and Michi (arbitrary order :) for helping me with my thesis and beyond.

I would like to thank Prof. Surzhykov for examining my thesis
and Prof. Weidemüller as well as Prof. Hausmann for participating in my oral examination.

Finally and especially, I would like to say thank you to my parents and Eli.

Diabatization through Block Diagonalization

The method originates from the Hamiltonian (5.7) represented in an initial basis $|\phi_i\rangle$ (,e.g., in MOs)

$$\underline{\mathbf{H}} = \langle \phi_i | \hat{H} | \phi_j \rangle. \tag{A.1}$$

We are looking for a transformation that block diagonalizes $\underline{\mathbf{H}}$ such that the derivative couplings are minimized. Assume that $\underline{\mathbf{H}}$ is block diagonalized by the unitary matrix $\underline{\mathbf{T}}$

$$\underline{\boldsymbol{\mathcal{H}}} = \underline{\mathbf{T}}^{\dagger} \underline{\mathbf{H}} \, \underline{\mathbf{T}}. \tag{A.2}$$

The connection between the initial basis and the adiabatic picture is provided by the unitary matrix $\underline{\mathbf{S}}$ defined by the following eigenproblem

$$\underline{\mathbf{H}} \, \underline{\mathbf{S}} = \underline{\mathbf{S}} \, \underline{\boldsymbol{\Lambda}}, \tag{A.3}$$

where the diagonal matrix $\underline{\boldsymbol{\Lambda}}$ contains the adiabatic eigenvalues and the elements of $\underline{\mathbf{S}}$ are of the form

$$S_{mn} = \langle \phi_m | \varphi_n \rangle, \tag{A.4}$$

where $|\varphi_n\rangle$ are the adiabatic eigenstates. By considering the expression

$$\underline{\boldsymbol{\mathcal{H}}} \, \underline{\mathbf{F}}^{\dagger} = \underline{\mathbf{F}}^{\dagger} \underline{\boldsymbol{\Delta}}, \tag{A.5}$$

where $\underline{\boldsymbol{\Delta}}$ is the corresponding (diabatic) eigenvalue matrix, we can easily find that

$$\underline{\mathbf{T}} = \underline{\mathbf{S}} \, \underline{\mathbf{F}}, \tag{A.6}$$

where $\underline{\mathbf{F}}$ is a unitary block diagonal matrix. This equation defines the most general transformation which block diagonalizes $\underline{\mathbf{H}}$: $\underline{\mathbf{S}}$ diagonalizes $\underline{\mathbf{H}}$ and the application of $\underline{\mathbf{F}}$ induces the block form.

Apart from being unitary the submatrices $\underline{\mathbf{F}}_{nn}$ of $\underline{\mathbf{F}}$ are arbitrary and a further condition is required to determine them uniquely. An appropriate constraint can be imposed by requiring that the transformation $\underline{\mathbf{T}}$ should bring $\underline{\mathbf{H}}$ into block diagonal form but, beyond this, it should change as little as possible [158]. Id est, the matrix $\underline{\mathbf{T}}$ should be as close as possible to the unit matrix and, consequently, one requires

$$\|\underline{\mathbf{T}} - \underline{\mathbf{1}}\| = \min. \tag{A.7}$$

Appendix **A**

One can show the the matrix $\underline{\mathbf{T}}$ which fulfills the desired constraints is of the form [158]

$$\underline{\mathbf{T}} = \underline{\mathbf{S}}\,\underline{\mathbf{S}}^{\dagger}_{BD}(\underline{\mathbf{S}}_{BD}\,\underline{\mathbf{S}}^{\dagger}_{BD})^{1/2} \equiv \underline{\mathbf{S}}\,\underline{\mathbf{F}}. \tag{A.8}$$

The block diagonal matrix $\underline{\mathbf{S}}_{BD}$ is known: it is a block diagonal choice of $\underline{\mathbf{S}}$:

$$\underline{\mathbf{S}}_{BD} = \begin{pmatrix} \underline{\mathbf{S}}_{11} & & & 0 \\ & \underline{\mathbf{S}}_{22} & & \\ & & \ddots & \\ 0 & & & \underline{\mathbf{S}}_{NN} \end{pmatrix}. \tag{A.9}$$

where N denotes the number of subsets or blocks, respectively. The choice of the block diagonal matrix $\underline{\mathbf{S}}_{BD}$ is essential because it determines the states which are represented diabatically. In practice, one is usually interested in one small subset of states α. To obtain the desired transformation one reorders $\underline{\mathbf{S}}$ until the desired block structure is achieved

$$\underline{\mathbf{S}}_P = \begin{pmatrix} S_{\alpha\alpha} & S_{\beta\alpha} \\ S_{\alpha\beta} & S_{\beta\beta} \end{pmatrix}. \tag{A.10}$$

The off-block elements S_{ba} should be small if the structure is chosen appropriately [190]. Due to this partitioning of the eigenvector matrix $\underline{\mathbf{S}}$, one is able to construct $\underline{\mathbf{T}}$ knowing the eigenvalues and eigenvectors belonging to subset α only. Since the subset is usually small the method is usually cheap.

That the proposed block diagonalization of the electronic part of the Hamiltonian leads to a minimalization of the couplings due to $\hat{T}_N$ if the initial basis and the subset α are chosen appropriately has been shown in Ref. [191].

Bibliography

[1] A. Temkin, *Autoionization*, Plenum, New York, 1985.

[2] P. Auger, J. Phys. Radium **6**, 205 (1925).

[3] L. S. Cederbaum, J. Zobeley, and F. Tarantelli, Phys. Rev. Lett. **79**, 4778 (1997).

[4] S. Marburger, O. Kugeler, U. Hergenhahn, and T. Möller, Phys. Rev. Lett. **90**, 203401 (2003).

[5] T. Jahnke, A. Czasch, M. S. Schöffler, S. Schössler, A. Knapp, M. Käsz, J. Titze, C. Wimmer, K. Kreidi, R. E. Grisenti, A. Staudte, O. Jagutzki, U. Hergenhahn, H. Schmidt-Böcking, and R. Dörner, Phys. Rev. Lett. **93**, 163401 (2004).

[6] G. Öhrwall, M. Tchaplyguine, M. Lundwall, R. Feifel, H. Bergersen, T. Rander, A. Lindblad, S. P. J. Schulz, S. Barth, S. Marburger, U. Hergenhahn, S. Svensson, and O. Björneholm, Phys. Rev. Lett. **93**, 173401 (2004).

[7] S. Barth, S. Joshi, S. Marburger, V. Ulrich, A. Lindblad, G. Öhrwall, O. Björneholm, and U. Hergenhahn, J. Chem. Phys. **122**, 241102 (2005).

[8] T. Aoto, K. Ito, Y. Hikosaka, E. Shigemasa, F. Penent, and P. Lablanquie, Phys. Rev. Lett. **97**, 243401 (2006).

[9] Y. Morishita, X.-J. Liu, N. Saito, T. Lischke, M. Kato, G. Prümper, M. Oura, H. Yamaoka, Y. Tamenori, and I. H. S. K. Ueda, Phys. Rev. Lett. **96**, 243402 (2006).

[10] T. Jahnke, A. Czasch, M. Schöffler, S. Schössler, M. Käsz, J. Titze, K. Kreidi, R. E. Grisenti, A. Staudte, O. Jagutzki, L. Schmidt, T. Weber, H. Schmidt-Böcking, K. Ueda, and R. Dörner, Phys. Rev. Lett. **99**, 153401 (2007).

[11] T. Jahnke, H. Sann, T. Havermeier, K. Kreidi, C. Stuck, M. Meckel, M. Schöffler, N. Neumann, R. Wallauer, S. Voss, A. Czasch, O. Jagutzki, A. Malakzadeh, F. Afaneh, T. Weber, H. Schmidt-Böcking, and R. Dörner, Nature Physics **6**, 139 (2010).

[12] M. Mucke, M. Braune, S. Barth, M. Förstel, T. Lischke, V. Ulrich, T. Arion, U. Becker, A. Bradshaw, and U. Hergenhahn, Nature Physics **6**, 143 (2010).

[13] R. Santra, J. Zobeley, L. S. Cederbaum, and N. Moiseyev, Phys. Rev. Lett. **85**, 4490 (2000).

[14] R. Santra, J. Zobeley, and L. S. Cederbaum, Phys. Rev. B **64**, 245104 (2001).

[15] R. Santra and L. S. Cederbaum, Phys. Rev. Lett. **90**, 153401 (2003).

[16] V. Averbukh, I. B. Müller, and L. S. Cederbaum, Phys. Rev. Lett. **93**, 263002 (2004).

[17] S. Scheit, V. Averbukh, H.-D. Meyer, N. Moiseyev, R. Santra, T. Sommerfeld, J. Zobeley, and L. S. Cederbaum, J. Chem. Phys. **121**, 8393 (2004).

[18] K. Gokhberg, V. Averbukh, and L. S. Cederbaum, J. Chem. Phys. **124**, 144315 (2006).

[19] K. Gokhberg, A. B. Trofimov, T. Sommerfeld, and L. S. Cederbaum, Europhys. Lett. **72**, 228 (2005).

[20] A. I. Kuleff and L. S. Cederbaum, Phys. Rev. Lett. **98**, 083201 (2007).

[21] K. Gokhberg, S. Kopelke, N. V. Kryzhevoi, P. Kolorenč, and L. S. Cederbaum, Phys. Rev. A **81**, 013417 (2010).

[22] N. Sisourat, N. V. Kryzhevoi, P. Kolorenč, S. Scheit, T. Jahnke, and L. S. Cederbaum, Nature Physics **6**, 508 (2010).

[23] S. Kopelke, K. Gokhberg, L. S. Cederbaum, and V. Averbukh, J. Chem. Phys. **130**, 144103 (2009).

[24] A. Kuleff, S. Kopelke, K. Gokhberg, and L. Cederbaum, Phys. Rev. Lett. **105**, 043004 (2010).

[25] S. Kopelke, K. Gokhberg, L. S. Cederbaum, F. Tarantelli, and V. Averbukh, J. Chem. Phys. **134**, 024106 (2011).

[26] R. Schinke, *Photodissociation Dynamics*, Cambridge University Press, Cambridge, 1993.

[27] J. Z. H. Zhang, *Theory and Applications of Quantum Molecular Dynamics*, World Scientific, New York, 1999.

[28] D. J. Tannor, *Introduction to Quantum Mechanics - A Time-Dependent Perspective*, University Science Books, Sausalito, 2007.

[29] W.-U. Tchang-Brillet, P. Julienne, J.-M. Robbe, C. Letzelter, and F. Rostas, J. Chem. Phys. **96**, 6735 (1992).

[30] M. Eidelsberg, J.-Y. Roncin, A. L. Floch, F. Launay, C. Letzelter, and J. Rostas, J. Mol. Spectrosc. **121**, 309 (1987).

[31] M. Eidelsberg and F. Rostas, Astron. Astrophys. **235**, 474 (1970).

[32] J. Baker, W.-U. Tchang-Brillet, and P. Julienne, J. Chem. Phys. **102**, 3956 (1995).

[33] L. S. Cederbaum and F. Tarantelli, J. Chem. Phys. **98**, 9691 (1993).

[34] E. Pahl, H.-D. Meyer, and L. S. Cederbaum, Z. Phys. D **38**, 215 (1996).

[35] S. Scheit, L. S. Cederbaum, and H.-D. Meyer, J. Chem. Phys. **118**, 2092 (2003).

[36] P. Kolorenč, N. V. Kryzhevoi, N. Sisourat, and L. S. Cederbaum, Phys. Rev. A **82**, 013422 (2010).

[37] U. V. Riss and H.-D. Meyer, Phys. Rev. B **26**, 4593 (1993).

[38] U. V. Riss and H.-D. Meyer, Phys. Rev. B **31**, 2279 (1998).

[39] J. G. Muga, J. P. Paloa, B. Navarro, and I. L. Egusquiza, Phys. Rep. **395**, 357 (2004).

[40] N. Vaval and L. S. Cederbaum, J. Chem. Phys. **126**, 164110 (2007).

[41] S. Feuerbach, T. Sommerfeld, R. Santra, and L. S. Cederbaum, J. Chem. Phys. **118**, 6188 (2003).

[42] Y. Sajeev, R. Santra, and S. Pal, J. Chem. Phys. **123**, 204110 (2005).

[43] T. Sommerfeld, U. V. Riss, H.-D. Meyer, L. S. Cederbaum, B. Engels, and H. U. Suter, Phys. Rev. B **31**, 4107 (1998).

[44] R. Santra, L. S. Cederbaum, and H.-D. Meyer, Chem. Phys. Lett. **303**, 413 (1999).

[45] U. Fano, Phys. Rev. **124**, 1866 (1961).

[46] H. Feshbach, Ann. Phys. **5**, 357 (1958).

[47] G. Howat, T. Åberg, and O. Goscinski, J. Phys. B **11**, 1575 (1978).

[48] G. Howat, J. Phys. B **11**, 1589 (1978).

[49] J. J. Sakurai, *Modern Quantum Mechanics*, Addison-Wesley, Reading, MA, 1994.

[50] V. Averbukh and L. S. Cederbaum, Phys. Rev. Lett. **96**, 053401 (2006).

[51] V. Averbukh and L. S. Cederbaum, J. Chem. Phys. **123**, 204107 (2005).

[52] I. Cacelli, V. Caravetta, and R. Moccia, Mol. Phys. **59**, 385 (1986).

[53] P. W. Langhoff, Chem. Phys. Lett. **22**, 60 (1973).

[54] P. W. Langhoff, C. T. Corcoran, J. Sims, F. Weinhold, and R. M. Glover, Phys. Rev. A **14**, 1042 (1976).

[55] P. W. Langhoff, *Electron-Molecule and Photon-Molecule Collisions*, Plenum, New York, 1979.

[56] A. U. Hazi, *Electron-Molecule and Photon-Molecule Collisions*, Plenum, New York, 1979.

[57] A. U. Hazi, J. Phys. B **11** (1978).

[58] A. U. Hazi, A. E. Orel, and T. N. Rescigno, Phys. Rev. Lett. **46**, 918 (1981).

[59] B. L. Whitten and A. U. Hazi, Phys. Rev. A **33**, 1039 (1986).

[60] K. Gokhberg, V. Averbukh, and L. S. Cederbaum, J. Chem. Phys. **126**, 154107 (2007).

[61] R. K. Nesbet, Phys. Rev. A **14**, 1065 (1976).

[62] V. V. Ivanov and A. V. Luzano, J. Struct. Chem. **38**, 10 (1997).

[63] H. Ågren, V. Carravetta, H. Jensen, P. Jørgensen, and J. Olsen, Phys. Rev. A **47**, 3810 (1993).

[64] V. Carravetta, Y. Luo, and H. Ågren, Chem. Phys. **174**, 141 (1993).

[65] K. Gokhberg, V. Vysotskiy, L. S. Cederbaum, L. Storchi, F. Tarantelli, and V. Averbukh, J. Chem. Phys. **130**, 064104 (2009).

[66] B. N. Parlett, *The Symmetric Eigenvalue Problem*, Prentice-Hall, Englewood Cliffs, NJ, 1980.

[67] J. Schirmer, Phys. Rev. A **26**, 2395 (1982).

[68] F. Mertins and J. Schirmer, Phys. Rev. A **53**, 2140 (1996).

[69] C. A. Nicolaides and D. R. Beck, Int. Journal of Quant. Chem. **14**, 457 (1978).

[70] E. Balslev and J. M. Combes, Commun. Math. Phys. **22**, 280 (1971).

[71] W. P. Reinhardt, Ann. Rev. Phys. Chem. **33**, 223 (1982).

[72] N. Moiseyev, Phys. Rep. **302**, 211 (1998).

[73] Y. K. Ho, Phys. Rep. **99**, 1 (1983).

[74] J. Aguilar and J. M. Combes, Commun. Math. Phys. **22**, 269 (1972).

[75] B. Simon, Ann. Math. **97**, 247 (1973).

[76] U. Riss and H.-D. Meyer, J. Chem. Phys. **105**, 1409 (1996).

[77] U. Riss and H.-D. Meyer, J. Phys. B **31**, 2279 (1998).

[78] N. Moiseyev and U. Peskin, Phys. Rev. A **42**, 255 (1990).

[79] V. F. Weisskopf and E. P. Wigner, **63**, 54 (1930).

[80] R. Santra and L. S. Cederbaum, **368**, 1 (2002).

[81] H. Feshbach, Ann. Phys. **19**, 287 (1962).

[82] T. F. Malley, Phys. Rev. **150**, 14 (1966).

[83] J. N. Bardsley, J. Phys. B **1**, 349 (1968).

[84] F. H. Mies, Phys. Rev. **175**, 164 (1968).

[85] P. A. M. Dirac, Z. Physik **44**, 585 (1927).

[86] R. G. Newton, *Scattering Theory of Waves and Particles*, Springer, New York, 1982.

[87] A. Szabo and N. S. Ostlund, *Modern Quantum Chemistry: Introduction to Advanced Electronic Structure Theory*, Dover Publ., Mineola, New York, 1989.

[88] T. Helgaker, P. Jørgenssen, and J. Olsen, *Molecular Electronic-Structure Theory*, Wiley & Sons, Weinheim, 2000.

[89] E. Dalgaard and H. J. Monkhorst, Phys. Rev. A **28**, 1217 (1983).

[90] H. Koch and P. Jørgensen, J. Chem. Phys. **93**, 3333 (1990).

[91] H. Koch, H. Jensen, P. Jørgensen, and T. Helgaker, J. Chem. Phys. **93** (199).

[92] H. Sekino and R. J. Bartlett, Int. J. Quantum Chem. **18**, 255 (1984).

[93] J. Geertsen, M. Rittby, and R. J. Bartlett, Chem. Phys. Lett. **164**, 57 (1989).

[94] J. F. Stanton and R. J. Bartlett, Chem. Phys. **98**, 7029 (1993).

[95] K. Andersson, P.-A. Malmquist, R. Roos, A. Sadlej, and K. Wolinksi, J. Phys. Chem. **94**, 5483 (1990).

[96] K. Andersson, P.-A. Malmquist, and R. Roos, J. Chem. Phys. **96**, 1218 (1992).

[97] A. L. Fetter and J. D. Walecka, *Quantum Theory of Many-Particle Systems*, McGraw-Hill, 1971.

[98] J. Oddershede, Adv. Quantum Chem. **11**, 275 (1978).

[99] J. Oddershede, Adv. Chem. Phys. **69**, 201 (1987).

[100] J. Schirmer, Phys. Rev. A **43**, 4647 (1991).

[101] J. Schirmer, L. S. Cederbaum, and O. Walter, Phys. Rev. A **28**, 1237 (1983).

[102] J. Schirmer and A. Barth, Z. Phys. A **317**, 267 (1984).

[103] A. B. Trofimov, G. Stelter, and J. Schirmer, J. Chem. Phys. **111**, 9982 (1999).

[104] J. Schirmer and A. B. Trofimov, J. Chem. Phys. **120**, 11449 (2004).

[105] J. A. Shohat and J. D. Tamarkin, *The Problem of Moments*, American Mathemetical Society, New York, 1943.

[106] C. B. Lang and N. Pucker, *Mathematische Methoden in der Physik*, Spektrum Akademischer Verlag, Heidelberg, 1998.

[107] F. Müller-Plathe and G. Diercksen, *Electronic Structure of Atoms, Molecules and Solids*, World Scientific, Singapore, 1990.

[108] W. B. Jones and W. J. Thron, *Continued Fractions. Analytic Theory and Applications*, Addison-Wesley, Ontario, 1980.

[109] G. A. Baker, *Essentials of Padé Approximations*, Academic Press, Inc, New York, 1975.

[110] Fischer, *Lineare Algebra*, Springer, Heidelberg, 2002.

[111] C. Lanczos, J. Res. Nat Bur. Stand. **45**, 255 (1950).

[112] G. H. Golub and C. F. van Loan, *Matrix Computations*, The Johns Hopkins University Press, Baltimore, 1989.

[113] E. Pahl and H.-D. Meyer, J. Chem. Phys. **91**, 6195 (1989).

[114] H.-D. Meyer and S. Pal, J. Chem. Phys. **91**, 6195 (1989).

[115] F. Schwabl, *Quantenmechanik*, Springer, Heidelberg, 2002.

[116] I. I. Sobelman, *An Introduction to the Theory of Atomic Spectra*, Pergamon Press, Oxford, 1972.

[117] Hober and Wachter, *Repititorium Theoretische Physik*, Spektrum Akademischer Verlag, Heidelberg, 1998.

[118] 3j-symbol Calculator, `http://www.svengato.com/threej.html`.

[119] W. Demtröder, *Molekülphysik*, Oldenburg, München, 2003.

[120] J. W. Cooper, Rev. Mod. Phys. **128**, 681 (1962).

[121] A. Derevianko and W. R. Johnson, Atomic and Nuclear Data Tables **73**, 153 (1999).

[122] P. L. Stiles, D. T. Moore, and R. E. Miller, J. Chem. Phys. **121**, 3130 (2004).

[123] Y. Ralchenko, Kramida, A. E. R. J., and N. A. Team, Nist atomic spectra database, 2011.

[124] J. T. H. Dunning, J. Chem. Phys. **90**, 1007 (1989).

[125] K. Kaufmann, W. Baumeister, and M. Jungen, J. Phys. B **22**, 2223 (1989).

[126] W. E. Davidson, J. Comput. Phys. **17**, 97 (1975).

[127] M. TEAM, `http://www.molcas.org/documentation/manual`.

[128] R. D. Brado and K. Ruedenberg, J. Chem. Phys. **60**, 918 (1974).

[129] R. D. Brado and K. Ruedenberg, J. Chem. Phys. **60**, 932 (1974).

[130] A. Chutjan, H. Tanaka, B. Wicke, and S. Srivastava, J. Chem. Phys. **67**, 4835 (1977).

[131] M. Stener, G. D. Alti, G. Fronzoni, and P. Decleva, Chem. Phys. **222**, 197 (1997).

[132] G. Wang, J. Wan, and X. Zhou, J. Phys. B **43**, 035001 (2010).

[133] S. Barth, S. Marburger, S. Joshi, V. Ulrich, O. Kugeler, and U. Hergenhahn, Phys. Chem. Chem. Phys. **8**, 3218 (2006).

[134] M. Inoue, J. Chim. Phys. **63**, 1061 (1966).

[135] O. May, D. Kubala, and M. Allan, Phys. Rev. A **82**, 010701 (2010).

[136] H. N. Varambhia and J. Tennyson, J. Phys. B **40**, 1211 (2007).

[137] P. D. Burrow, A. E. Howard, and A. Johnston, J. Chem. Phys. **96**, 7570 (1992).

[138] F. Edard, A. P. Hitchcock, and M. Tronc, J. Phys. Chem. **94**, 2768 (1990).

[139] W. Domcke and L. S. Cederbaum, Phys. Rev. A **16**, 1465 (1977).

[140] T. J. Chuang, G. W. Hoffmann, and K. B. Eisenthal, Chem. Phys. Lett. **25**, 201 (1974).

[141] Z. Li, R. Zadoyan, V. A. Apkarian, and C. C. Martens, J. Phys. Chem. **99**, 7453 (1995).

[142] Q. Liu, J. K. Wang, and A. H. Zewail, Nature **364**, 427 (1993).

[143] C. Lienau and A. H. Zewail, J. Phys. Chem. **100**, 18629 (1996).

[144] G. Herzberg, *Molecular Spectra and Molecular Structure III*, Van Nostrand, New York, 1967.

[145] H. A. Jahn and E. Teller, Proc. Roy. Soc. **161**, 220 (1938).

[146] R. Renner, **92**, 172 (1934).

[147] J. Neumann and E. Wigner, Physik. Zeitschr. **30**, 467 (1929).

[148] L. D. Landau, Phys. Z. Sowjetunion **2**, 46 (1932).

[149] F. T. Smith, Phys. Rev. **179**, 111 (1969).

[150] W. Lichten, Phys. Rev. **164**, 131 (1967).

[151] C. Mead and D. Truhlar, J. Chem. Phys. **77**, 6090 (1982).

[152] M. Baer, Chem. Phys. Lett. **35**, 112 (1975).

[153] C. Petrongolo, R. Buenker, and S. Peyerimhoff, J. Chem. Phys. **78**, 7284 (1983).

[154] M. Desouter-Lecomte, D. Dehareng, and J. Lorquet, J. Chem. Phys. **86**, 1429 (1987).

[155] H.-J. Werner and W. Meyer, J. Chem. Phys. **74**, 5802 (1981).

[156] J. Hendeković, Chem. Phys. Lett. **90**, 193 (1982).

[157] I. Özkan and L. Goodman, Chem. Rev. **79**, 275 (1979).

[158] L. Cederbaum, J. Schirmer, and H.-D. Meyer, J. Phys. A **22**, 2427 (1989).

[159] C. Letzelter, M. Eidelsberger, J. Rostas, J. Breton, and B. Thieblemont, Chem. Phys. **114**, 273 (1987).

[160] J. Baker, Chem. Phys. Lett. **408**, 312 (2005).

[161] Y. Li, O. Bludsky, G. Hirsch, and R. Buenker, J. Chem. Phys. **107**, 3014 (1997).

[162] M. Monnerville and J. M. Robbbe, J. Chem. Phys. **101**, 7580 (1994).

[163] D. L. Cooper and K. Kirby, J. Chem. Phys. **87**, 424 (1987).

[164] H. Karlsson, Eur. Phys. J. D **11**, 207 (2000).

[165] M. Monnerville and J. M. Robbbe, Eur. Phys. J. D **5**, 381 (1999).

[166] Y. Li, R. Buenker, and G. Hirsch, Theor. Chem. Acc. **100**, 112 (1998).

[167] F. Busam, *Funktionentheorie I*, Springer, Heidelberg, 2003.

[168] N. Moiseyev, Phys. Rep. **302**, 211 (1998).

[169] H. O. Karlsson, J. Chem. Phys. **108**, 3849 (1998).

[170] A. Trofimov, *phd thesis*, 1994.

[171] Obtained via MP(2) calculation for the ground State using MOLCAS 7.4.

[172] J. Royal, A. Larson, and A. E. Orel, J. Phys. B **37**, 3075 (2004).

[173] A. U. Hazi, J. Phys. B **16** (1983).

[174] H. Estrada, L. S. Cederbaum, and W. Domcke, J. Chem. Phys. **84**, 152 (1986).

[175] S. Feuerbacher, T. Sommerfeld, and L. S. Cederbaum, J. Chem. Phys. **120**, 3201 (2004).

[176] M. Gell-Man and M. L. Goldberger, Phys. Rev. **91**, 398 (1953).

[177] A. U. Hazi, T. N. Rescigno, and M. Kurilla, Phys. Rev. A **23**, 1089 (1981).

[178] H.-D. Meyer, F. Gatti, and G. A. Worth, *Multidimensional Quantum Dynamics: MCTDH Theory and Applications*, WILEY-VCH, Weinheim, 2009.

[179] J. C. Light, I. P. Hamilton, and J. V. Lill, J. Chem. Phys. **82**, 1400 (1985).

[180] D. T. Colbert and W. H. Miller, J. Chem. Phys. **96**, 1982 (1992).

[181] W. T. Pollard and R. A. Friesner, J. Chem. Phys. **100**, 5054 (1994).

[182] T. J. Park and J. C. Light, J. Chem. Phys. **85**, 5870 (1986).

[183] C. Leforestier, J. Comput. Phys. **94**, 59 (1991).

[184] D. Kosloff and R. Kosloff, J. Comput. Phys. **52**, 35 (1983).

[185] D. Neuhauser, J. Chem. Phys. **93**, 2611 (1990).

[186] T. P. Grozdanov, V. A. Mendelshtam, and H. S. Taylor, J. Chem. Phys. **103**, 7990 (1995).

[187] V. A. Mendelshtam, T. P. Grozdanov, and H. S. Taylor, J. Chem. Phys. **103**, 10074 (1995).

[188] R. Chen and H. Guo, J. Chem. Phys. **105**, 1311 (1996).

[189] P. Lablanquie, F. Penent, R. I. Hall, J. Eland, P. Bolognesi, D. Cooper, G. C. King, L. Avaldi, R. Camillion, S. Stranges, M. Cereno, K. C. Prince, A. Müehleisen, and M. Žitnik, Phys. Rev. Lett. **84**, 431 (2000).

[190] T. Pacher, H. Köppel, and L. S. Cederbaum, J. Chem. Phys. **95**, 6668 (1991).

[191] T. Pacher, L. S. Cederbaum, and H. Köppel, J. Chem. Phys. **89**, 7367 (1988).